THESIS

# STRUCTURAL EVOLUTION AND RHEOLOGY OF THE PAPOSO SHEAR ZONE IN THE ATACAMA FAULT SYSTEM, NORTHERN CHILE

Submitted by

Rachel Courtney Ruthven

Department of Geosciences

In partial fulfillment of the requirements

For the Degree of Master of Science

Colorado State University

Fort Collins, Colorado

Fall 2018

Master's Committee:

Advisor: John Singleton

Jerry Magloughlin
John Ridley
Aditi Bhaskar

# ABSTRACT

## STRUCTURAL EVOLUTION AND RHEOLOGY OF THE PAPOSO SHEAR ZONE IN THE ATACAMA FAULT SYSTEM, NORTHERN CHILE

The Paposo fault zone is a major brittle-ductile strand of the Atacama fault system (AFS), which records sinistral shear associated with Mesozoic oblique subduction beneath northern Chile. The southern portion of the Paposo fault juxtaposes mylonitized Late Jurassic to Early Cretaceous granodiorite and Early Cretaceous tonalite east of the fault against nonmylonitic Early Jurassic granodiorite and metasedimentary rocks west of the fault. Geologic mapping along a 1.25 km-long transect across the east side of the Paposo fault documents a strain progression towards the core of the fault. Within this region, two related but temporally different shear zones can be identified in this area. Shear zone A deforms the Late Jurassic to Early Cretaceous granodiorite, and shear zone B deforms the Early Cretaceous tonalite. The Early Cretaceous and Late Jurassic granodiorites, moving from E to W, grade from unstrained to a ~75-250 m-thick zone containing discrete mylonitic bands (1 - 20 cm). This zone of variably strained granodiorite transitions to a ~300-1050 m-thick pervasive high strain zone which contains a ~50-550 m-thick band of hydrothermally-altered ultramylonite and locally mylonitized cataclasite, indicating that fluids played an important role in brittle-ductile deformation. The Late Jurassic to Early Cretaceous granodiorite is mylonitized cataclasite contains oblate clasts and S>L tectonite fabrics, suggesting transpressional flattening. Moving further west, shear zone B, a ~150-400 m-thick zone of younger tonalite (136.0 ± 1.6 Ma), grades from a low strain protomylonite adjacent to the hydrothermally-altered high strain zone to mylonite and locally ultramylonite against the brittle core of Paposo

fault. Across the transect, mylonitic foliations and lineations have a mean orientation of 043/62 SE and 18/211, respectively. Most SE-dipping mylonitic fabrics record sinistral-reverse shear that is consistent with the overall pattern of small-scale brittle faults, but in several parts of the hydrothermally-altered zone, symmetric microstructures suggest a component of pure shear. In the core of the fault, a ~50 m-thick illite-rich, subvertical gouge zone strikes ~018 and records sinistral S-C-C' fabrics. Regionally, the Paposo fault is arcuate, trending NNW-SSE in the northern end and NNE-SSW in the southern end. Previous studies, along the northern portion of the Paposo fault, have observed sinistral transtension, whereas, in this study, we observe evidence for oblique sinistral-reverse shear and local coaxial flattening indicate sinistral transpression along the southern portion of the Paposo fault. We propose that transtension and transpression along the AFS are controlled by the arcuate geometry, and both are compatible with sinistral simple shear along the N-S-trending magmatic arc.

Shear zone A is characterized by pervasive hydrothermal alteration, synkinematic mafic dike emplacement, and associated mylonitization of Early Cretaceous to Late Jurassic granodiorite. The age of alteration and mylonitization of shear zone A is mostly bracketed between ~139 Ma (138.8 ± 1.5 Ma: the age of the youngest altered pluton) and ~136 Ma (136.0 ± 1.6 Ma: the age of Early Cretaceous tonalite which lacks alteration and mafic dikes). Shear zone B is characterized primarily by protomylonitic fabrics in Early Cretaceous tonalite adjacent to the brittle fault core of the Paposo fault. The age of mylonitization in shear zone B is bracketed between ~136 Ma (the age of the tonalite) and ~117 Ma (when the shear zone cooled below ~190°C). This cooling age most likely overlaps with development of the Paposo fault gouge zone, which formed between 150-200°C based on clay mineralogy and the illite Kübler index. Together these data constrain brittle and ductile deformation to the Early Cretaceous, slightly older than the

timing of deformation along the Atacama fault system farther south. This timing difference may be attributed to the fact that Early Cretaceous plutons are slightly older here compared with synkinematic plutons farther south, and elevated temperature associated with pluton emplacement was needed for shear zone development.

The two shear zones along the southern Paposo fault provide significant insight into brittle-plastic deformation within the exhumed Late Jurassic to Early Cretaceous magmatic arc. The rheology and strength at the brittle-plastic transition of these two shear zones are controlled by two different interconnected weak phases. Due to partial breakdown of feldspar during hydrothermal alteration, shear zone A is dominated by a two-phase, fine-grained mixture of ~80% plagioclase and ~20% quartz with minor fine-grained chlorite and white mica along grain boundaries. Locally, shear zone B records a mylonitic overprint of cataclastic fabrics, suggesting that deformation occurred near the brittle-plastic transition during variable strain rates. Shear zone B lacks significant hydrothermal alteration and is rheologically controlled by interconnected quartz regions. Based on dynamically recrystallized quartz grain sizes, shear zone B is most likely stronger than shear zone A. Adjacent to the brittle Paposo fault, mylonite is locally cataclastically deformed in shear zone B and displays a ~6 μm mean dynamically recrystallized quartz grain size, suggesting peak deviatoric stress during deformation was ~118 MPa. We construct a rheological model of shear zone B and find that our estimate of peak stress at the brittle-plastic transition is consistent with typical shear zone strain rates (between $10^{-13}$ and $10^{-14}$) and a coefficient of friction ($\mu$) of 0.85 if the geothermal gradient is ~50°C/km. The modeled depth of ~6 km for the brittle-plastic transition is much shallower than most shear zones, and the peak crustal strength is ~58% lower than the predicted peak strength in areas with a more typical continental geothermal gradient of ~25°C/km. These results suggest that shear zones at subduction margins are more likely to

localize within magmatic arcs due to high geothermal gradients and reaction softening associated with hydrothermal alteration.

# ACKNOWLEDGEMENTS

First I would like to thank my advisor, Dr. John Singleton. He was extremely involved in the development and success of the project. He went to Chile for both field seasons to help with data collection, and afterwards was very helpful with guidance for analyzing and interpreting the data. John was a very strong motivating force and made sure I was able to complete the project on time.

I would also like to thank Dr. Jerry Magloughlin, who helped collect structural data in the field, take high quality field photos, use his drone to collect large-scale photos and videos, and helped in determining if pseudotachylyte was present. I would also like to thank Dr. John Ridley for his help with interpreting fluid inclusion, geochronological, and geochemical data.

I would like to thank Nikki Seymour, who was instrumental in collection of geochronological and thermochronological data discussed in this project and who was a great resource in understanding and interpreting the data.

I thank Rodrigo Gomila, Gert Heuser, Skyler Mavor, and Stewart Williams for their help with organizing field work and work as field assistants.

I would like to thank both Dave Adams and Bill Benzel who are researchers at the USGS laboratories in Denver. Dave Adams helped us prep samples for EBSD analyses and taught us how to collect and analyze the data. Bill Benzel helped prepare and further separate samples for XRD analyses, collected the XRD spectrums, and processed the raw data for us.

TABLE OF CONTENTS

LIST OF TABLES

LIST OF FIGURES

# 1. CHAPTER 1: THE GEOMETRY, KINEMATICS, AND TIMING OF DEFORMATION ALONG THE SOUTHERN SEGMENT OF THE PAPOSO FAULT ZONE, ATACAMA FAULT SYSTEM, NORHTERN CHILE

## 1.1.Introduction and geologic background

The Atacama fault system (AFS) in the Coastal Cordillera of northern Chile is a ~1,000 km-long, trench-parallel sinistral strike-slip system that was active during Mesozoic oblique subduction of the Phoenix plate beneath the South American plate (Fig. 1) (Scheuber and Andriessen, 1990; Brown et al., 1993; Cembrano et al., 2005). The AFS lies along the trace of the Jurassic-Early Cretaceous magmatic arc, suggesting strain localized within the rheologically weak arc (Fig. 2) (Scheuber and Gonzalez, 1999; Molnar and Dayem, 2010). The Paposo fault zone is the main strand in the Paposo segment of the Atacama fault system and is characterized by an arcuate NNE-striking zone in the southern end and a NNW-striking zone in the northern end with numerous NW-striking splays (Brown et al., 1993; Scheuber and Andriessen, 1990; Cembrano et al., 2005). Along the Paposo segment mylonitic fabrics are overprinted by brittle deformation (e.g. Scheuber and Andriessen, 1990; Brown et al., 1993; Scheuber and Gonzalez, 1999; Cembrano et al., 2005; Veloso et al., 2015; Gomila et al., 2016). The Paposo fault was reactivated during the Neogene as an E-side down normal fault (González et al., 2006; Loveless et al., 2010).

Previous studies along the Paposo fault have focused primarily on brittle faulting and ductile deformation along the northern segment near Antofagasta (Cembrano et al., 2005; Veloso et al., 2015; Gomila et al., 2016; Mitchel and Faulkner, 2009; Jensen et al., 2011; Arancibia et al., 2014). Cembrano et al. (2005) and Veloso et al. (2015) document brittle sinistral transtension associated with splays off the northern portion of the Paposo fault (Fig. 1b). Given the likely SE

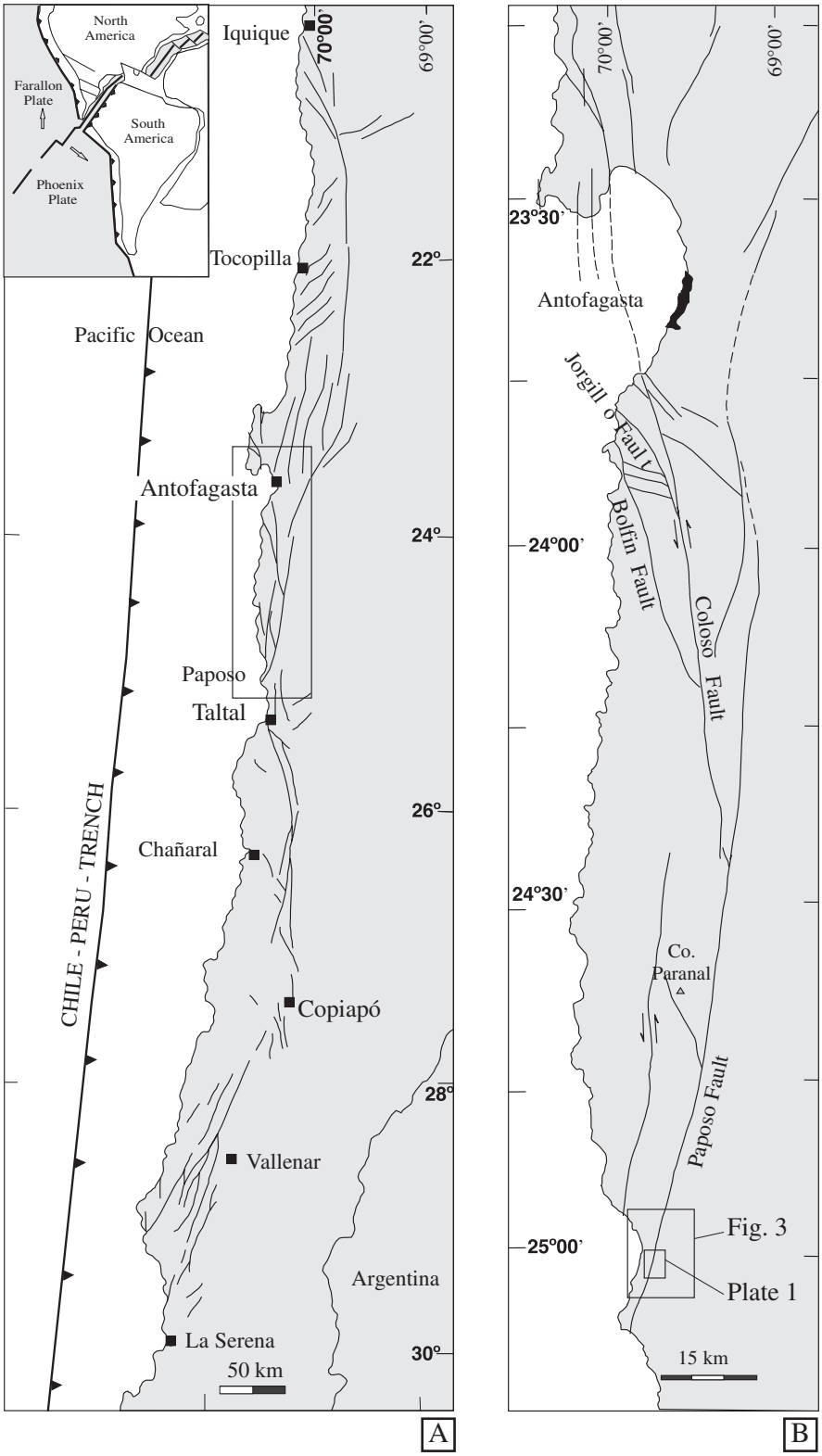


**Figure 1: A)** Simplified map of the Atacama Fault System with an inset of the Mesozoic plate configuration during sinistral deformation along the AFS. **B)** The Paposo fault segment of the AFS. The inset rectangle show the areas in Fig. 3 and Plate 1. (Modified from Cembrano et al, 2005; Brown et al, 1993; Scheuber and González, 1999)

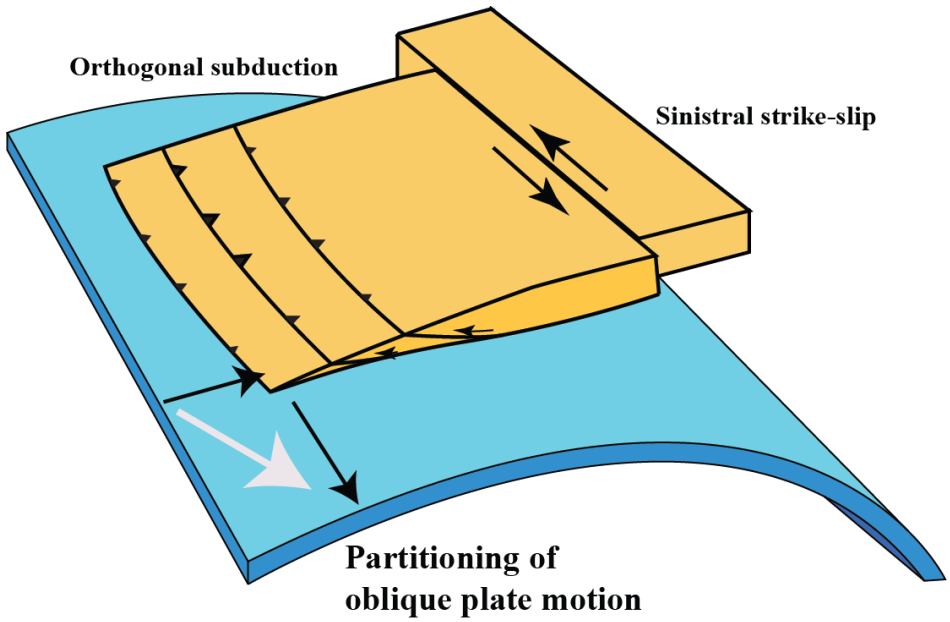


**Figure 2:** Schematic example of oblique plate motion partitioned into trench-orthogonal convergence and trench-parallel strike-slip motion. Strike-slip movement maybe localized within the weaker magmatic arc (Modified from Molnar and Dayem, 2010)

convergence direction of the Phoenix plate, sinistral transtension is consistent with the NNW-trend of the northern portion of the Paposo fault. Kinematics along the southern segment have not been previously been documented, but the NNE-trend along this part of the fault zone is more compatible with sinistral transpression.

Scheuber and Andriessen (1990) discuss the timing of deformation and conditions of ductile deformation along a portion of the Paposo fault, and Scheuber and Gonzalez (1999) interpret 4 stages of Jurassic to Cretaceous deformation along the Coastal Cordillera between 22° and 26°S. Stage 1 (195-155 Ma) is marked by formation of a broad belt of plutonic rocks which were sheared in sinistral arc-parallel strike-slip motion under granulite to amphibolite facies metamorphism (Scheuber and Andriessen, 1990; Scheuber and Gonzalez, 1999). In stage 2 (160-150 Ma), there is evidence for arc normal extension by shallow brittle low-angle normal faults and some deeper ductile normal faults (Scheuber and Gonzalez, 1999). Stage 3 (155-147 Ma) is defined by two reversals in stress regime evidenced by two generations of dikes (Scheuber and Gonzalez, 1999).

The older set trends NE-SW, whereas the younger set trends NW-SE (Scheuber and Gonzalez, 1999). Sinistral mylonitic fabrics, sinistral offset of dikes and plutons along brittle structures mark the change to sinistral strike-slip deformation under greenschist-facies conditions in stage 4 (Scheuber and Andriessen, 1990; Scheuber and Gonzalez, 1999). $^{40}Ar/^{39}Ar$ and Rb-Sr ages of mylonitic fabrics constrain stage 4 to ~125 Ma (Scheuber et al., 1995; Scheuber and Gonzalez, 1999). The AFS may have originated as a sinistral, trench-linked system during stage 4 (Scheuber and Andriessen, 1990; Scheuber and Gonzalez, 1999; Fig. 2). Scheuber and Andriessen (1999) also find that ductile deformation occurred in plutonic rocks of roughly the same age, suggesting that high temperature associated with pluton emplacement was needed for shear zone development. Most estimates of the timing of deformation along the AFS are only loosely constrained by K-Ar and $^{40}Ar/^{39}Ar$ cooling ages (Grocott et al., 1994; Scheuber et al., 1995; Dallmeyer et al., 1996). Regional studies have touched on the timing and kinematics of the Paposo fault, but none have focused in detail on the southern Paposo segment. In this paper, we examine the geometry, kinematics, and timing of deformation along the southern segment of the Paposo fault zone. We study geometry and kinematics of deformation through analyses of field-based structural data from mylonitic and brittle structures, analyses of mylonitic microstructures, 3D strain analyses of strained clasts, and analyses of recrystallized quartz fabrics. Timing of deformation and relationship between deformation and magmatism are studied by determining the U-Pb zircon ages of 5 igneous intrusions and determining the zircon (U-Th)/He cooling age of 2 igneous intrusions.

### 1.2.Study area and previous mapping

This study focuses on detailed geologic mapping and kinematic analysis of a 15 $km^2$ area along the southern segment of the Paposo fault (Fig. 3). This area has been previously mapped at

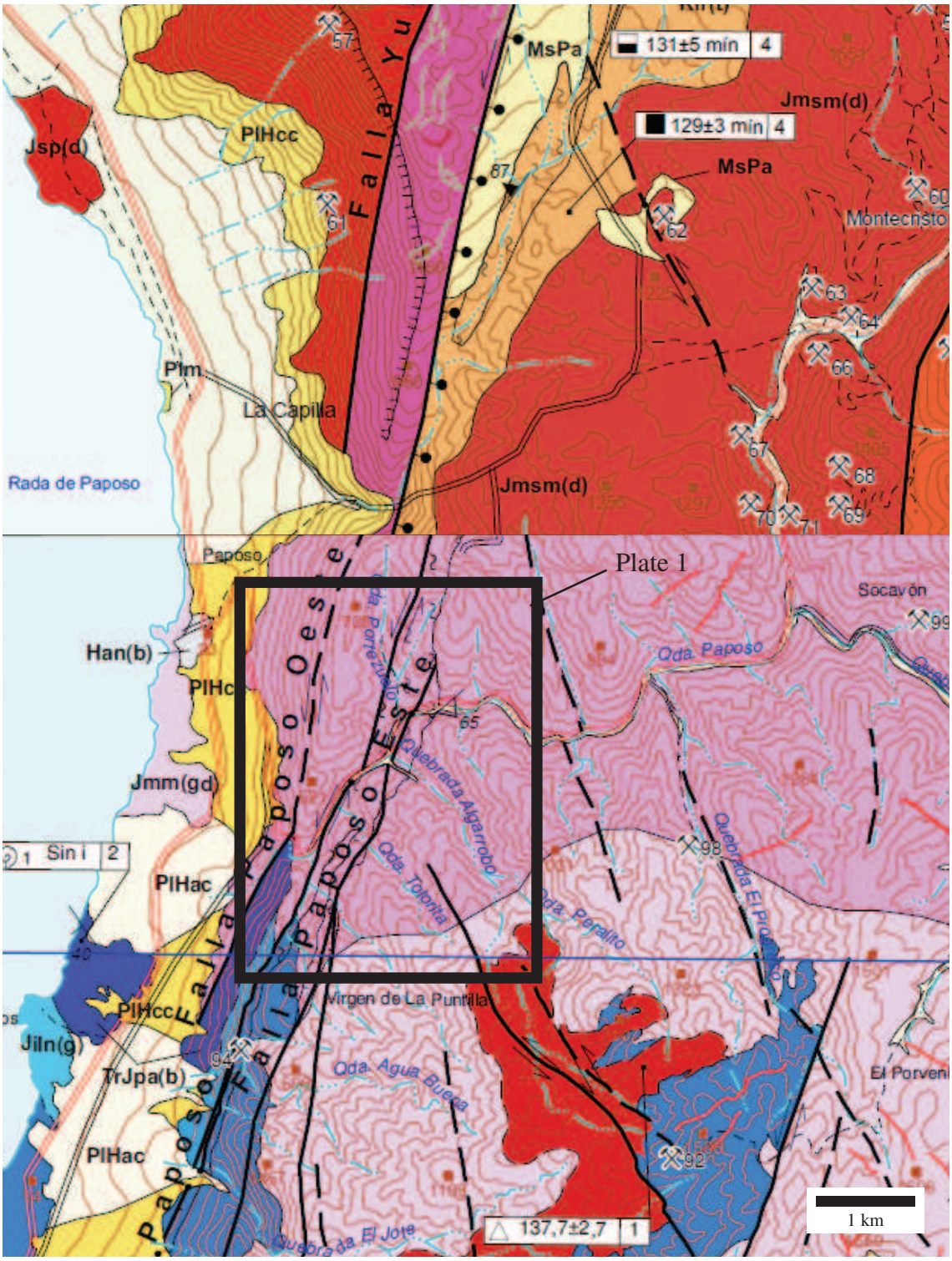


**Figure 3:** Existing 1:100,000-scale geologic maps of the southern end of the Paposo fault by Escribano et al. (2013), south portion and Alvarez et al. (2016), north portion. Enlarged view of the inset from Figure 1b. The black rectangle outlines this study's map area. The units within the rectangle are quartz diorite (dark pink); biotite, pyroxene, and amphibole granodiorites (light pink); calcareous sandstones (dark blue); porphyritic andesitic composition intrusives (light blue); and andesitic and basaltic lava flows (medium blue).

1:100,000 scale by Escribano and others (2013), and the area just north of this study was mapped first by Scheuber and Andriessen (1990) and later by Alvarez et al. (2016) at 1:100,000 scale (Fig. 3). This area is optimal for field mapping due to good access along highway B-710 and bedrock exposure that is significantly better than exposures further inland (Fig. 4), and discrepancies such as mismatched boundary faults and units across the two 1:100,000-scale maps can be resolved by our detailed mapping (Fig. 3) (Escribano et al., 2013; Alvarez et al., 2016).

## 1.3.Methods

### *1.3.1. Field methods and structural analysis*

We mapped a 15 $km^2$ area along the southern Paposo Segment of the AFS at 1:10,000-scale to determine map unit geometries and structural fabric orientations. Structural data were collected using a Brunton compass and notes and data were recorded with an associated global position system (GPS) waypoint. The geologic map in plate 1 was created through assembling basemaps and waypoints in ArcGIS and digitizing map units and structural data in Adobe Illustrator. Cross sections were also made with Adobe Illustrator and used to determine structural thicknesses of shear zones across the map area.

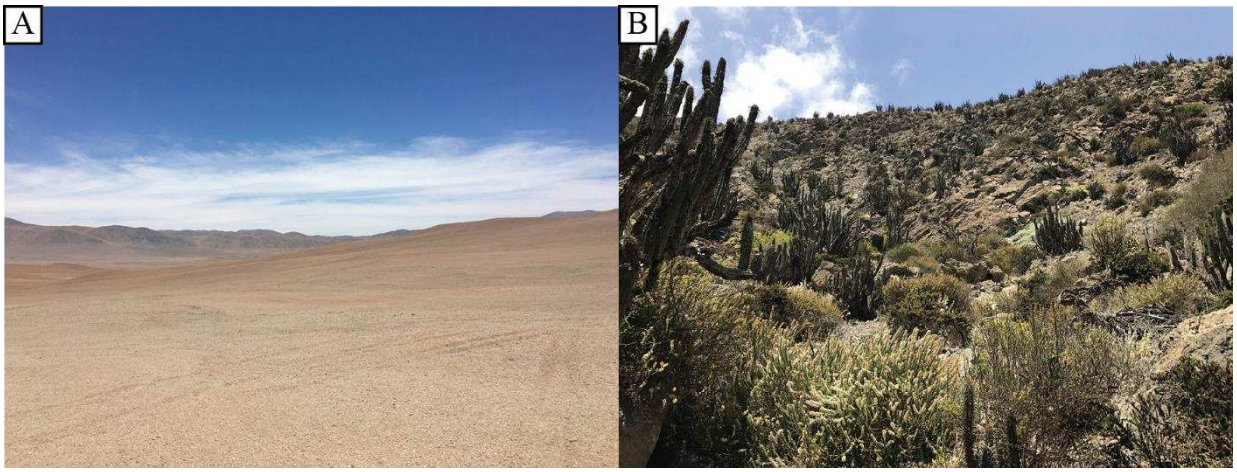


**Figure 4: A)** Representative photo of the landscape at a slightly higher elevation, just north of the area along the road B-710. **B)** Representative photo of the landscape within the study area. Coastal fog banks provide water, and result in significantly better outcrop exposure.

Structural data were analyzed with Stereonet 9 and FaultKin, and we used the maximum eigenvectors to present mean orientations (Marrett and Allmendinger, 1990; Allmendinger et al., 2012; Cardozo and Allmendinger, 2013). In the field we measured the orientations of brittle fault planes and slickenlines and interpreted slip sense based primarily on Riedel shears, lunate steps, mineral growth steps, offset features, and gouge foliation patterns. We assumed a slip sense on striated faults with unknown slip sense (~27% total) based on geometric similarity and/or kinematic compatibility to faults with known slip sense. We present kinematic data of faults with known and assumed slip sense separately and together for comparison. Then we calculate the expected fault plane using Linked Bingham fault plane solutions in FaultKin (Marrett and Allmendinger, 1990; Allmendinger et al., 2012).

We collected dozens of mylonite samples for kinematic and microstructural analyses. We cut X-Z sections of 33 oriented ductilely-deformed samples to determine the kinematics of the shear zones. We note kinematic indicators from microstructural observations. Using ImageJ and photomicrographs of recrystallized quartz regions oriented parallel to foliation, we traced recrystallized grains to find the average recrystallized grain size and to measure the oblique grain shape angle. We also determine deformation mechanisms through petrographic observations. To help determine the strain geometry of the hydrothermally-altered mylonite zone we also collected axial ratios and orientations of mylonitized cataclasite clasts, which were used to calculate a strain ellipsoid using EllipseFit program (Vollmer, 2018).

### *1.3.2. Geochronological and thermochronological methods*

To determine the timing of magmatism and deformation along the southern Paposo fault, we analyzed 5 samples for zircon U-Pb geochronology: one sample from the Early Jurassic (EJ) granodiorite west of the Paposo fault, two samples from the Late Jurassic-Early Cretaceous (LJ-

EK) granodiorite east of the fault, one sample from a high-strain aplite sill within the LJ-EK granodiorite, and one sample from the Early Cretaceous (EK) tonalite on the east side of the fault. Samples were crushed using a mini-jaw crusher, sieved below 300 microns, panned to remove clay-size particles and concentrate dense grains, magnetically separated using a Frantz, and separated by density using heavy liquids. We used two mounting methods for zircon separates. Samples 16-1-P31 (LJ-EK granodiorite), 18-1-P73 (EK tonalite) and 18-1-P81 (EJ granodiorite), were poured onto tape mounts and left unpolished. For samples 17-1-P26 (LJ-EK granodiorite), and 17-1-P124 (strained aplite sill), we mounted selected zircons with few imperfections in epoxy and polished the mount to expose the central portions of zircons. Polished mounts were then imaged using cathodoluminescence (CL) at the United States Geological Society, Denver Microbeam Laboratory. Using laser ablation inductively coupled plasma mass spectrometry (LA-ICP-MS) U-Pb ratios were measured in 20 to 40 zircons for each sample. Samples mounted on tape were depth profiled to obtain ages from the zircon rims and cores (e.g. Marsh and Stockli, 2015), and samples mounted in an epoxy puck were measured at specific spots chosen based on CL images. None of the depth profiled samples revealed evidence of metamorphic rims.

We also analyzed 5 euhedral zircons from sample 16-1-P31 (Early Cretaceous granodiorite) for (U-Th)/He thermochronology and 4 euhedral zircons from sample 18-1-PJ88 (Early Jurassic granodiorite). All of the thermochronological and geochronological analytical work was done at Dr. Daniel Stockli's (U-Th)/He and U-Pb Geo-Thermochronology Lab at the Jackson School of Geosciences, University of Texas in Austin using equipment and methods outlined at https://www.jsg.utexas.edu/he-lab/u-thhe-noble-gas-lab/.

The geochronology data were filtered to eliminate isotope ratios for both >5% and >10% discordance. For each sample, we show plots of the ages in figure 5 (<5% discordance) and figure

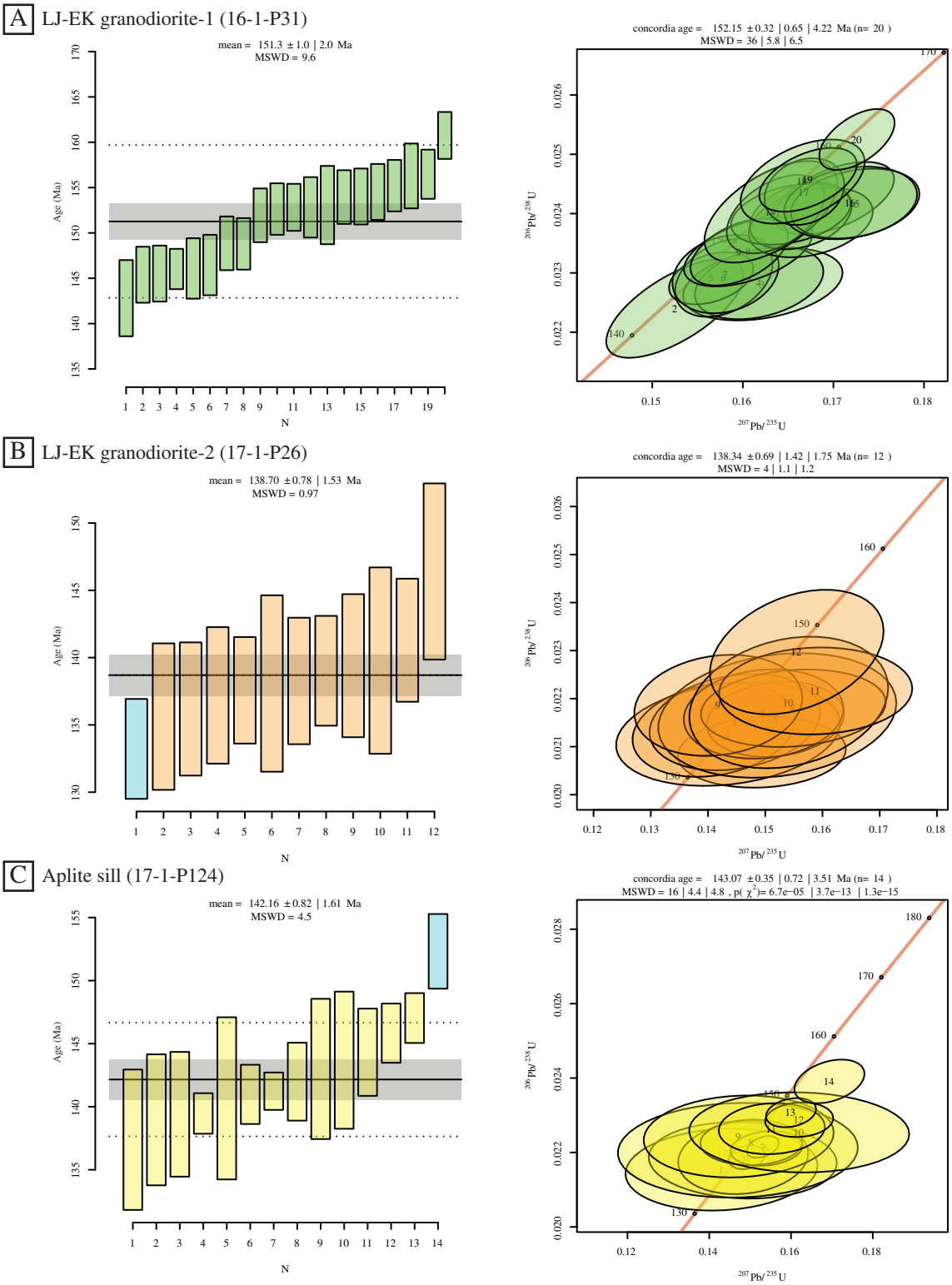


**Figure 5:** Weighted mean plots and corresponding concordance plots filtered for less than 5% discordance for samples **A)** LJ-EK granodiorite-1 (16-1-P31), **B)** LJ-EK granodiorite-2 (17-1-P26), **C)** aplite sill (17-1-P124), **D)** Early Cretaceous tonalite (18-1-PJ73), and **E)** Early Jurassic granodiorite (18-1-PJ81). The gray rectangle is the 2-σ region and the blue bars are dates rejected by the weighted mean algorithm.

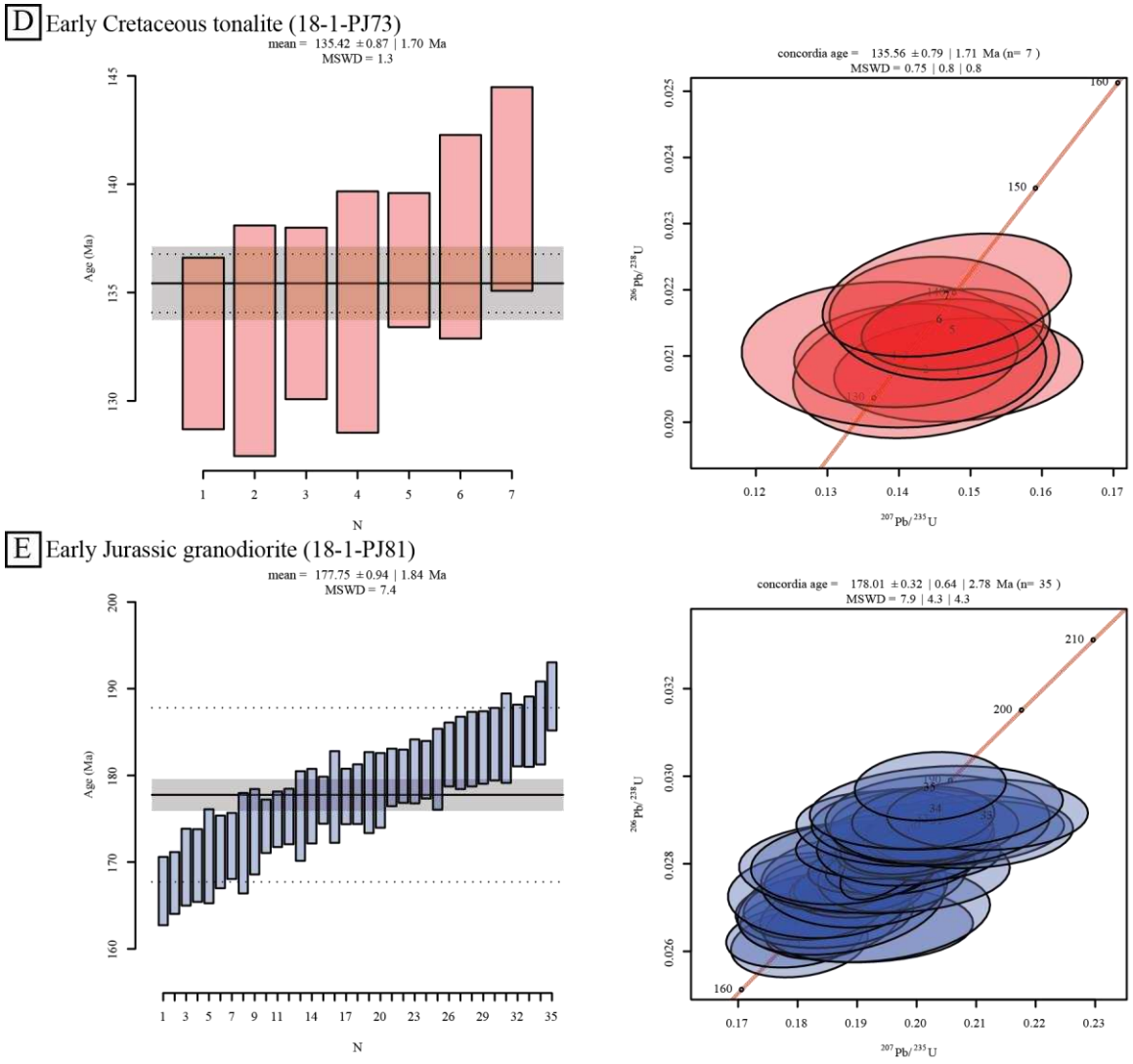


**Figure 5 continued**

6 (<10% discordance). However, in the text we present weighted mean $^{238}U/^{206}Pb$ ages from zircons with <5% discordance for samples 16-1-P31 (LJ granodiorite) and 18-1-PJ81 (EJ granodiorite), and for samples 17-1-P26 (EK granodiorite), 17-1-P124 (aplite sill) and 18-1-PJ73 (EK tonalite) we present an age using a 10% discordance filter due to the relatively small number of zircons with <5% discordance (<20 zircons per sample). The ages calculated from isotopic ratios filtered for 5% and 10% discordance do not vary by more than 0.2% from each other. All geochronology plots were made using IsoplotR (Vermeesch, 2018) and the thermochronology plots were made with excel.

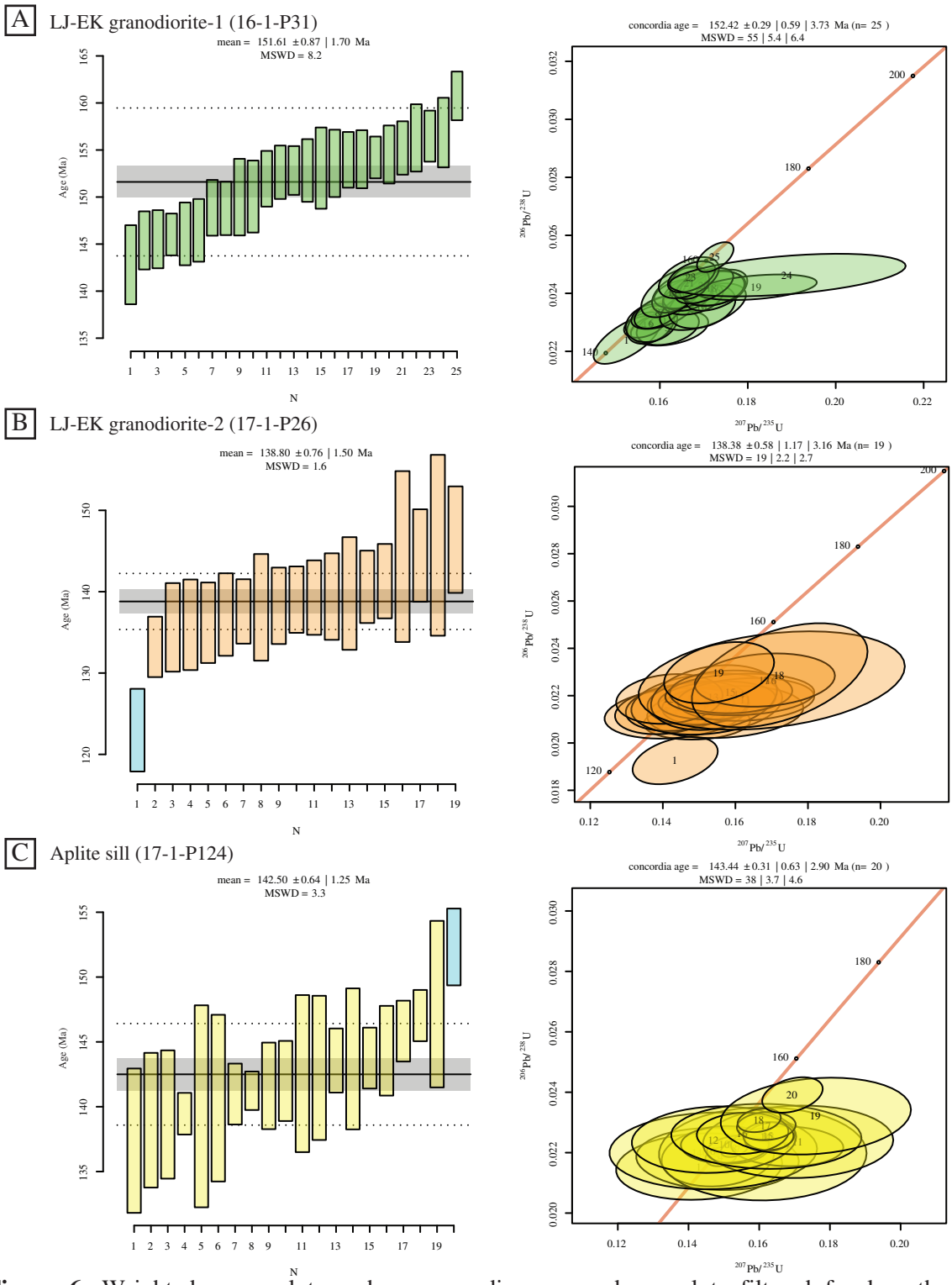


**Figure 6:** Weighted mean plots and corresponding concordance plots filtered for less than 10% discordance for samples **A)** LJ-EK granodiorite-1 (16-1-P31), **B)** LJ-EK granodiorite-2 (17-1-P26), **C)** aplite sill (17-1-P124), **D)** Early Cretaceous tonalite (18-1-P73), and **E)** Early Jurassic granodiorite (18-1-PJ81). The gray rectangle is the 2-σ region and the blue bars are dates rejected by the weighted mean algorithm.

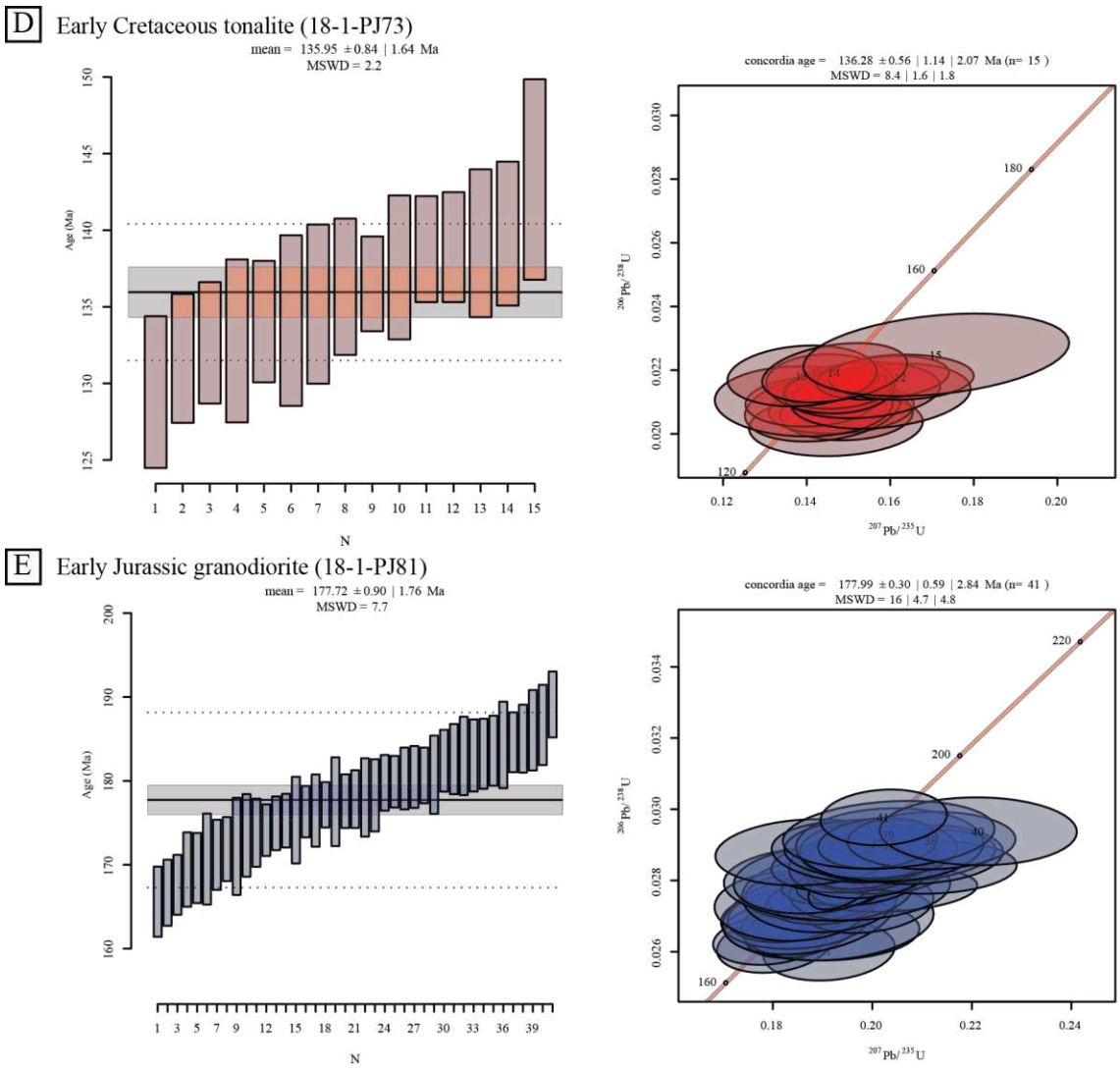


**Figure 6 continued**

### *1.3.3. Illite crystallinity*

Illite crystallinity was determined for the clay gouge zone to determine temperature of clay formation. The gouge was first sieved to remove sand-sized grains and then was settled out of a water column using a separatory funnel at Colorado State University. Then samples were side packed and scanned using X-ray diffraction (XRD) for over an hour to determine mineralogy at the XRD laboratory at the USGS in Denver. Later, the samples were further separated, at the USGS in Denver, using a centrifuge to 2-0.5 micron and < 0.5 micron size fractions. The both size fractions were split in half and air dried and ethylene glycolated to determine if there were

expandable clays and measured again using the XRD to find full width and half maximum (FWHM) peak for illite clay at the USGS in Denver. This resulted in 4 FWHM measurements.

### 1.4.Description of map units and geochronology results

The geologic map is broken into 7 different map-scale units based on compositional differences as well as deformation characteristics. From oldest to youngest, these units are an Early Jurassic (?) undifferentiated metasedimentary unit, an Early Jurassic (EJ) granodiorite, an Late Jurassic-Early Cretaceous (LJ-EK) granodiorite which has been subdivided into four units by the degree of penetrative strain and alteration, an Early Cretaceous (EK) tonalite, a clay-rich gouge zone along the Paposo fault (Plate 1).

The undifferentiated very slightly metamorphosed sedimentary rocks are made up of metamorphosed limestone, siltstone, and fine-grained sandstone which have undergone low-grade contact metamorphism (Fig. 7a). These metasedimentary rocks lack penetrative fabrics and significant recrystallization. The siliciclastic rocks are immature and rich in clay, and the limestone is micritic with locally abundant silt.

The Early Jurassic granodiorite has a zircon U-Pb age of 177.8 ± 1.8 Ma (Fig. 5e) (Appendix 1 and 2). However, this age has a very high MSWD of 7.4, and the distribution of dates in the weighted mean deviation plot suggests that there is protracted crystallization. The individual concordant zircons range from 189 to 166 Ma. This sample has a zircon (U-Th)/He cooling age of 104.1 ± 21.4 Ma (Fig. 8a). In the field, this unit does not crop out very well. Although this granodiorite dominates the western side of the fault, many of the outcrops within this unit consist of younger, more resistant mafic and intermediate dikes. It is chloritically altered, oxidized, and pervasively fractured but nowhere has mylonitic fabrics (Fig. 7b). Most of this unit is fine- to

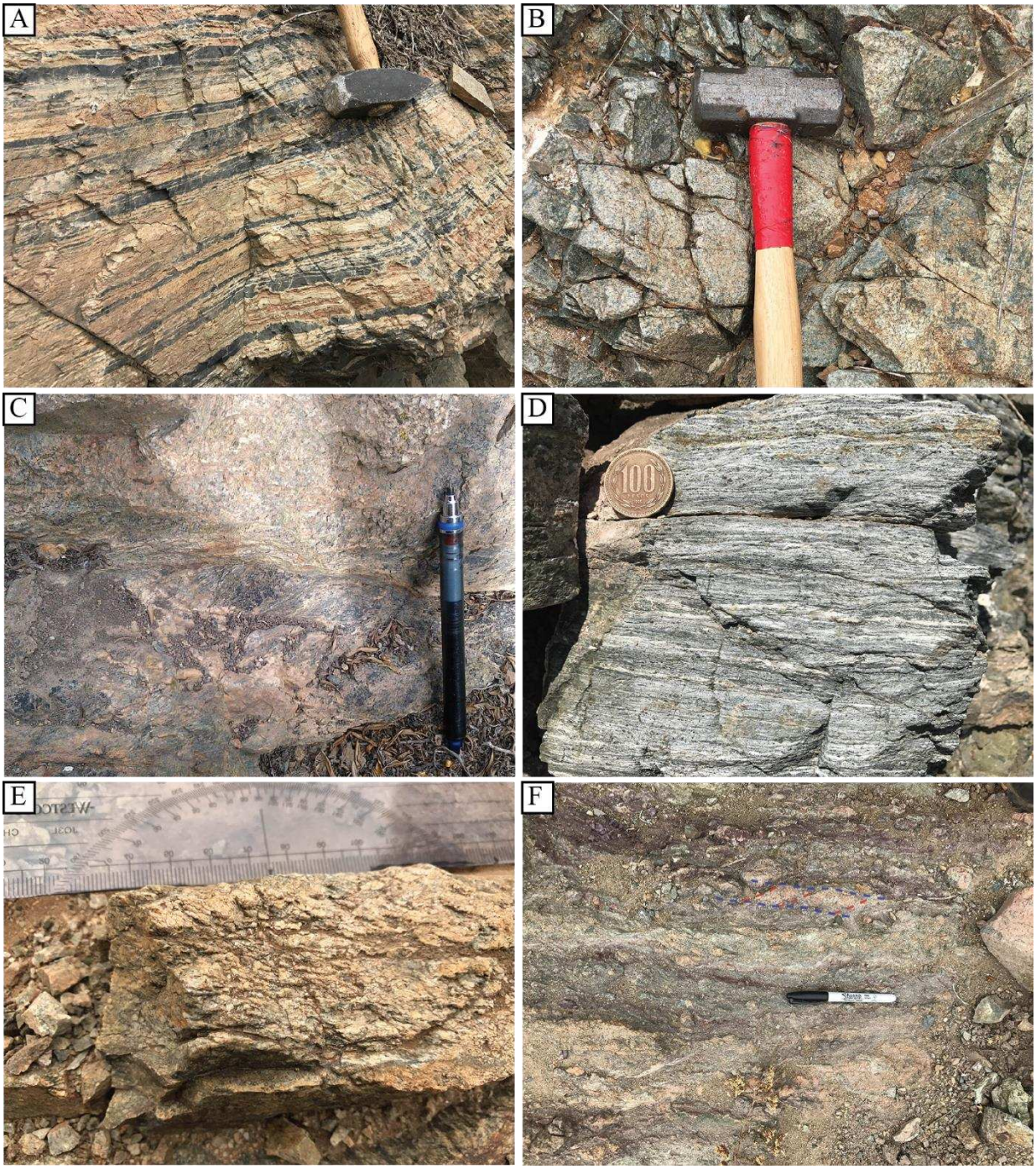


**Figure 7:** Representative outcrop photos of **A)** siliciclastic metasedimentary rocks from the undifferentiated metasedimentary rock unit, **B)** the Early Jurassic granodiorite, **C)** a discrete high strain zone in the Late Jurassic granodiorite, **D)** hydrothermally-altered mylonite derived from the LJ-EK granodiorite (coin diameter ~27 mm), **E)** a protomylonite from the Early Cretaceous tonalite unit, and **F)** a foliated illite-rich gouge zone along the Paposo fault with blue and red dashed lines highlighting the fabrics.

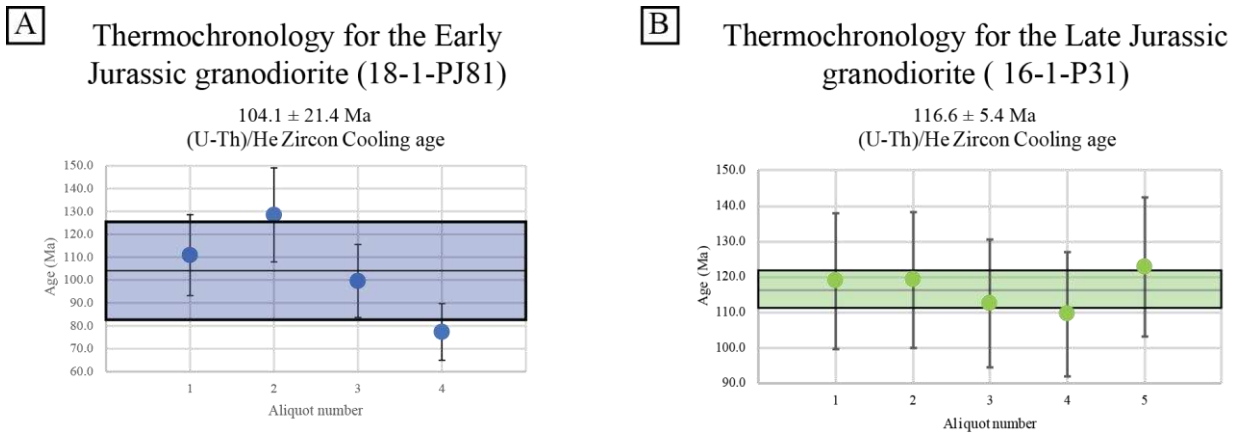


**Figure 8: A)** A graph plotting the (U-Th)/He zircon cooling ages for 4 aliquots from the Early Jurassic granodiorite (18-1-PJ81). The blue bar is the 2-σ region. **B)** A graph plotting the (U-Th)/He zircon cooling ages for 5 aliquots from the Late Jurassic granodiorite (16-1-P31). The green bar is the 2-σ region.

medium-grained (1-4mm) and consists of ~20-27% quartz, ~40-55% plagioclase, ~8-19% potassium feldspar, ≤3% biotite, and ~10-14% chlorite which replaces biotite (Fig. 9d).

The LJ-EK granodiorite has zircon U-Pb ages of 138.8 ± 1.5 Ma and 151.3 ± 2.0 Ma (Fig. 6b and 5a) (Appendix 1 and 2). However, the sample with an age of 151.3 ± 2.0 Ma has a high MSWD and a kernel density estimation (KDE) plot of the data with a bandwidth of 2, has a bimodal distribution (Fig. 10a). Therefore, we interpret the younger population as the age of the intrusion (146.5 ± 1.1 Ma) (Fig. 10b). The ~147 Ma sample has a (U-Th)/He zircon cooling age of 116.6 ± 5.4 Ma (Fig. 8b). This unit has been subdivided into a hydrothermally-altered, pervasively strained zone (~50-550 m-thick) (Fig. 7c), a dominantly mylonitized zone with discrete unstrained zones (~80-500 m-thick), a dominantly unstrained granodiorite with minor discrete high strain zones (~75-250 m-thick) (Fig. 7d), and an unstrained zone (Plate 1). The LJ-EK granodiorite has a range of mineralogical composition from plagioclase-dominated granodiorite to more quartz and plagioclase-quartz dominated granodiorite, and the two main mafic minerals are chlorite which pseudomorphs biotite and slightly less abundant hornblende (Fig. 9a and b). Highly strained aplite sills are locally present within the hydrothermally-altered zone. One of these aplite sills has a zircon U-Pb age 142.5 ± 1.3 Ma (Fig. 6c) (Appendix 1 and 2).

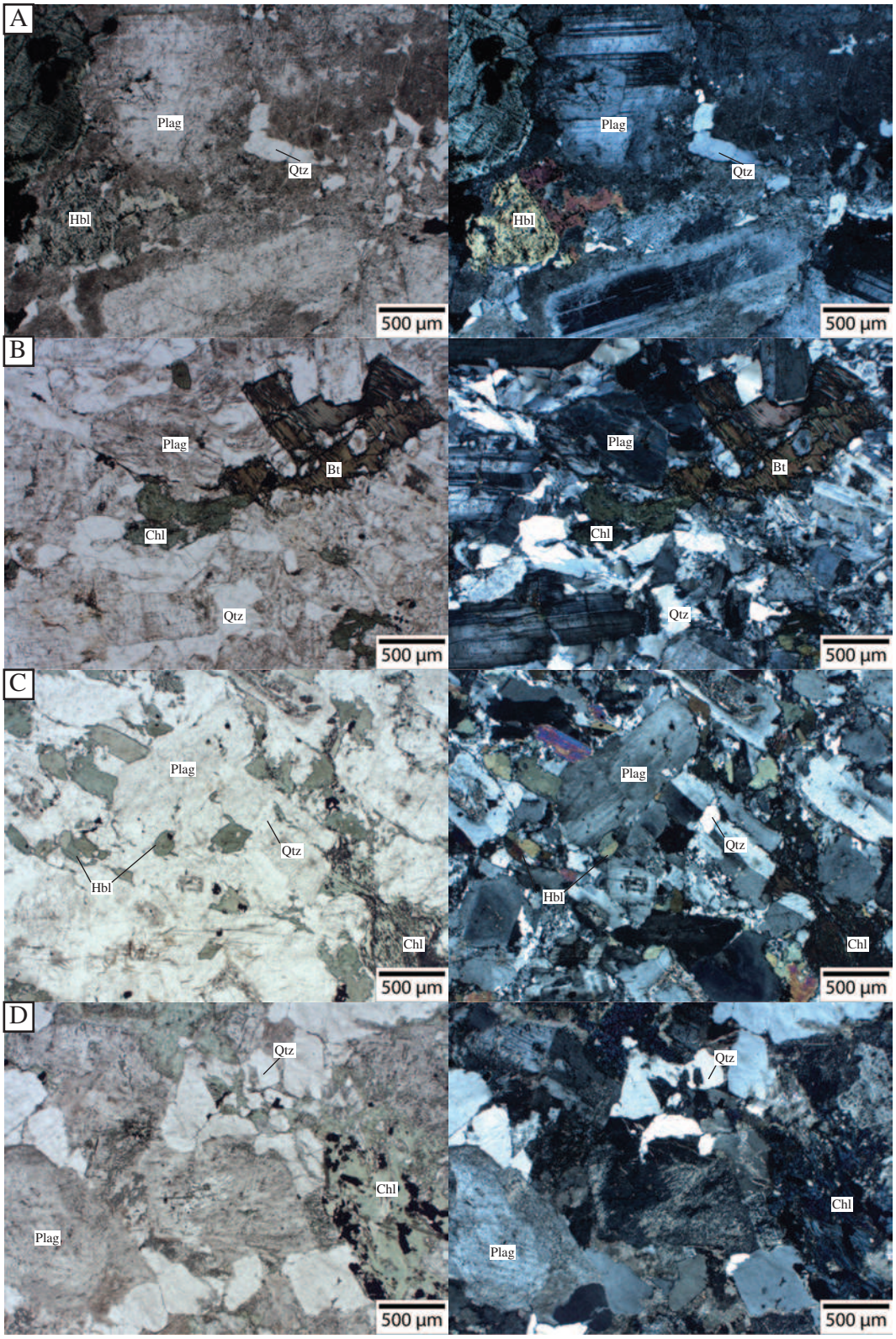


**Figure 9:** Plane polarized light and cross polarized light photomicrographs with representative textures and mineralogies from samples **A)** 16-1-P31 (Late Jurassic granodiorite), **B)** 17-1-P26 (Early Cretaceous granodiorite), **C)** 18-1-PJ73 (Early Cretaceous tonalite), and **D)** 17-1-PJ81 (Early Jurassic granodiorite).

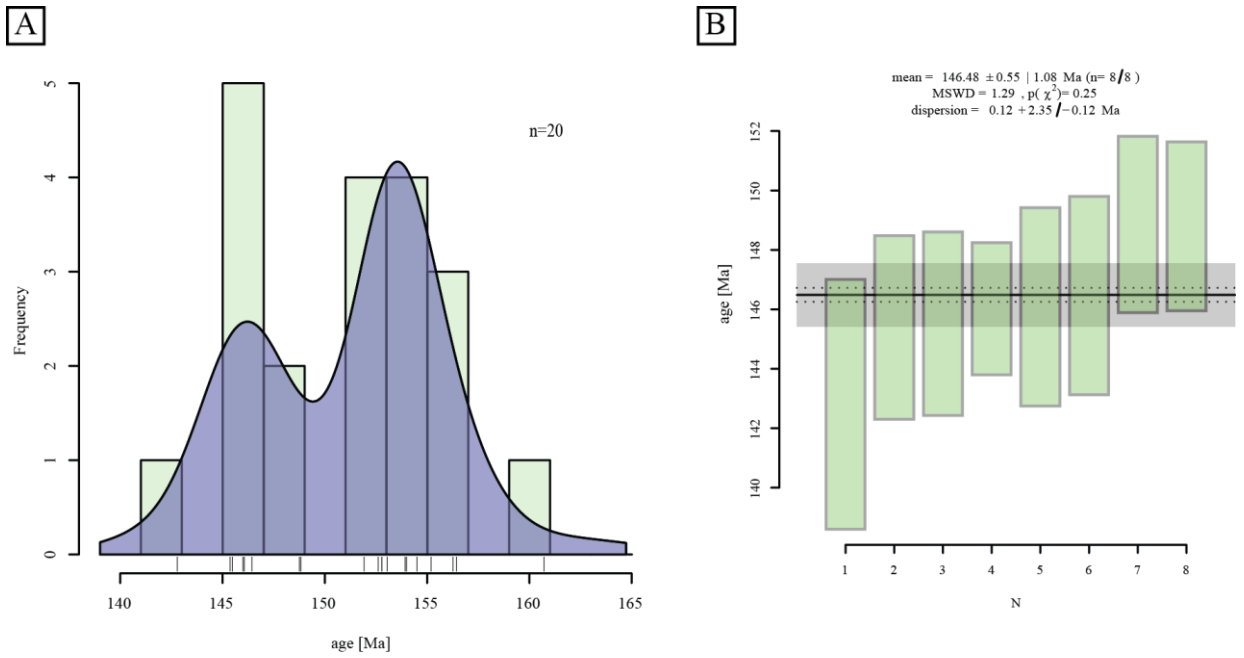


**Figure 10: A)** A kernel density estimation (KDE) plot of zircons from the Late Jurassic granodiorite (16-1-P31), with a histogram of the data in green, using a bin size of 2 my, and the distribution in dark blue, using a bandwidth of 2 my. This plot shows a bimodal distribution of dates. **B)** A weighted mean distribution of the younger population of dates from sample the Late Jurassic granodiorite (18-1-P31).

The mean sum of weighted deviation (MSWD) of this population is 3.3 which is relatively high, suggesting that this is not a single population of zircons. Some of these zircons may be inherited, in which case perhaps just the younger subset of zircons are autocrystic. Both the LJ-EK granodiorite and the EJ granodiorite are intruded by mafic dikes.

The EK tonalite has a zircon U-Pb age of 136.0 ± 1.6 Ma and is mostly protomylonitic (~150-400 m-thick) (Fig. 6d and 7e). The EK tonalite has local unstrained areas (<10 m-thick) at the eastern margin with the hydrothermally-altered unit in the LJ-EK granodiorite, but the contact between these two units is not exposed in the field area (Appendix 1 and 2). The tonalite grades from protomylonite to mylonite and becomes increasingly brittlely deformed at contact with the gouge zone. In addition, there are also <5 m thick slivers of ultramylonite along the eastern contact which were likely derived from the EK tonalite. The tonalite has roughly ~20-33% quartz, ~46-50% plagioclase, ~4-5% potassium feldspar, ≤20% hornblende, ~2% oxides, and ~1% chlorite which pseudomorphs biotite (Fig. 9c). Secondary chlorite veins locally make up 7% of this unit

(Fig. 9c). The protomylonite is neither bleached nor intruded by the mafic dikes that intrude the LJ granodiorite and the LJ-EK granodiorite.

A ~50 m-thick gouge zone defines the core of the Paposo fault. Based on detailed X-ray diffraction (XRD) data the gouge zone mineralogy is made up of quartz, albite, illite, chlorite, calcite, and hematite. This gouge zone contains a foliation defined by scaly clay-rich zones and cataclastically deformed zones derived from Early Jurassic granodiorite on the west side of the fault (Fig. 7f). No mylonitized clasts from the east side were found in the gouge zone, but the slivers of ultramylonite and mylonite along the eastern contact with the gouge zone are locally overprinted by cataclastic deformation. To estimate the temperature of authigenic clay formation in the gouge and we determined the clay mineralogy and the Kübler index (KI) of illite (Fig. 11) from the gouge zone using XRD. There is no smectite clay in this gouge, suggesting temperatures

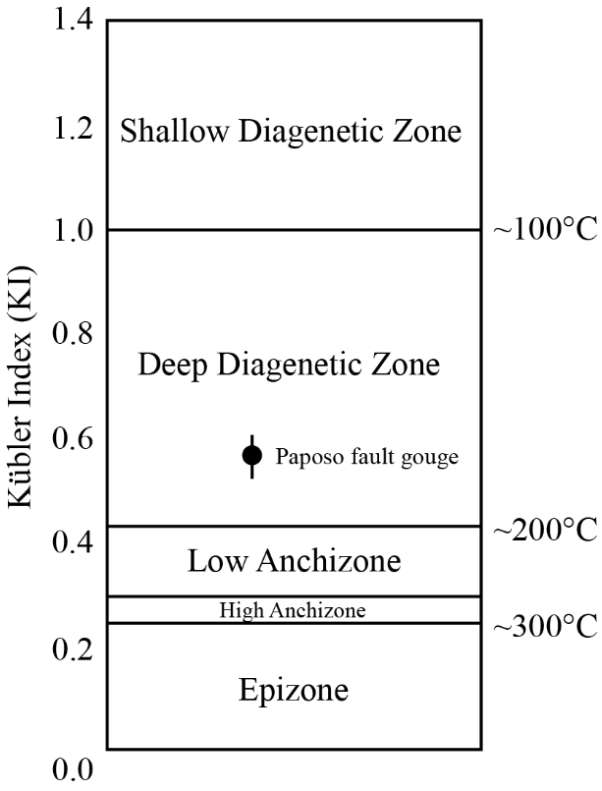


**Figure 11:** Kübler Index and corresponding estimated temperature of formation of the illite in the clay gouge (modified from Verdel et al, 2011).

were above ~150°C, where ≥85% of clay should be illite due to the upper thermal stability of smectite (Abad, 2007). However, this lack of smectite clay could also reflect the initial lack of mixed-layer clays. The full width at half maximum peak for the gouge is ~0.529-0.611 $\Delta^{o}2\theta$, which is consistent with clay formation within the deep diagenetic zone near the boundary with the low anchizone (Fig. 11) (Verdel et al., 2011). Both the lack of smectite and this KI suggests the gouge developed in the ~150-200°C temperature range.

### 1.5.Fabrics and kinematics

#### *1.5.1. Ductile fabrics*

The mylonitized plutonic bodies within the map area are the LJ-EK granodiorite and the EK tonalite east of the Paposo fault. Mylonitic fabrics have an average foliation and lineation of 041/63 SE and 18/212, respectively, and the average foliation strikes ~23° clockwise of the Paposo fault (Fig. 12). As outlined in the previous section, the LJ-EK granodiorite is divided into 4 different zones based on deformation and alteration characteristics. From west to east these zones

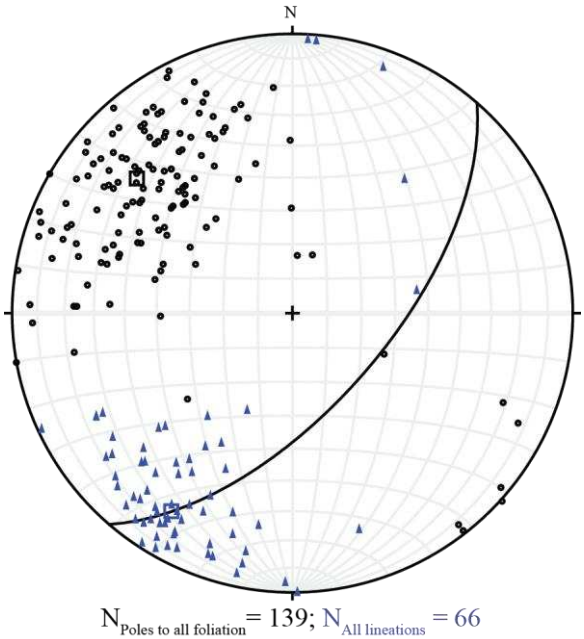


**Figure 12:** All poles to foliations (black hollow circles) and all lineations (blue circles) with the average pole and average lineation plotted as large squares with the same color. The average foliation plane is also plotted as a black arc. The average pole to foliation is 27/311; the average foliation is 041/63 SE; and the average lineation is 18/212.

(and average mylonitic foliation and lineation in each zone) are: 1) a hydrothermally-altered zone that is >90% mylonitic and commonly ultramylonitic (foliation 043/64 E; lineation 19/218), 2) a zone consisting of >50% discrete mylonitic zones (typically <1 m thick) with unstrained zones (foliation 020/62 E; lineation 10/192), 3) a zone consisting of <50% discrete mylonitic zones (foliation 044/49 E; lineation 24/204), and 4) an unstrained zone lacking discrete shear zones (Fig. 13a and b). The mylonitic fabrics within the discrete shear zones are mostly high strain zones associated with mafic dikes. The majority of these mylonitic to ultramylonitic fabrics record a sinistral shear sense (Fig. 14).

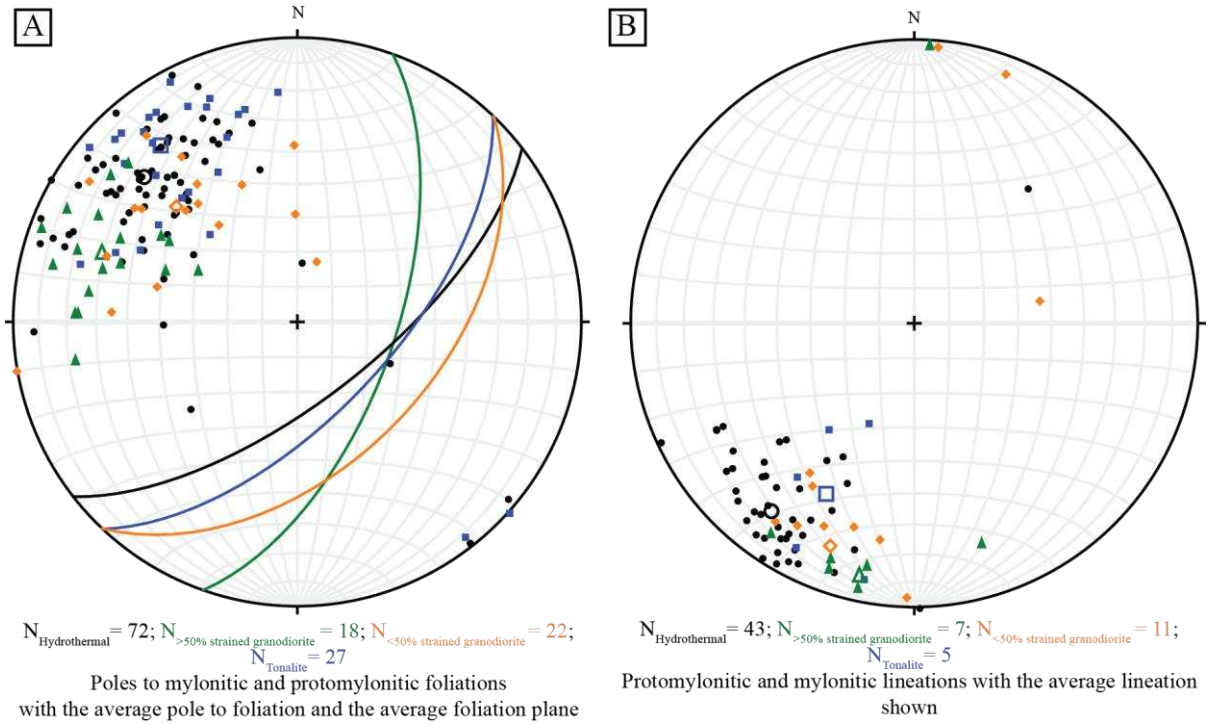


**Figure 13: A)** Poles to mylonite and protomylonite foliations and the average foliation plane. The black poles (circles) and average pole to foliation (large hollow black circle, 26/313), green poles (triangles) and average pole to foliation (large hollow green triangle, 28/290), orange poles (diamonds) and average pole to foliation (large hollow orange diamond, 51/314), and the blue poles (squares) and average pole to foliation (large hollow blue square, 22/322) correspond to measurements from the hydrothermal zone, more than 50% strained, less than 50% strained granodiorite, and tonalite, respectively. Arcs of the same color correspond to the average foliation plane for that unit (black: 043/64 E, green: 020/62 E, orange: 044/49 E, blue: 052/68 E). **B)** Black circles, green triangles, orange diamonds, and blue squares correspond to lineations from the hydrothermal zone, the more than 50% strained granodiorite, the less than 50% strained granodiorite, and the tonalite, respectively. The larger hollow symbols are average lineations for the respective units (black: 19/218, green: 10/192, orange: 24/204, blue: 33/208)

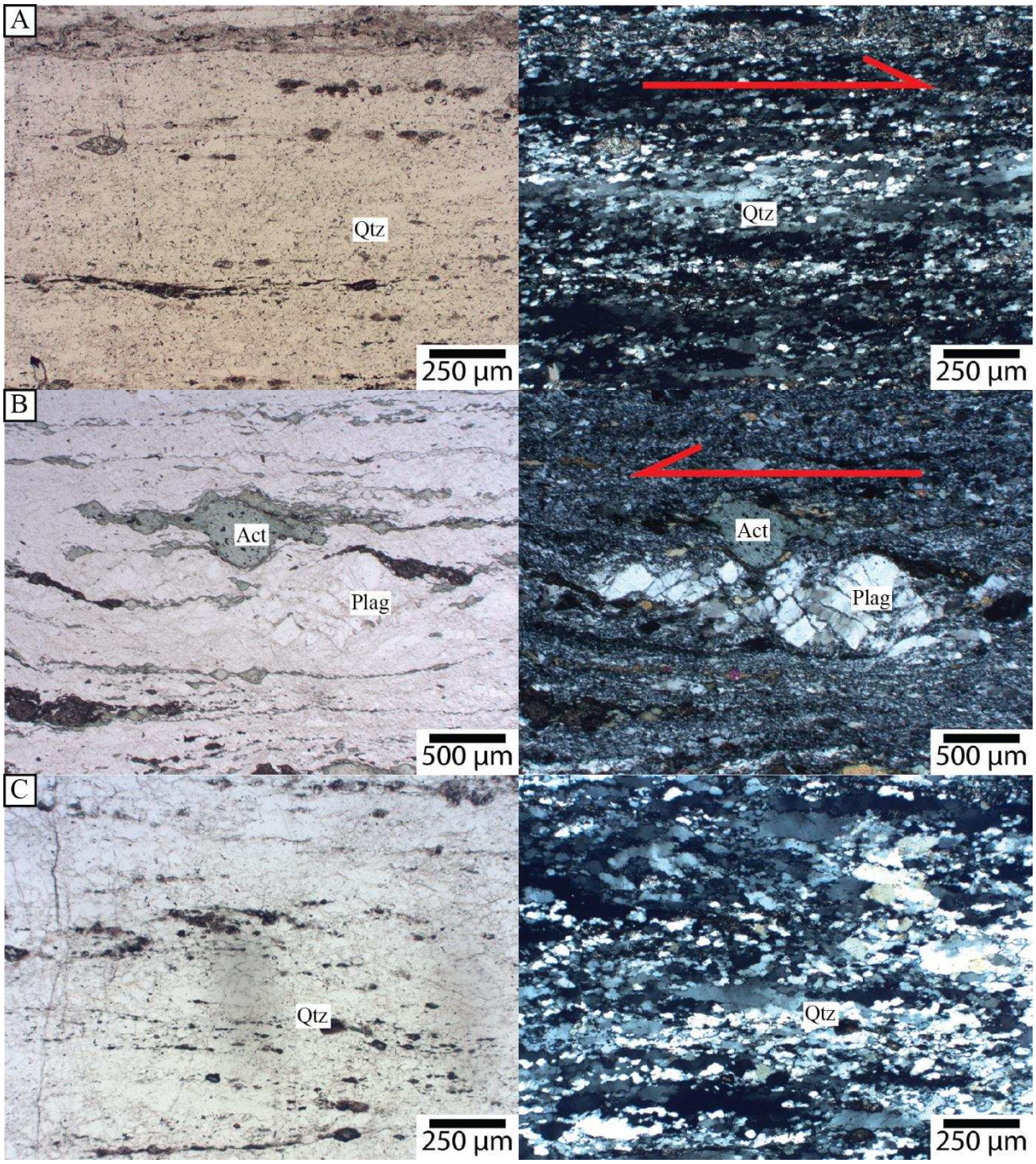


**Figure 14:** Plane-polarized light and cross-polarized light photomicrographs with sinistral shear fabrics (in the map-view reference frame) from samples **A)** hydrothermally-altered zone, 16-1-P23a (oblique grain shape fabric), **B)** hydrothermally-altered zone, 16-1-P30a (domino feldspar with synthetic shear fractures and asymmetric porphyroclast). **C)** Plane- and cross-polarized light photomicrographs of a symmetric grain shape fabric from the hydrothermally-altered zone, 17-1-P9. Evidence of subgrains within quartz and dynamically recrystallized grains are polygonal.

Based on more limited data, the average foliation and lineation orientations in the protomylonitic EK tonalite are 052/68 SE and 33/208, and the angle between the mean foliation

and the Paposo fault is 34° (Fig. 13a and b). The protomylonite foliations are more east striking, and the lineations are more steeply plunging than the average mylonitic fabrics in the LJ-EK granodiorite. There is weak spatial relationship between the strike of the protomylonitic fabrics and distance from the gouge zone (Fig. 15). The angle between protomylonite foliations and the gouge zone apparently decreases toward the gouge zone. However, this relationship is weakly developed, as evidenced by the low $r^2$ value corresponding to foliation angle with respect to proximity to the Paposo fault (Fig. 15).

### *1.5.2. Ductile strain kinematics*

Thirty-three X:Z thin sections of oriented mylonite samples were used to determine shear sense and to evaluate deformation conditions. We determined shear sense by examining shear sense indicators such as dynamically recrystallized oblique grain-shape fabric, domino-fractured

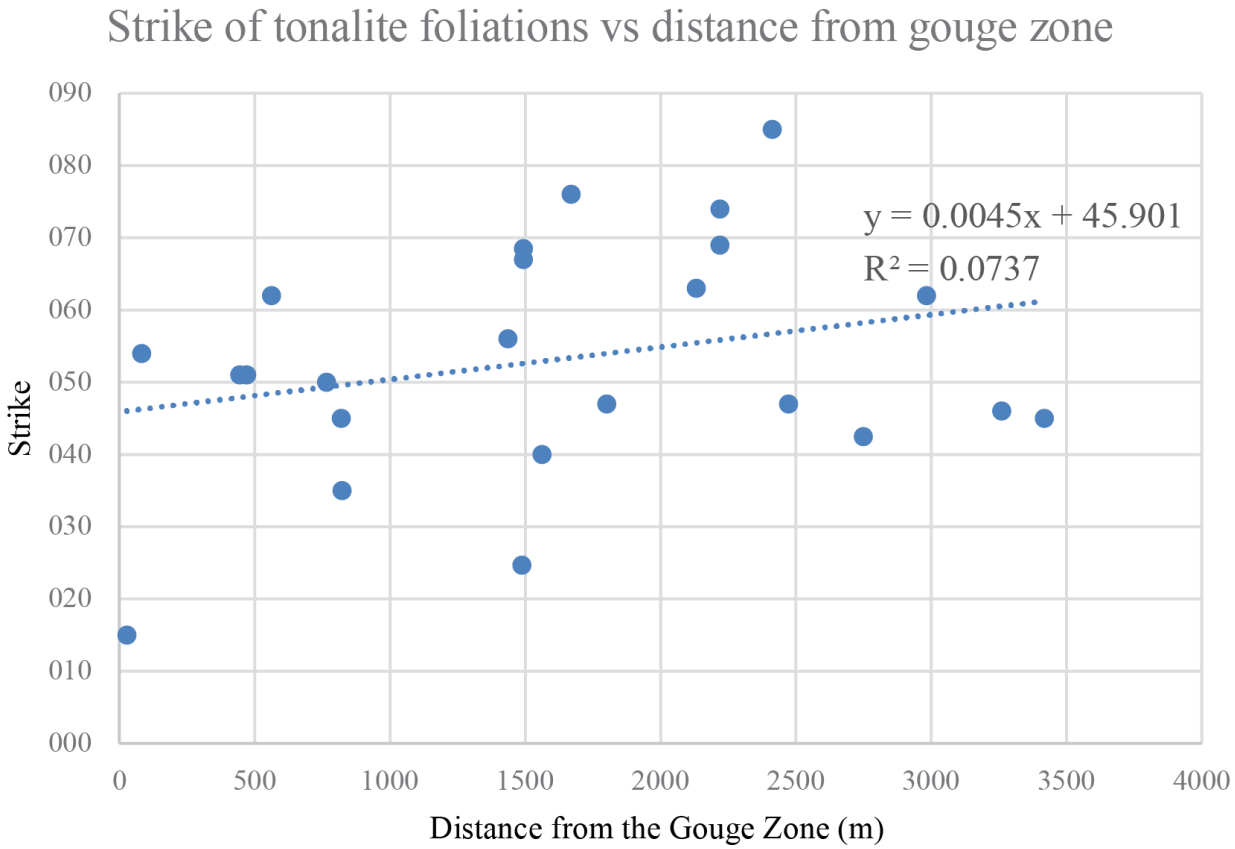


**Figure 15:** Graph showing the relationship between the strikes of protomylonitic foliations, measured in the tonalite unit, to the distance of the measurement from the gouge zone.

feldspar, and asymmetric porphyroclasts (Figs. 14a and b). From microstructural observations 24 out of 33 thin sections record a sinistral shear sense (in the map-view reference frame), whereas 9 out of 33 have indeterminate shear sense, and 1 out of 33 has subtle dextral shear sense indicators (Appendix 3). Of the 9 samples with an indeterminate shear sense, 2 are ultramylonites, 1 is from a discrete shear zone and 6 are from the hydrothermally-altered zone. The shear sense of the 6 samples from the hydrothermally altered zone could not be determined due to conflicting shear sense indicators and a lack of clear oblique grain-shape fabrics. The samples from the hydrothermally-altered zone have oblique grain shape fabrics with an average maxima that is 30° counterclockwise of foliation, but locally grain shape fabrics lack clear asymmetry (Fig. 16), whereas samples from the protomylonite zone have consistently asymmetric oblique grain-shape fabrics with an average maxima that is 36° counterclockwise of the foliation (Fig. 17). Since most mylonitic fabrics have SSW-plunging lineations on SE-dipping foliation planes (Fig. 13a and b) the dominant sinistral shear includes a component of SE-side up reverse shear, and the tonalite has may have experienced more oblique slip as evidenced by steeper plunging lineations (Fig. 13b).

A minority of discrete shear zones within the <50% mylonitic zone have macroscopic dextral shear indicators, and one records 30 cm of reverse displacement of a mafic dike. These dextral shear zones have an average orientation of 015/85 E and an average lineation of 06/194 (Fig. 18), and the reverse shear zone is oriented 003/55 E with a lineation of 53/080. The shears with macroscopic dextral indicators are more N-S striking than the sinistral mylonitic fabrics. Microscopically these dextral fabrics have a high degree of symmetry. Based on the orientations of the dextral shears subparallel to the Paposo fault and their largely symmetric fabrics, we interpret the dextral shears to record a component of coaxial strain. We also see evidence of a significant coaxial component of strain from outcrop scale. A distinct outcrop within the

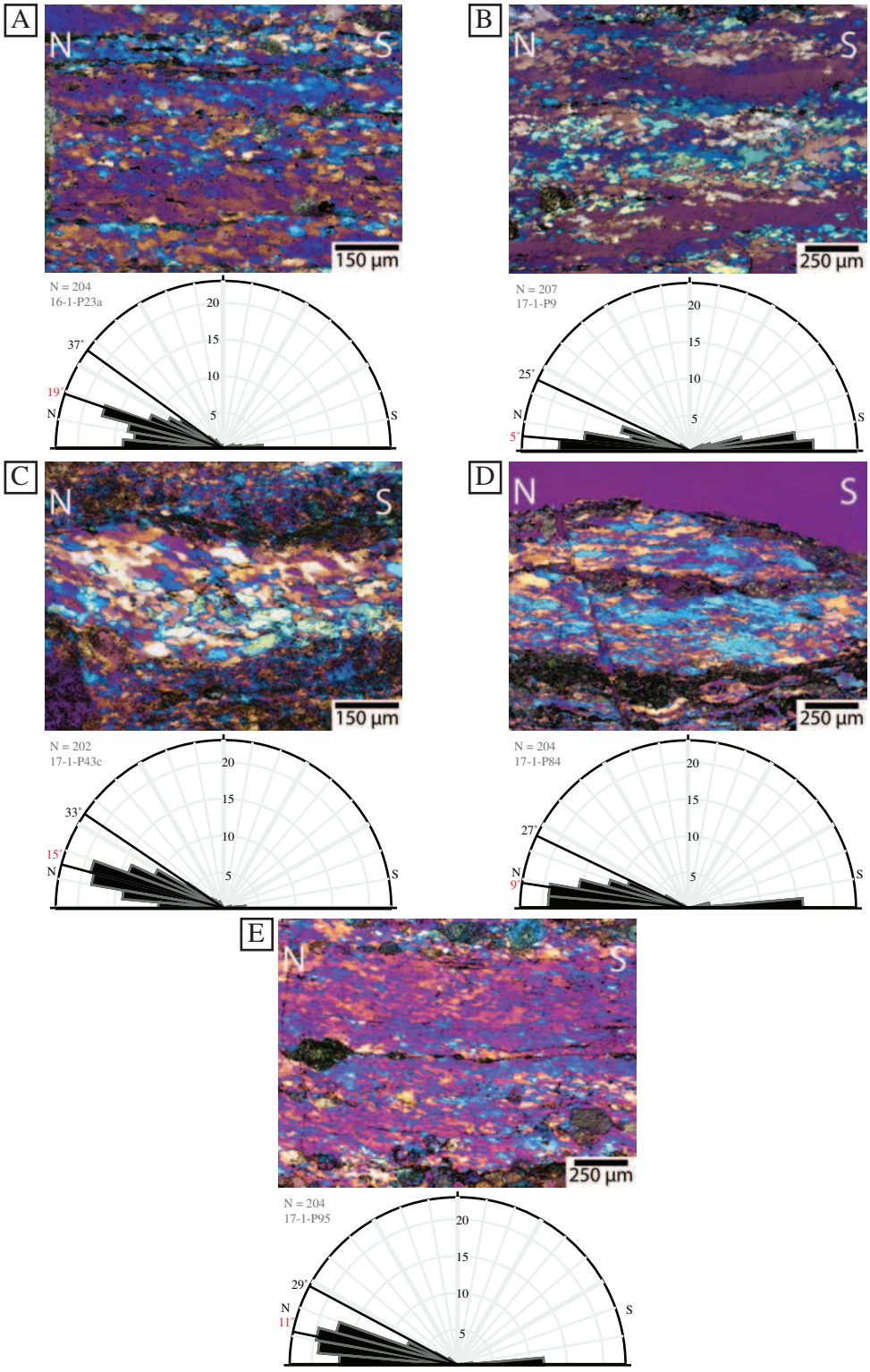


**Figure 16:** Photomicrographs and plots of 5 different samples from the hydrothermally-altered zone within the Late Jurassic-Early Cretaceous granodiorite. The plots beneath the photomicrographs show the maximum dynamically recrystallized grain shape angle (black number) and the mode angle (red number) found by tracing recrystallized grains using ImageJ. **A)** 16-1-P23a, **B)** 17-1-P9, **C)** 17-1-P43c, **D)** 17-1-P84, and **E)** 17-1-P95

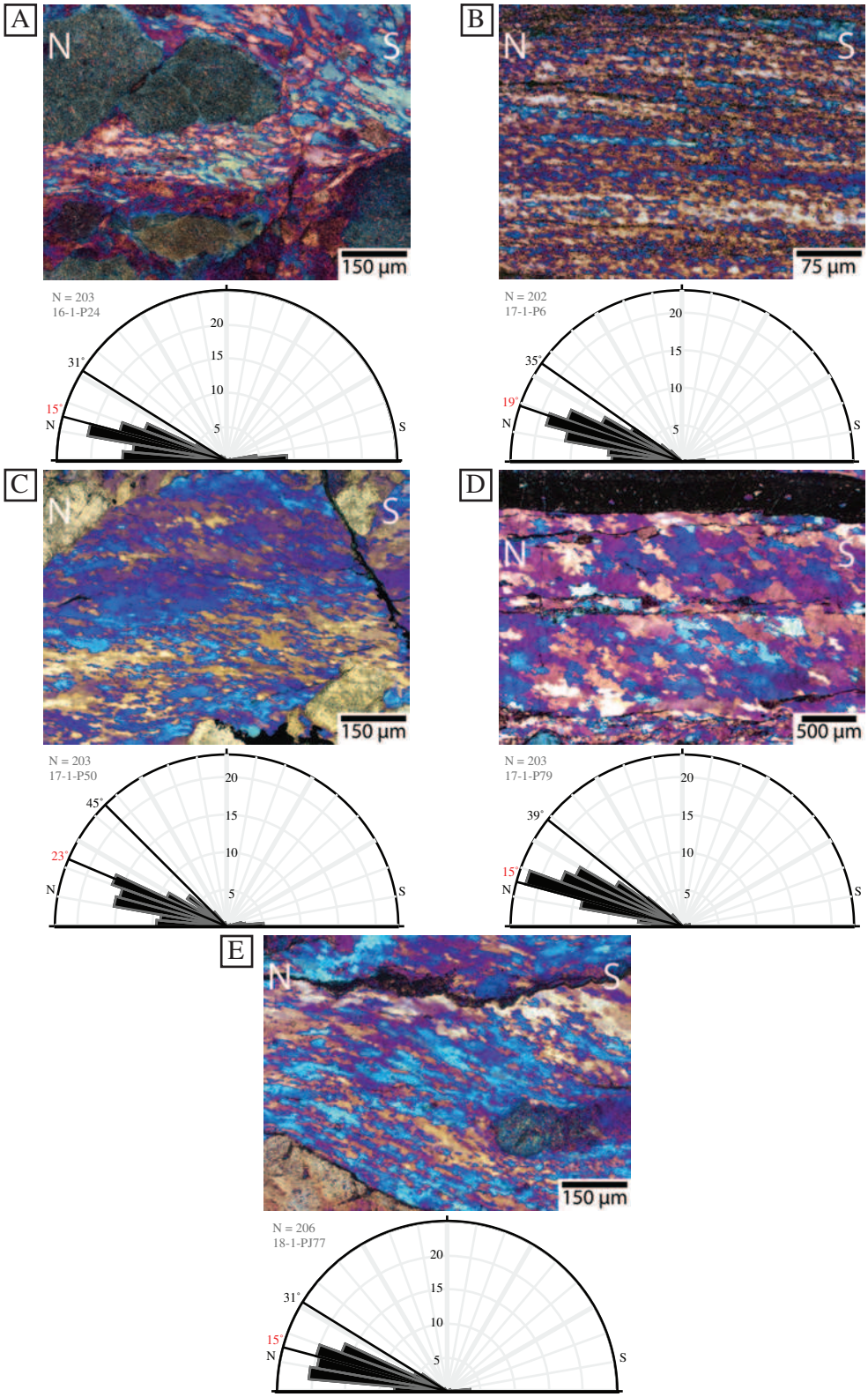


**Figure 17:** Photomicrographs and plots of 5 different samples from the Early Cretaceous tonalite. The plots beneath the photomicrographs show the maximum dynamically recrystallized grain shape angle (black number) and the mode angle (red number) found by tracing recrystallized grains using ImageJ. **A)** 16-1-P24, **B)** 17-1-P6, **C)** 17-1-P50, **D)** 17-1-P79, and **E)** 18-1-PJ77

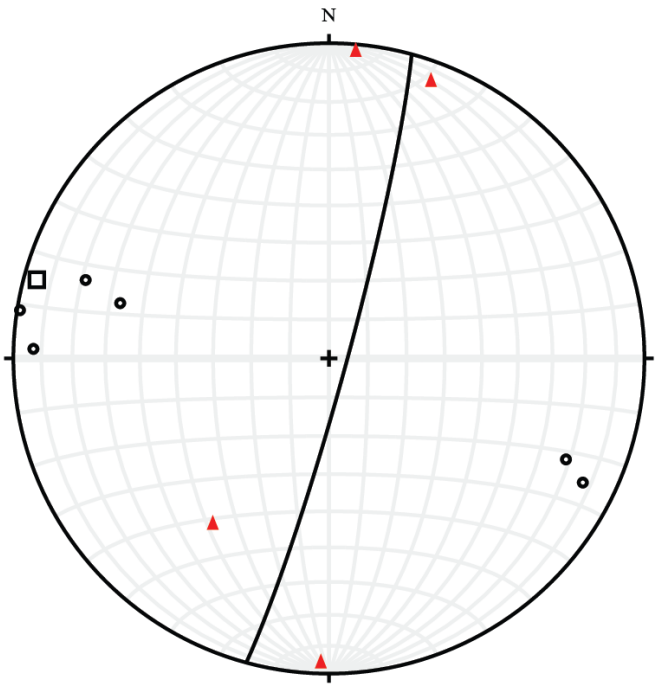


**Figure 18:** Stereoplot of poles to foliations with dextral shear sense (hollow black circles) and lineations (red triangles) with the average pole to foliation (hollow black square) and the average dextral foliation plane.

hydrothermally-altered zone (P43 labelled in Plate 1) consists of elongate LJ-EK granodiorite clasts within a foliated mafic matrix (Fig. 19). Based on the angular shapes of many clasts and the large range of clast sizes, we interpret this outcrop as either an intrusive breccia or cataclasite with


**Figure 19:** Outcrop photos of granodiorite clasts in a mafic matrix **A)** foliation parallel view with angular clasts and **B)** foliation perpendicular view.

brittle mixing of LJ-EK granodiorite and mafic dikes. This brecciation was then followed by mylonitization of both the granodiorite and altered mafic dike. This switch between ductile deformation to brittle deformation and back suggests that this zone formed at the brittle-ductile transition as strain rates and/or fluid pressures fluctuated. The granodiorite clasts are flattened parallel to the mylonitic foliation and elongate parallel to a weakly-developed lineation. To quantify the strain geometry recorded in these clasts we measured the axial ratios and orientations of 34 clasts from across the outcrop. We calculated a best-fit ellipsoid from these data using EllipseFit (Vollmer, 2018) (Fig. 20a). Calculated finite strain axes from these data closely match those inferred from measured fabrics at the outcrop (Fig. 20b), and the best-fit ellipsoid plots within the general flattening strain region, which is consistent with the S>L tectonite fabric at the outcrop.

### *1.5.3. Brittle fabrics and kinematics*

Brittle faults have a greater scatter of orientations than the ductile fabrics (Figs. 12 and 21). Excluding one kinematically anomalous W-dipping normal fault mapped in the southeastern part of the study area (Plate 1), the average small-scale fault orientation is 019/75 E (Fig. 21a). This orientation roughly parallels the Paposo fault. Faults that record sinistral slip have the most geometrically consistent orientation, with an average fault plane of 021/79 E and average slickenline orientation of 01/019 (Fig. 21b). The average P- and T-axes for faults with a known slip sense are 02/323 and 36/232, respectively. Faults with kinematic slip determined in the field (known faults) have a Linked Bingham fault plane solution (Marrett and Allmendinger, 1990) of 014/64 E with a slickenline orientation of 23/182 (Fig. 22a); the assumed faults (faults with kinematic sense determined later based on geometric similarity and/or kinematic compatibility to faults with known slip sense) have a Linked Bingham fault plane solution (Marrett and

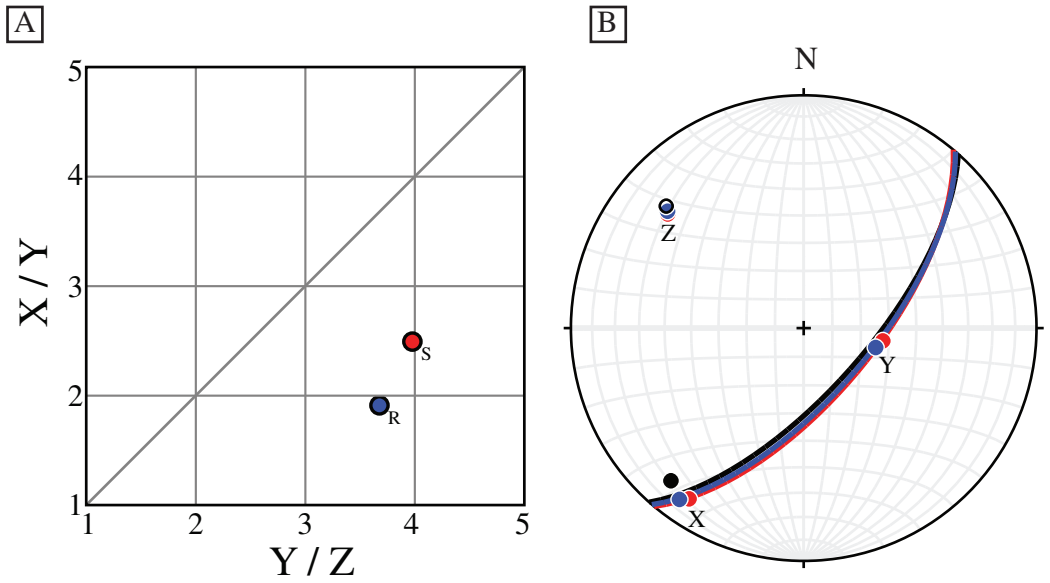


**Figure 20: A)** Flinn diagram of 34 strained clasts from the outcrop shown in figure 16, which plots within the flattening strain regime using the Robin method (blue circle labelled with an "R") (Robin, 2002) and the Shan method (red circle labelled with an "S"). **B)** Stereoplot of the calculated strain axes using EllipseFit (Volmer, 2018) using the Shan method (red) and the Robin method (blue) and their corresponding (X-Y) foliation planes. The average foliation plane (black arc), pole to that plane (hollow black circle), and average lineation (black circle) from the outcrop.

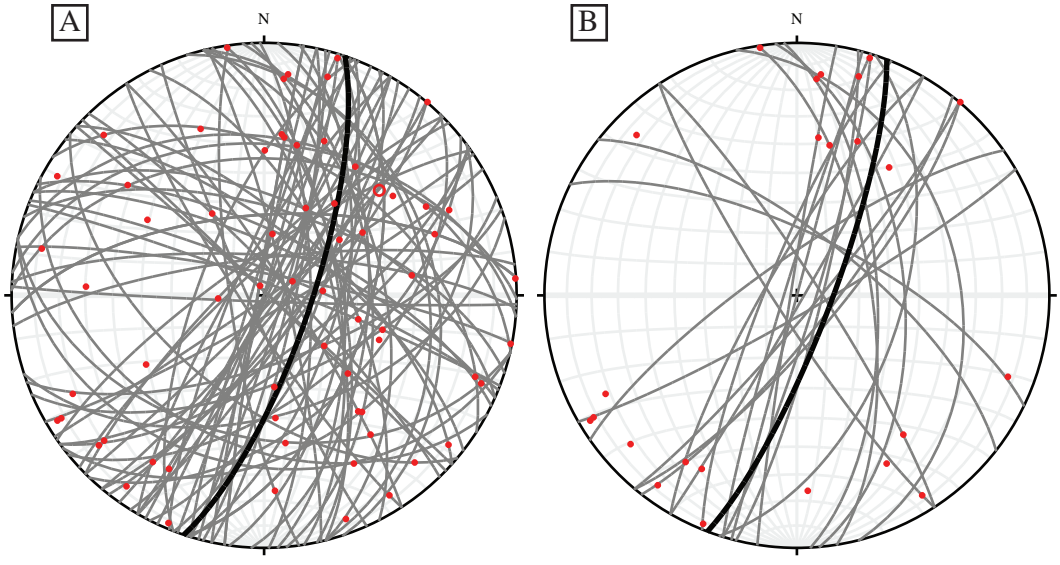


**Figure 21: A)** Stereoplot of all small-scale faults (gray arcs) and all slickenlines (red circles) with the average fault plane orientation (bold black arc) and the average slickenline (large hollow red circle). **B)** Stereoplot of sinistral small-scale faults (gray arcs) and sinistral slickenlines (red circles) and the average sinistral fault (bold black arc).

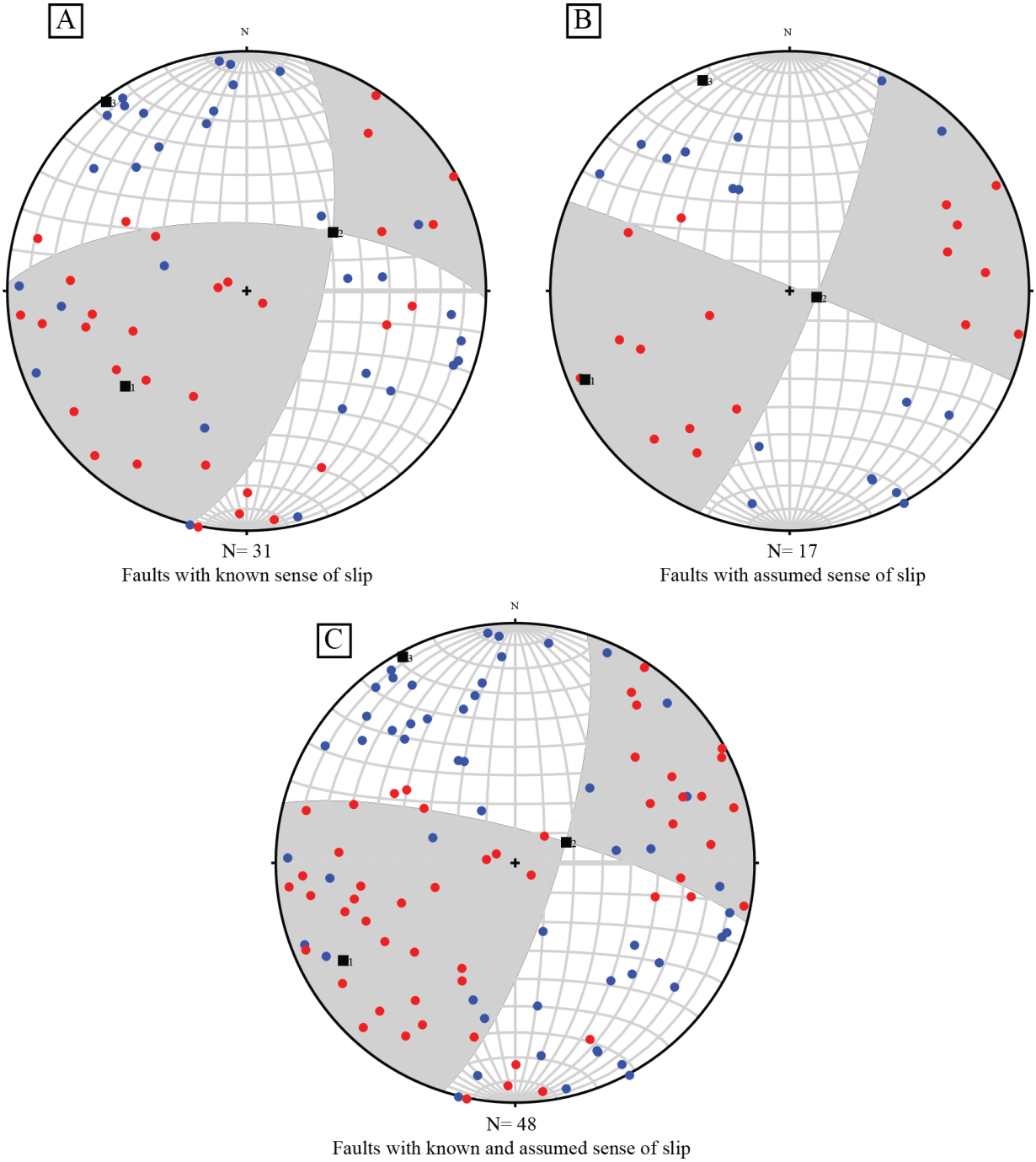


**Figure 22:** Black squares are kinematic axes for the 3 groups of faults **A)** stereoplot of P and T axes for faults with field-determined slip sense with the Linked Bingham fault plane solutions (sinistral plane: 014/64 E, slickenlines: 23/182). **B)** stereoplot of P and T axes for faults with assumed slip sense based on geometric similarity and/or kinematic compatibility with the Linked Bingham fault plane solutions (sinistral plane: 022/81 E, slickenlines: 02/202). **C)** stereoplot of P and T axes for faults with known and assumed slip sense with the Linked Bingham fault plane solutions (sinistral plane: 018/76 E, slickenlines: 12/195).

Allmendinger, 1990) of 022/81 E with a slickenline orientation of 02/202 (Fig. 22b); and the combined known and assumed Linked Bingham fault plane solution (Marrett and Allmendinger, 1990) is 018/76 E with a slickenline orientation of 12/195 (Fig. 22c).

The W-dipping normal fault in the southeastern part of the study area (Plate 1) may be associated with the Neogene normal faulting along the Paposo fault. Neogene normal faulting affected the entire Paposo fault, creating the 100–400 m-high escarpment on the western side, but in the study area it did not rework the gouge fabrics, which still preserve Mesozoic sinistral slip. We did observe one subvertical apparent SE-side-down fault within alluvium, but this structure could be associated with gravity-driven slumping.

The gouge zone that defines the Paposo fault core has well-preserved scaly foliation with prominent S, C, and C' shear bands indicative of sinistral shear (Figs. 7f and 23). The majority of


**Figure 23:** Photo of an S-C fabric with a granodiorite clast from the Early Jurassic granodiorite. The C fabrics are highlighted by faint blue dashed lines and the S fabrics are highlighted by faint red dashed lines.

the slickenlines in the gouge zone are associated with sinistral or sinistral/SE-up slip, but one slip surface has down-dip slickenlines which could record reverse slip. Gouge zones on hill slopes dip moderately into the slope, whereas fabrics exposed in near level areas typically dip >70° NE. We assume that there has been some downhill creep that has shallowed the foliation dip of gouge slope exposures, so these data were removed when calculating the average gouge foliation which is 027/82 E (Fig. 24). The kinematic data from small-scale faults and the gouge zone both indicate that sinistral shear with a component of reverse (E-side-up) slip was dominant along the southern Paposo fault segment.

Epidote veins measured throughout the eastern side of the fault have variable orientations, but the maximum eigenvector of pole to veins is subparallel to the average stretching lineation for

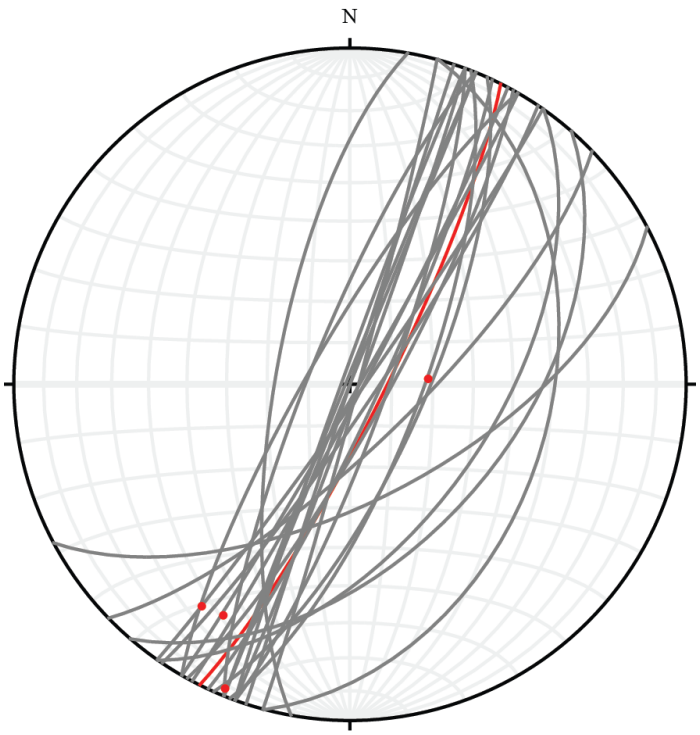


**Figure 24:** Stereoplot of all brittle gouge fabrics (gray arcs) and slickenlines (red circles) with the average brittle gouge fabric plotted as a red arc.

the shear zone (Fig. 25). A cylindrical best fit of the poles to the data suggests multiple extension directions along a plane subparallel to the Paposo fault. This pattern is consistent with flattening strain along the Paposo fault.

## 1.6.Discussion

### *1.6.1. Geometry of map units and mylonitic fabrics*

The southern segment of the Paposo fault consists of a steeply ESE-dipping shear zone, which juxtaposes a brittlely deformed Early Jurassic granodiorite west of the fault against brittlely overprinted mylonitic Late Jurassic to Early Cretaceous granitoids east of the fault (Plate 1). These units and their subdivisions roughly parallel the trend of the Paposo fault. This geometric relationship suggests that emplacement of the Early Cretaceous tonalite and development of the hydrothermally-altered high strain zone were structurally controlled by the shear zone.

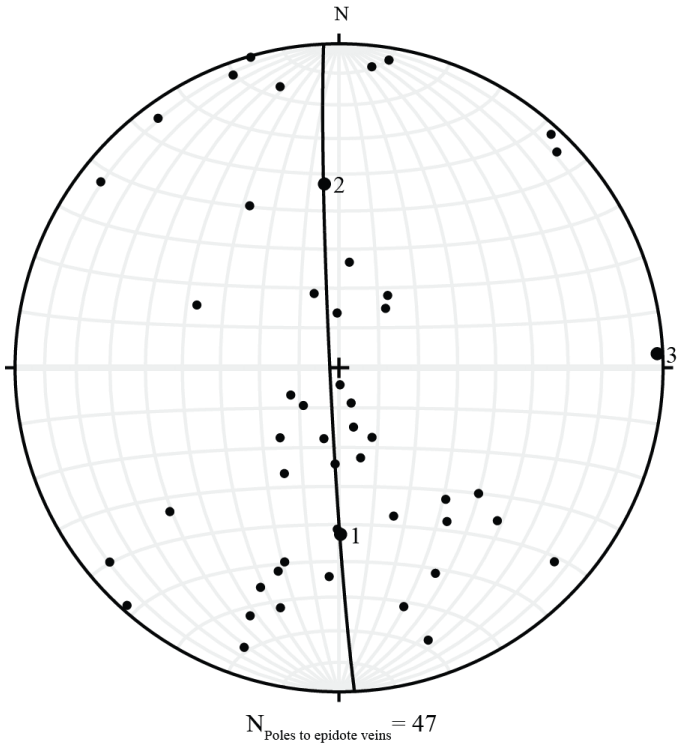


**Figure 25:** Stereoplot of poles to epidote veins (black circles). The arc is a cylindrical best fit to the data and the maximum (1), intermediate (2), and minimum (3) eigenvectors are plotted as larger black circles.

The average foliation of all mylonite zones is 041/63 SE, which is ~23° clockwise from the average strike of the Paposo fault and the mean fault plane solution from small-scale faults (Figs. 12 and 21). The obliquity between the mylonitic foliation and the fault is consistent with overall sinistral shear. The average foliation orientation in mylonites is 039/61 SE, whereas the average foliation in protomylonite is 052/68 SE (Fig. 13a). The larger angle between the protomylonitic foliation and the fault is consistent with counterclockwise rotation of the finite strain axes during progressive sinistral shear. In addition, there is some evidence for counterclockwise rotation of protomylonite foliations to parallelism with the shear zone closer to the Paposo fault (Plate 1, Fig. 15).

### *1.6.2. Timing of deformation*

Mylonitic deformation along the southern segment of the Paposo fault zone is bracketed between ~147 and 117 Ma based on zircon U-Pb ages of the mylonitic LJ granodiorite (146.5 ± 1.1 Ma) and high strain aplite (142.5 ± 1.3 Ma) and the zircon (U-Th)/He cooling age of 116.6 ± 5.4 Ma from the ~147 Ma granodiorite (Figs. 10b, 6c, and 8b) (Appendix 1 and 2). We attribute the lack of penetrative strain in the EJ granodiorite west of the Paposo fault to the fact that this unit was emplaced well before deformation initiated. That is, the EJ granodiorite was most likely cold and strong when the synkinematic EK plutons were hot and weak. The EK plutons may only be able to deform ductilely while they are still cooling. The 139 Ma granodiorite is unstrained where dated but is similar in appearance to granodiorite with discrete high strain zones, consistent with the hypothesis that most strain is post-139 Ma. Also, since the dated aplite sill is very high strain and probably prekinematic, the maximum age of deformation, is likely less than the weighted mean age of the aplite sill (142.5 ± 1.3 Ma) (Fig. 6c; Appendix 1 and 2).

We know the EK tonalite is younger than the LJ-EK granodiorite from zircon ages and the lack of mafic dikes and hydrothermal alteration that characterize the LJ-EK granodiorite. Mafic dike intrusion thus must have occurred between emplacement of the ~139 Ma granodiorite and the ~136 Ma tonalite. These dikes are spatially associated with hydrothermal alteration and discrete high strain zones, suggesting alteration and shear zone development were coeval with dike emplacement. Therefore, we can bracket hydrothermal alteration, development of ultramylonite fabrics and discrete high strain zones between ~139 and 136 Ma, within the interval of Early Cretaceous magmatism along the southern Paposo fault. The protomylonitic fabrics in the ~136 Ma EK tonalite must have formed after the main episode of alteration and fabric development.

The minimum lower age limit for ductile deformation is ~117 Ma —the approximate age when strained granodiorite cooled below the zircon helium closure temperature of ~180-200° C (Reiners et al., 2002; Tagami et al., 2003; Reiners et al., 2004; Stockli, 2005; Wolfe and Stockli, 2010), which is well below the lower limit for crystal plastic deformation of quartz (e.g.; Sibson, 1977; Stockhert et al., 1999; Stipp et al., 2002). We also believe that this ~117 Ma age is close to the timing of brittle gouge formation because the full width at half maximum for illite clay from the gouge is 0.529- 0.611 $\Delta^{o}2\theta$, which suggests these clays formed in the deep diagenetic zone between 100 to 200 °C, and more likely between 150°C and 200 °C because there is no smectite and the KI plots close to the deep diagenetic zone/low anchizone boundary (Fig. 11) (Verdel et al., 2011). Accordingly, gouge formation was likely coeval or younger than cooling below the zircon He closure temperature. The timing of deformation along the southern segment of the Paposo fault zone is slightly older than the interpreted ages of AFS deformation presented by Scheuber and Gonzalez (1999) and Grocott and Taylor (2002), which are based primarily on K-Ar and $^{40}Ar/^{39}Ar$

cooling ages. However, this age difference could be due to the southern Paposo segment containing older Early Cretaceous plutons which are intricately linked with deformation on the AFS.

### *1.6.3. Regional kinematics of the Paposo fault*

The Paposo fault has a slightly arcuate geometry where it is NNE-trending in the south and NNW-trending in the north (Fig. 1b). Regionally, we see variable kinematics along the Paposo fault segment. In the northern part, brittle fault data suggest sinistral transtension along the subsidiary Bolfin and Jorgillo faults (Cembrano et al., 2005; Veloso et al., 2015). Cembrano et al. (2005) determined that the Caleta Coloso duplex formed as a dilational jog between the Bolfin and Jorgillo faults. Veloso and others (2015) document an overall transtensional sinistral regime with NW compressional and NE tensional principal axes.

In the southern Paposo segment, we examine orientations of brittle and ductile fabrics, recrystallized grain shapes and geometries of deformed clasts to determine the kinematics and strain geometry. Slickenlines on steeply E-dipping sinistral faults and mylonitic lineations in steeply E-dipping sinistral shear zones have an average plunge of 14 and 20 to the SSE, respectively, indicating a minor component of reverse slip. In addition, a discrete reverse shear zone parallel to the Paposo fault and N-S striking shears with coaxial-dominated fabrics are consistent with a component of shortening across the southern portion of the Paposo fault zone. Microstructures such as symmetric porphyroclasts and symmetric grain shape fabrics are common in the hydrothermally-altered high strain zone (Figs. 14c, 16), suggesting this sinistral shear zone also records a component of coaxial shortening. The oblate strain geometry of the mylonitized cataclasite zone is also consistent with coaxial flattening and overall sinistral transpression (Fig. 20a). Due to the steeper lineations within the EK tonalite, we believe that the EK tonalite records transpression via non-coaxial dominated sinistral-reverse shear with a greater reverse component

than the other units. Transpressional strain in the rheologically weaker LJ-EK granodiorite was more partitioned, partly accommodated by sinistral non-coaxial shear and coaxial flattening across the shear zone. All these observations support sinistral transpression on the southern segment of the Paposo fault zone. Transtension and transpression are both consistent with their location along the arcuate Paposo fault. These kinematics are also consistent with the idea that fundamentally the dominant N-S arc-parallel AFS is a zone of sinistral simple shear.

### 1.7.Conclusions

The southern segment of the Paposo fault zone is a steeply ESE- dipping fault that accommodated sinistral transpression. The southern portion of the Paposo fault zone experienced ductile deformation between ~139 Ma and ~117 Ma. Mafic dikes associated with hydrothermal alteration and development of high strain fabrics in granodiorite were emplaced between ~139 and ~136 Ma, and protomylonitic fabrics within the younger tonalite can be bracketed from ~136 Ma to ~117 Ma. Based on XRD data and a zircon (U-Th)/He cooling age, clay gouge zone development associated with sinistral slip on the Paposo fault most likely formed between 150°C and 200°C around 117 Ma. The close timing relationship between pluton emplacement and age of penetrative deformation, as well as the lack of penetrative strain in Early Jurassic granitoids suggests that ductile deformation was localized in hot, rheologically weak plutons. Deformation along the AFS may be fundamentally linked to synkinematic arc magmatism in the Coastal Cordillera.

Evidence for sinistral transpression along the Paposo fault includes oblique sinistral-reverse shear in mylonitic fabrics and brittle faults, and locally symmetric microstructures suggestive of coaxial strain. Transpression and transtension along the southern portion of the Paposo fault are likely controlled by the arcuate geometry of the Paposo segment. Sinistral

transtension along the NNW-trending northern segment and sinistral transpression along the NNE-trending southern segment are consistent with overall sinistral simple shear along the N-S-trending AFS.

# 2. CHAPTER 2: RHEOLOGY OF A BRITTLE-PLASTIC TRANSITION ALONG AN EXHUMED INTRA-ARC STRIKE-SLIP FAULT: AN EXAMPLE FROM THE ATACAMA FAULT SYSTEM, NORHTERN CHILE

## 2.1. Introduction

Knowledge of the rheology, strength, and deformation conditions at the brittle-plastic transition (BPT) of crustal-scale faults is fundamental for understanding fault behavior. Most recent studies on brittle-plastic transitions of major faults have focused on normal-sense shear zones (e.g. Behr and Platt, 2011 and 2013; Gottardi and Teyssier, 2013; Singleton et al., 2018) and thrust shear zones (e.g. Kidder et al., 2012; Kjøll et al., 2015), but studies on strike-slip shear zones are less common due to the lack of their exposed ductile roots. Studies of the brittle-plastic transitions of strike-slip shear zones have been done on the Alpine fault (Toy et al., 2008), Karakoram fault (Rutter et al., 2007; Wallis et al., 2015), and the Tonale fault zone (Stipp et al., 2002; Stipp and Kunze, 2008). However, these faults may not be representative of the majority of strike-slip faults because the Alpine fault has a large component of reverse shear, the Karakorum fault deforms metasedimentary rocks, and the Tonale fault deforms a contact aureole with a large lateral temperature gradient parallel to the fault.

Similar to strike-slip faults, there are limited data on the conditions at the BPT for faults within magmatic arcs. Shear zones within magmatic arcs have been studied but lacked detailed constraints on deformation conditions at the BPT (e.g. Avė Lallemant et al., 1985; Busby-Spera and Saleeby, 1990; Tikoff and Saint Blanquat, 1997; Nadin et al., 2016). There is some evidence that intra-arc shear zones are weak. Strain may localize within magmatic arcs because of thermal weakening from an elevated geothermal gradient, hydrolytic weakening, and reaction softening,

but few studies quantify the strength of faults within arcs. In this study we investigate the deformation conditions along a portion of the Atacama fault system.

## 2.2.Geologic background

The Atacama fault system (AFS) is a ~1000 km-long, intra-arc, trench-parallel strike-slip fault that exhibited sinistral slip during Mesozoic oblique subduction (Fig. 1a) (Scheuber and Andriessen, 1990; Brown et al., 1993; Grocott and Taylor, 2002, Cembrano et al., 2005). The AFS lies along the trace of the Jurassic-Early Cretaceous magmatic arc, with most ductile strain accommodated within synkinematic plutons, suggesting there is a relationship between deformation and active magmatism. Brittle-ductile exposures are common along the Paposo segment of the AFS (Fig. 26) (Scheuber and Andriessen, 1990; Brown et al., 1993; Grocott and Taylor, 2002). These exposures can provide important insight into the deformation conditions and rheology of the AFS.

### *2.2.1. Paposo fault background*

The Paposo fault is an arcuate, sinistral strike-slip fault that forms the main strand of the AFS (Fig. 1b). The southern segment of the Paposo fault is an exceptional exposure of a ductile root of an intra-arc strike-slip fault (Plate 1). It juxtaposes an Early Jurassic granodiorite with Early Jurassic (?) metasedimentary rocks against Late Jurassic and Early Cretaceous plutons (Plate 1). In Chapter 1, we discuss the geometry, kinematics, and timing of deformation along the southern segment of the Paposo fault. Based on U-Pb zircon geochronology and (U-Th)/He thermochronology we bracketed mylonitic deformation to ~139 to > ~117 Ma (Chapter 1). Evidence, such as differences in the timing of deformation and amount of hydrothermal alteration, suggests the presence of two episodes of shear along the southern Paposo fault segment.

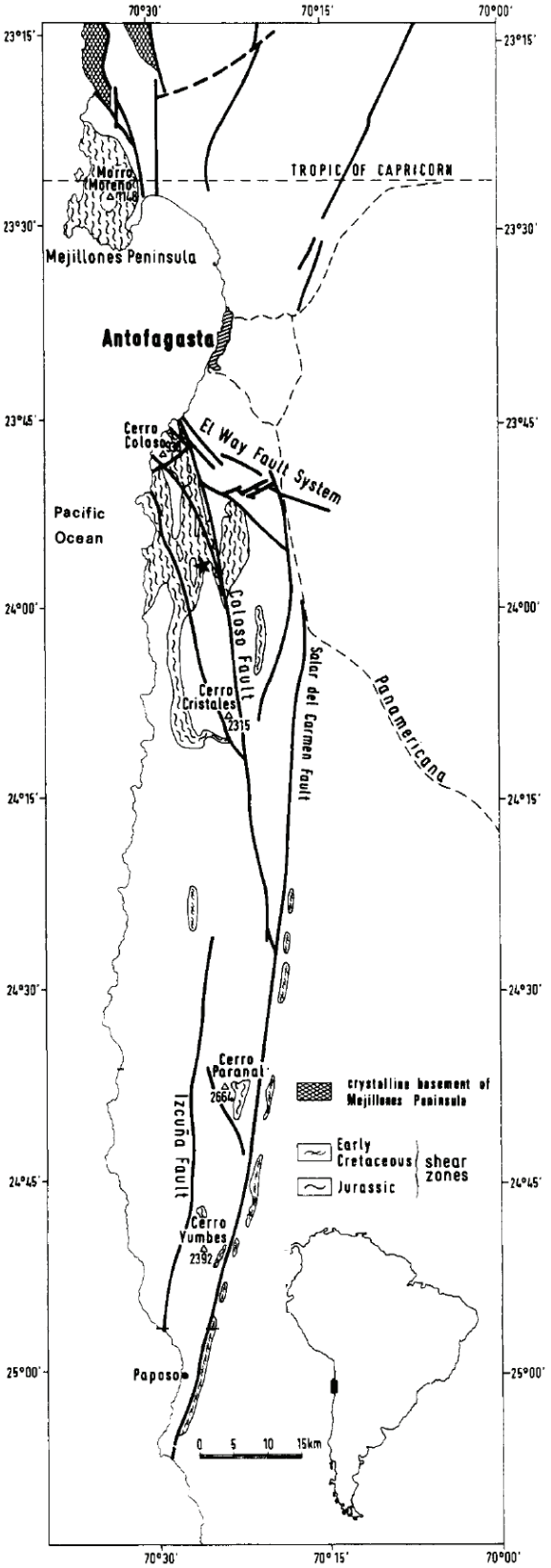


**Figure 26:** Occurrences of sheared rocks along the Paposo segment of the Atacama fault system. From Scheuber and Andriessen, 1990.

Shear zone A is defined by mylonitization of the Early Cretaceous to Late Jurassic granodiorite linked with hydrothermal alteration and areas of discrete high strain spatially associated with mafic dikes. This spatial association suggests the mafic dikes played an important role in driving hydrothermal circulation associated with alteration. Both hydrothermal alteration and dike emplacement are spatially associated with shear zones and, therefore, deformation can be dated using the timing of dike emplacement (Chapter 1). The mafic dikes intrude the Late Jurassic-Early Cretaceous granodiorite but do not intrude the Early Cretaceous tonalite that borders the Paposo fault (Chapter 1). This relationship brackets the timing of diking between the ages of the two deformed plutons (Late Jurassic-Early Cretaceous granodiorite: 138.8 ± 1.5 Ma (Fig. 6b); Early Cretaceous tonalite: 136.0 ± 1.6 Ma (Fig. 6d) (Chapter 1) (Appendix 1 and 2). Shear zone B, within the Early Cretaceous tonalite, lacks significant hydrothermal alteration and is characterized primarily by protomylonitic fabrics. Based on the emplacement age of the Early Cretaceous tonalite (U-Pb zircon age: 136.0 ± 1.6 Ma (Fig. 6d)) and the time at which adjacent rocks cooled below ~190°C ((U-Th)/He zircon age 116.6 ± 5.4 Ma (Fig. 8b), we were able to determine that deformation occurred between ~136-117 Ma (Chapter 1) (Appendix 1 and 2). In this chapter, we study the conditions of deformation along these two shear zones.

## 2.3.Methods

### *2.3.1. Thin sections*

Oriented samples were collected in the field and marked with corresponding GPS waypoints. Samples were cut into thin section billets, parallel to lineation and perpendicular to foliation (parallel to the X:Z planes). We have 38 oriented thin sections made from 33 unique samples (Appendix 3). Thin sections were noted for mineral composition, shear sense indicators, quartz dynamic recrystallization type and grain size, as well as other microstructural and

compositional observations. Dynamic recrystallized quartz grain size and angle of oblique grain shape fabrics were measured using the program ImageJ.

### *2.3.2. Electron backscatter diffraction analyses*

Electron backscatter diffraction (EBSD) analyses were performed on two protomylonite samples from the Early Cretaceous (EK) tonalite, a sample of a dynamically recrystallized quartz vein, and five samples from the hydrothermally-altered Late Jurassic-Early Cretaceous (LJ-EK) granodiorite. Pole figures for quartz and misorientation maps were collected for each sample. EBSD data were collected on an environmental scanning electron microscope (ESEM) at the USGS microbeam laboratories in Denver, Colorado. Data were collected with an accelerating voltage of 15 KeV, a working distance of ~15 mm, and various step sizes depending on the sample. Various step sizes were used because different pixel resolution was needed for each sample depending on the recrystallized grain size. We used a step size of 1 µm for samples 16-1-P30a (hydrothermally-altered zone), 17-1-P6 (EK tonalite), 17-1-P50 (EK tonalite), a step size of 2.5 µm for sample 17-1-P45 (hydrothermally-altered zone) and 17-1-P95 (hydrothermally-altered zone), a step size of 3.5 µm for 17-1-P9, a step size of 5 µm for 16-1-P23a (hydrothermally-altered zone), and a step size of 15 µm for 17-1-P79 (quartz vein). For each sample, minerals were indexed for analysis based on petrographic observations and multiple feldspar species were indexed to account for compositional differences. Data were collected using Aztec software by Oxford Instruments and analyzed using MTEX 5.0.3 software for Matlab.

### *2.3.3. Geochemical methods*

Whole rock major and trace element geochemistry analyses were collected for unstrained protoliths, hydrothermally-altered and adjacent relatively unaltered rock pairs, strained clast and matrix pairs from outcrop P43 within the hydrothermally-altered zone, unpaired hydrothermally-

altered samples, a clay gouge sample, and a mafic dike sample (Plate 1 and Table 1). In total, 20 samples were analyzed and details for each sample are included in Table 1. Samples were prepared by first hammering the rocks into smaller pieces with folded-over butcher paper to protect against contamination from the steel hammer. The cleanest chips without weathered surfaces were selected and placed in a ball mill and powdered. Five grams of the samples were sent to ALS Global Geochemistry Analytical Lab in Reno, Nevada. All samples were analyzed for major elements (ALS package ME-ICP06) and trace elements (ALS package ME-MS81). ME-ICP06 is a method using fused bead and acid digestion with inductively coupled plasma atomic emission spectrometry (ICP-AES) to measure the major element concentrations ($Al_2O_3$, BaO, CaO, $Cr_2O_3$, $Fe_2O_3$, $K_2O$, MgO, MnO, $Na_2O$, $P_2O_5$, $SiO_2$, SrO, $TiO_2$, and LOI) (ALS, 2018). ME-MS81 is a method using fused bead and acid digestion with inductively coupled plasma mass spectrometry (ICP-MS) to measure the amounts of trace elements (Ba, Ce, Cr, Cs, Dy, Er, Eu, Ga, Gd, Hf, Ho, La, Lu, Nb, Nd, Pr, Rb, Sm, Sn, Sr, Ta, Tb, Th, Tm, U, V, W, Y, Yb, Zr) (ALS, 2018).

To estimate volume loss and interpret the relative loss or gain of major elements between unaltered and altered pairs, we constructed isocon plots with the assumption that $Al_2O_3$, $TiO_2$, and Zr are immobile. However in some samples, Zr plots far off lines through $Al_2O_3$ and $TiO_2$ and is likely due to an inhomogeneous distribution of Zr. This could result in an overestimation of volume change.

### *2.3.4. Fluid inclusions*

Fluid inclusion data were collected on a dilational quartz vein from one sample. These quartz veins are believed to have formed at the brittle-plastic transition during deformation because of their orientation and undulose extinction present in the quartz crystals. Fluid inclusion trails were identified and documented using an optical microscope. Then using a microthermometry

**Table 1:** List of samples for geochemical analyses, UTM coordinates (WGS84) where samples were collected, the unit they were collected from, numbers denoting pairs of samples compared, and a short description of the sample. The "Sample pairs for analyses" column lists sample pairs. Samples with matching numbers were compared to each other in isocon plots. For example, samples 161-P30b.1 and 17-1-P120 both have the number 9 so they were compared in an isocon plot. Samples with multiple numbers were compared to multiple samples.

| Sample Name | UTM Y | UTM X | Unit | Sample pairs for analyses | Nature of Sample |
|---|---|---|---|---|---|
| 161-P32 | 7232154 | 355594 | Unstrained LJ granodiorite | | Undeformed protolith |
| 161-P30b.1 | 7232569 | 354620 | Hydrothermally altered zone | 9 | Mafic material from outcrop P43 |
| 161-P30b.2 | 7232569 | 354620 | Hydrothermally altered zone | | Granodiorite material from outcrop P43 |
| 17-1-P6 | 7231889 | 353768 | EK tonalite | 12 | Protomylonite |
| 17-1-P26 | 7231061 | 354971 | Unstrained EK granodiorite | 4, 5, 6, 7, 8 | Protolith |
| 17-1-P43a | 7232544 | 354603 | Hydrothermally altered zone | 10 | Mafic material from outcrop P43 |
| 17-1-P43b-1 | 7232544 | 354603 | Hydrothermally altered zone | 11 | Mafic material from outcrop P43 |
| 17-1-P43b-2 | 7232544 | 354603 | Hydrothermally altered zone | | Granodiorite material from outcrop P43 |
| 17-1-P56 | 7232935 | 354245 | Hydrothermally altered zone | 4 | High strain mylonite |
| 17-1-P95 | 7229889 | 353484 | Hydrothermally altered zone | 5 | High strain mylonite |
| 17-1-P112 | 7231898 | 353714 | Gouge zone | | Foliated gouge |
| 17-1-P120 | 7232471 | 354543 | Hydrothermally altered zone | 9, 10, 11 | Unstrained Mafic Dike |
| 18-1-PJ58A | 7232186 | 354070 | Hydrothermally altered zone | 1 | Low strain unaltered pair |
| 18-1-PJ58Ab | 7232186 | 354070 | Hydrothermally altered zone | 1, 6 | High strain altered pair |
| 18-1-PJ59 | 7232120 | 354066 | Hydrothermally altered zone | 2 | Low strain less altered pair |
| 18-1-PJ59b | 7232120 | 354066 | Hydrothermally altered zone | 2, 7 | High strain altered pair |
| 18-1-PJ60 | 7232258 | 354089 | Hydrothermally altered zone | 3 | Low strain less altered pair |
| 18-1-PJ60b | 7232258 | 354089 | Hydrothermally altered zone | 3, 8 | High strain altered pair |
| 18-1-PJ73 | 7232069 | 353936 | EK tonalite | 12, 13 | Protolith |
| 18-1-PJ80 | 7231950 | 353772 | EK tonalite | 13 | High strain mylonite |

stage on an optical microscope, the fluid inclusions were then frozen and reheated slowly to room temperature to determine the salinity of the inclusion trails and then heated above room temperature to the point of homogenization.

### 2.4.Shear zone in Late Jurassic-Early Cretaceous granodiorite (shear zone A)

#### *2.4.1. Characteristics of shear zone A*

Shear zone A is ~610-1060 m across and affects the deformed units within the Late Jurassic-Early Cretaceous granodiorites, which are medium-grained (~1-4 mm) with ~20-25% quartz and ≤11% biotite. These granodiorites are subdivided into a hydrothermally-altered mylonite zone, a zone of mylonitic and nonmylonitic rocks with >50% mylonite, a <50% mylonite, and an unstrained zone (Plate 1). In outcrop, rocks from the hydrothermally-altered mylonite zone are white or light tan and have a small amount of mafic minerals, if any. Alteration in this zone is typically heterogeneous (Fig. 27), and the less-altered regions are lower strain than the more

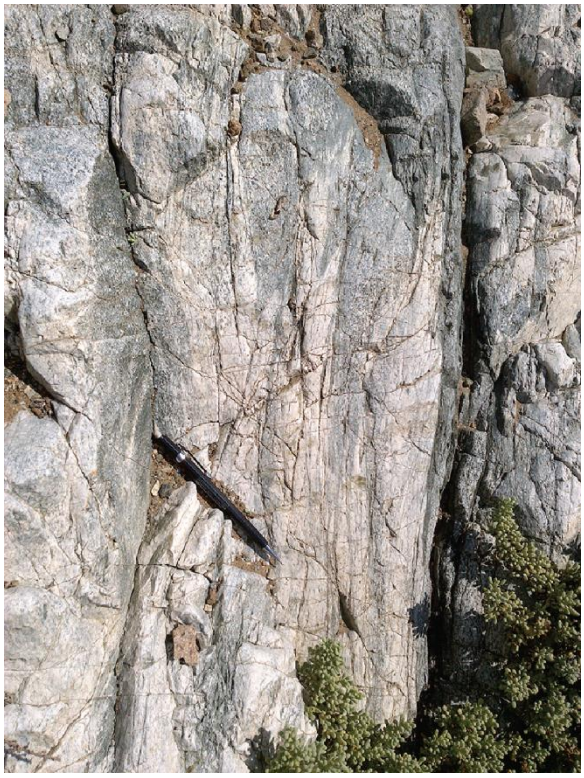

**Figure 27:** Outcrop photo of a heterogeneously hydrothermally altered area. The more hydrothermally altered areas (lighter areas) are higher strain than the less hydrothermally altered areas.

altered, higher strain regions, based on outcrop and microstructural observations, which suggests that hydrothermal alteration weakened the rock and facilitated penetrative deformation or vice versa. The >50% mylonite zone contains ~10-150 cm-thick high strain regions adjacent to thinner areas of undeformed granodiorite. The <50% mylonite zone contains ~1-10 cm-thick high strain zones usually located at the margins of mafic dikes (Figs. 7c and 28) within thicker packages of undeformed granodiorite. This relationship suggests fluid flow and mafic dike intrusion played an important role in deformation along this zone (Fig. 7c and 28). All of these observations suggest that the deformation in this zone is linked to hydrothermal alteration and dike emplacement.

Zircon U-Pb ages from two samples within this map unit are 138.8 ± 1.5 Ma and 146.5 ± 1.1 Ma (Chapter 1, Figs. 6b and 10b, Appendix 1 and 2). Both plutonic bodies are intruded by mafic dikes, which are associated with hydrothermal alteration and deformation. These mafic dikes are not present in the Early Cretaceous tonalite, so the age of deformation, hydrothermal alteration, and dike emplacement must be between ~139-136 Ma.

**Figure 28:** Outcrop photo of a discrete shear zone in the less than 50% mylonite zone.

### *2.4.2. Characteristics of hydrothermal alteration*

Hydrothermal alteration plays an important role in deformation in shear zone A. To characterize the alteration, we observed microstructural and outcrop-scale changes and analyzed geochemical changes between: a) spatially associated pairs of less altered and more altered samples and b) the least altered unstrained protolith versus strained samples (Table 2 and 3). In outcrop, the less altered areas of the hydrothermally-altered zone contain more mafic minerals and appear less deformed (Fig. 27). In thin section, there are also fewer mafic minerals by volume, if any, more feldspar alteration and secondary white mica, more veinlets and veins, and more quartz-rich regions in hydrothermally altered samples than less hydrothermally altered samples (Figs. 29a, b).

Geochemical analyses of the less altered versus more altered pairs indicate a relative loss of major elements ($SiO_2$, $Na_2O$, CaO, $Fe_2O_3$, MgO, and $K_2O$) compared to the best fit line though immobile elements (Figs. 30a-c). In some plots $SiO_2$, $Na_2O$, and $Al_2O_3$ are slightly increased based on the 1:1 line (Figs. 30a-c). There is also a significant amount of volume loss between the less and more altered pairs ranging from -10.9% to -72.4% based on the slope of a best fit line though the assumed immobile elements, Zr, $Al_2O_3$, and $Ti_2O$ (Figs. 30a-c). However, in plots in figure 30 b and c, Zr plots far off the $Al_2O_3$ and $TiO_2$ lines, so the isocon may be misinterpreted and the volume change may be overestimated. The composition of a sample of unaltered/unstrained protolith compared with altered samples show a relative gain of $SiO_2$, $Na_2O$, and CaO, and a relative loss of MgO, $Fe_2O_3$, and $K_2O$ (Figs. 31a-e). However, it is possible that the unaltered protolith, sampled from the granodiorite with an age of ~139 Ma, does not represent the original composition of all of the strained samples, because the protolith for these strained samples may be

**Table 2:** Table of major element concentrations for all geochemical samples.

| SAMPLE | SiO2 | Al2O3 | Fe2O3 | CaO | MgO | Na2O | K2O | Cr2O3 | TiO2 | MnO | P2O5 | SrO | BaO | LOI | Total |
|---|---|---|---|---|---|---|---|---|---|---|---|---|---|---|---|
| DESCRIPTION | % | % | % | % | % | % | % | % | % | % | % | % | % | % | % |
| 161-P32 | 70 | 15.9 | 3.24 | 2.25 | 0.89 | 4.34 | 3.64 | <0.01 | 0.39 | 0.05 | 0.09 | 0.02 | 0.06 | 0.82 | 102 |
| 161-P30b.1 | 56 | 17.7 | 8.36 | 6.87 | 3.53 | 5.41 | 0.59 | <0.01 | 0.96 | 0.05 | 0.22 | 0.05 | 0.01 | 1.84 | 102 |
| 161-P30b.2 | 67.3 | 15.3 | 3.57 | 4.8 | 1.39 | 5.41 | 0.56 | <0.01 | 0.91 | 0.04 | 0.33 | 0.05 | 0.01 | 1.49 | 101 |
| 17-1-P6 | 69.6 | 17 | 1.91 | 2.99 | 0.9 | 4.75 | 2.01 | <0.01 | 0.3 | 0.03 | 0.11 | 0.05 | 0.06 | 1.2 | 101 |
| 17-1-P26 | 65.2 | 16.6 | 4.54 | 3.32 | 1.7 | 4.36 | 2.69 | <0.01 | 0.49 | 0.08 | 0.11 | 0.03 | 0.05 | 1.37 | 101 |
| 17-1-P43a | 39 | 21.6 | 17.4 | 2.21 | 5.94 | 1.92 | 0.39 | 0.01 | 0.68 | 0.02 | 0.23 | 0.05 | 0.01 | 2.41 | 91.9 |
| 17-1-P43b-1 | 52.6 | 19.8 | 8.19 | 2.33 | 5.16 | 1.99 | 0.56 | <0.01 | 0.48 | 0.01 | 0.15 | 0.04 | 0.01 | 2.42 | 93.7 |
| 17-1-P43b-2 | 50.7 | 16.8 | 8.79 | 8.85 | 4.75 | 4.9 | 0.69 | 0.01 | 0.89 | 0.04 | 0.12 | 0.04 | 0.01 | 2.34 | 98.9 |
| 17-1-P56 | 72.8 | 12.5 | 1.32 | 5.6 | 1.63 | 3.75 | 0.2 | <0.01 | 0.51 | 0.03 | 0.16 | 0.04 | <0.01 | 2.09 | 101 |
| 17-1-P95 | 71.9 | 16.1 | 1.06 | 4.26 | 0.86 | 4.09 | 0.7 | <0.01 | 0.34 | 0.04 | 0.07 | 0.04 | 0.01 | 2 | 101 |
| 17-1-P112 | 58.6 | 17.5 | 7.12 | 2.48 | 2.32 | 1.55 | 3.78 | 0.01 | 0.8 | 0.09 | 0.14 | 0.01 | 0.01 | 6.95 | 101 |
| 17-1-P120 | 49 | 21.2 | 8.57 | 8.08 | 5.95 | 2.93 | 1.32 | 0.01 | 0.61 | 0.1 | 0.11 | 0.05 | 0.03 | 3.38 | 101 |
| 18-1-PJ58A | 57.9 | 18.65 | 2.96 | 8.87 | 4.53 | 4.44 | 0.51 | <0.01 | 0.72 | 0.06 | 0.12 | 0.06 | 0.01 | 1.54 | 100.4 |
| 18-1-PJ58Ab | 65.5 | 19.85 | 0.54 | 7.18 | 0.69 | 4.61 | 0.26 | <0.01 | 0.86 | 0.01 | <0.01 | 0.06 | <0.01 | 1.19 | 100.8 |
| 18-1-PJ59 | 60.2 | 18.65 | 2.37 | 8.2 | 3.7 | 4.51 | 0.71 | <0.01 | 0.77 | 0.07 | 0.12 | 0.05 | 0.01 | 1.56 | 100.9 |
| 18-1-PJ59b | 70.3 | 15.7 | 0.61 | 6.92 | 1.22 | 3.17 | 0.27 | <0.01 | 0.38 | 0.03 | 0.01 | 0.04 | <0.01 | 1.37 | 100 |
| 18-1-PJ60 | 56.2 | 18.7 | 3.28 | 8.91 | 4.33 | 4.67 | 0.68 | <0.01 | 1.26 | 0.06 | 0.23 | 0.07 | 0.01 | 1.79 | 100.2 |
| 18-1-PJ60b | 54.3 | 27.7 | 0.37 | 9.68 | 0.38 | 5.7 | 0.41 | <0.01 | 0.78 | 0.02 | <0.01 | 0.08 | 0.01 | 1.24 | 100.7 |
| 18-1-PJ73 | 53.9 | 19.15 | 7.41 | 7.92 | 4.72 | 4.23 | 0.6 | 0.01 | 0.75 | 0.16 | 0.17 | 0.08 | 0.02 | 1.88 | 101 |
| 18-1-PJ80 | 69.7 | 16.05 | 1.96 | 3.22 | 0.69 | 4.38 | 2.6 | <0.01 | 0.32 | 0.03 | 0.1 | 0.04 | 0.06 | 1.05 | 100.2 |

**Table 3:** Table of trace element concentrations for all geochemical samples.

| SAMPLE | Ba | Ce | Cr | Cs | Dy | Er | Eu | Ga | Gd | Hf | Ho | La | Lu | Nb | Nd | Pr | Rb | Sm | Sn | Sr | Ta | Tb | Th | Tm | U | V | W | Y | Yb | Zr |
|---|---|---|---|---|---|---|---|---|---|---|---|---|---|---|---|---|---|---|---|---|---|---|---|---|---|---|---|---|---|---|
| DESCRIPTION | ppm | ppm | ppm | ppm | ppm | ppm | ppm | ppm | ppm | ppm | ppm | ppm | ppm | ppm | ppm | ppm | ppm | ppm | ppm | ppm | ppm | ppm | ppm | ppm | ppm | ppm | ppm | ppm | ppm | ppm |
| 161-P32 | 484 | 35.6 | 10 | 2.03 | 4.76 | 2.51 | 0.97 | 18.9 | 4.31 | 7.7 | 0.95 | 15.3 | 0.43 | 5 | 20.5 | 4.89 | 101 | 4.51 | 1 | 195.5 | 0.4 | 0.71 | 10.85 | 0.43 | 1.71 | 49 | 1 | 24.9 | 2.85 | 281 |
| 161-P30b.1 | 76.4 | 60.2 | 30 | 1.43 | 6.28 | 3.63 | 1.46 | 22 | 6.88 | 8.3 | 1.37 | 28.6 | 0.5 | 6.9 | 33.5 | 7.97 | 19.5 | 7.91 | 2 | 437 | 0.4 | 1.07 | 12.4 | 0.51 | 3.12 | 372 | 1 | 33.6 | 3.89 | 337 |
| 161-P30b.2 | 64.7 | 73.1 | 10 | 1.31 | 7.33 | 3.69 | 1.26 | 17.6 | 7.94 | 15 | 1.59 | 31.2 | 0.61 | 16.1 | 37.4 | 9.39 | 16.6 | 8.1 | 2 | 424 | 1.2 | 1.26 | 42.3 | 0.61 | 4.04 | 200 | 1 | 39 | 4.01 | 625 |
| 17-1-P6 | 546 | 32.1 | 10 | 0.51 | 1.89 | 1.19 | 0.73 | 16.8 | 2.21 | 3.9 | 0.46 | 16.2 | 0.24 | 4.5 | 13.6 | 3.94 | 40 | 3.25 | 1 | 417 | 0.4 | 0.29 | 5.3 | 0.2 | 1.39 | 34 | 5 | 11.5 | 1.44 | 160 |
| 17-1-P26 | 466 | 38.6 | 20 | 2.03 | 4.37 | 2.4 | 1 | 19.2 | 4.06 | 6.3 | 0.83 | 17.2 | 0.42 | 4.5 | 22 | 5.36 | 63.5 | 4.83 | 2 | 300 | 0.4 | 0.64 | 8.04 | 0.36 | 1.48 | 87 | 1 | 23.9 | 2.57 | 234 |
| 17-1-P43a | 43.2 | 6.9 | 50 | 0.53 | 1.19 | 0.59 | 0.42 | 52 | 1.31 | 1.9 | 0.26 | 3.4 | 0.13 | 1 | 4.6 | 1.08 | 9.9 | 1.08 | 4 | 417 | <0.1 | 0.19 | 2.31 | 0.12 | 1.19 | 597 | 1 | 6.4 | 0.79 | 74 |
| 17-1-P43b-1 | 64.8 | 3.6 | 30 | 0.11 | 0.74 | 0.4 | 0.15 | 41.4 | 0.57 | 2.3 | 0.13 | 1.8 | 0.09 | 0.8 | 2.1 | 0.45 | 12 | 0.85 | 4 | 363 | 0.1 | 0.09 | 1.59 | 0.06 | 0.45 | 495 | <1 | 3.9 | 0.43 | 92 |
| 17-1-P43b-2 | 66 | 18.8 | 50 | 2.53 | 5.53 | 3.38 | 1.4 | 21 | 5.41 | 5.2 | 1.11 | 5.8 | 0.48 | 6.1 | 17.5 | 3.42 | 11.5 | 5.97 | 3 | 301 | 0.5 | 0.91 | 4.52 | 0.52 | 3.3 | 504 | 1 | 28 | 2.99 | 201 |
| 17-1-P56 | 22 | 14 | 30 | 0.42 | 1.41 | 0.72 | 0.47 | 14.2 | 1.48 | 4.8 | 0.27 | 5.6 | 0.16 | 2.7 | 7.1 | 1.92 | 5.3 | 1.79 | 1 | 299 | 0.3 | 0.28 | 56.2 | 0.15 | 3.45 | 87 | 1 | 7.7 | 0.92 | 131 |
| 17-1-P95 | 68.1 | 28.5 | 10 | 3.35 | 2.43 | 1.61 | 0.55 | 16.6 | 2.71 | 5.7 | 0.54 | 9.7 | 0.31 | 4.9 | 16.4 | 4.26 | 26.4 | 3.46 | 1 | 346 | 0.6 | 0.43 | 14.1 | 0.3 | 2.06 | 52 | 1 | 15.6 | 1.84 | 216 |
| 17-1-P112 | 104 | 40.4 | 60 | 14.65 | 3.19 | 1.75 | 0.88 | 19.5 | 3.02 | 5.3 | 0.69 | 18.9 | 0.34 | 5 | 18.7 | 5.18 | 142.5 | 4.23 | 1 | 54.4 | 0.4 | 0.53 | 9.95 | 0.3 | 2.32 | 147 | 1 | 17.2 | 1.97 | 209 |
| 17-1-P120 | 225 | 9.9 | 80 | 1.69 | 1.93 | 1.28 | 0.77 | 21.5 | 2.16 | 1.8 | 0.5 | 3.6 | 0.2 | 1.3 | 7.9 | 1.78 | 56.6 | 2.31 | 1 | 433 | 0.1 | 0.36 | 1.59 | 0.19 | 0.72 | 230 | <1 | 11.2 | 1.3 | 65 |
| 18-1-PJ58A | 84.8 | 32.6 | 10 | 1.81 | 3.64 | 2.32 | 1.03 | 21.6 | 4.15 | 3.2 | 0.73 | 9.1 | 0.34 | 3.5 | 22.9 | 5.28 | 15.7 | 5.33 | 2 | 580 | 0.2 | 0.63 | 6.23 | 0.35 | 2.18 | 261 | 3 | 21.9 | 2.36 | 117 |
| 18-1-PJ58Ab | 50.4 | 39.2 | 30 | 2.49 | 5.6 | 3.35 | 1.29 | 23.8 | 6.38 | 3.8 | 1.13 | 8.8 | 0.49 | 5.8 | 30.8 | 6.87 | 6.9 | 7.59 | 3 | 610 | 0.4 | 0.96 | 6.53 | 0.49 | 3.14 | 121 | 1 | 31.2 | 3.31 | 133 |
| 18-1-PJ59 | 115 | 39.7 | 10 | 2.06 | 4.61 | 2.71 | 1.24 | 22.7 | 4.93 | 3.1 | 0.94 | 12 | 0.42 | 5 | 26.2 | 6.01 | 27 | 6.11 | 2 | 601 | 0.3 | 0.75 | 5.22 | 0.4 | 2.45 | 235 | 1 | 25.9 | 2.79 | 104 |
| 18-1-PJ59b | 46.8 | 19.1 | 10 | 1.1 | 3.06 | 2.06 | 0.54 | 19.2 | 3.29 | 5.8 | 0.67 | 4.6 | 0.32 | 4.8 | 15.2 | 3.3 | 8.7 | 4.22 | 1 | 425 | 0.5 | 0.51 | 7.14 | 0.3 | 1.65 | 89 | <1 | 18.8 | 2.12 | 205 |
| 18-1-PJ60 | 101 | 60.9 | 10 | 1.96 | 5.38 | 3.02 | 2.42 | 22.9 | 7.02 | 4.4 | 1.06 | 19.6 | 0.47 | 8 | 39.4 | 9.16 | 21.3 | 9.03 | 3 | 646 | 0.5 | 0.94 | 5.02 | 0.46 | 2.51 | 277 | 1 | 28.3 | 2.94 | 160 |
| 18-1-PJ60b | 77.9 | 34.9 | 10 | 3.42 | 5.12 | 3.44 | 1.26 | 26.2 | 5.6 | 20.4 | 1.13 | 9 | 0.64 | 7.5 | 26.3 | 5.81 | 13.4 | 6.5 | 2 | 787 | 0.7 | 0.84 | 5.38 | 0.59 | 3.72 | 80 | <1 | 30.9 | 4.01 | 739 |
| 18-1-PJ73 | 192 | 39.5 | 40 | 0.68 | 4.16 | 2.37 | 1.41 | 22.5 | 4.67 | 3.8 | 0.82 | 16.9 | 0.33 | 3.6 | 24 | 5.51 | 15.6 | 5.52 | 1 | 692 | 0.2 | 0.67 | 3.54 | 0.37 | 0.89 | 223 | 1 | 22.3 | 2.32 | 133 |
| 18-1-PJ80 | 546 | 36.9 | 10 | 0.85 | 2.25 | 1.45 | 0.76 | 16.5 | 2.66 | 4.6 | 0.47 | 19.4 | 0.24 | 4.8 | 16.8 | 4.49 | 70.7 | 3.15 | 1 | 431 | 0.5 | 0.37 | 6.38 | 0.22 | 2.06 | 41 | 3 | 13.8 | 1.65 | 175 |

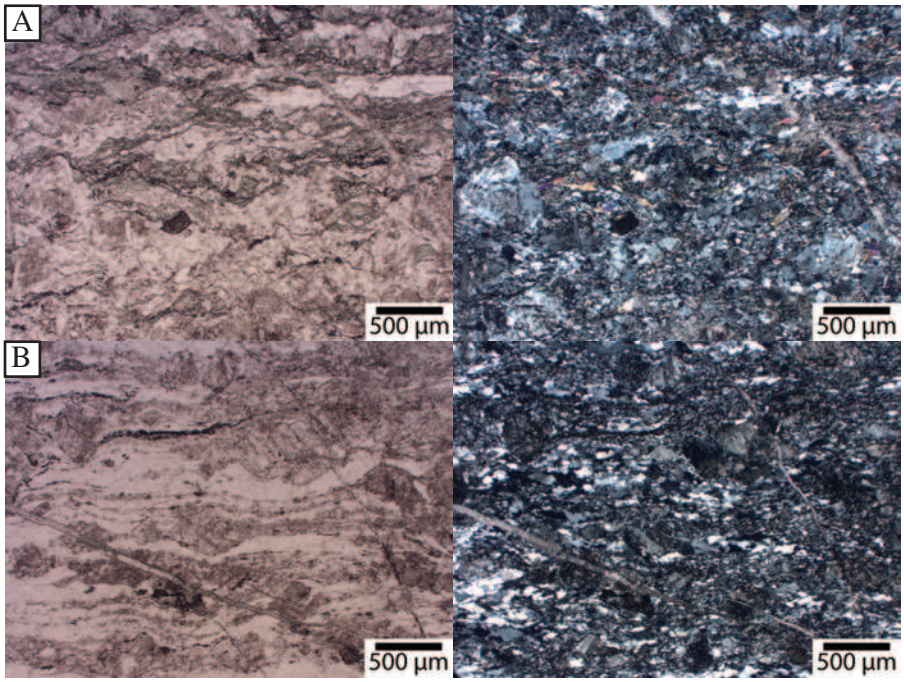


**Figure 29:** Plane-polarized (left) and cross-polarized (right) photomicrographs of **A)** a less hydrothermally altered sample and **B)** a more hydrothermally altered sample. There is more chlorite in the less altered sample and more quartz in the more altered sample. The feldspars in **B)** appear to have a higher portion altered to white mica and sausssurite than feldspars in **A)**.

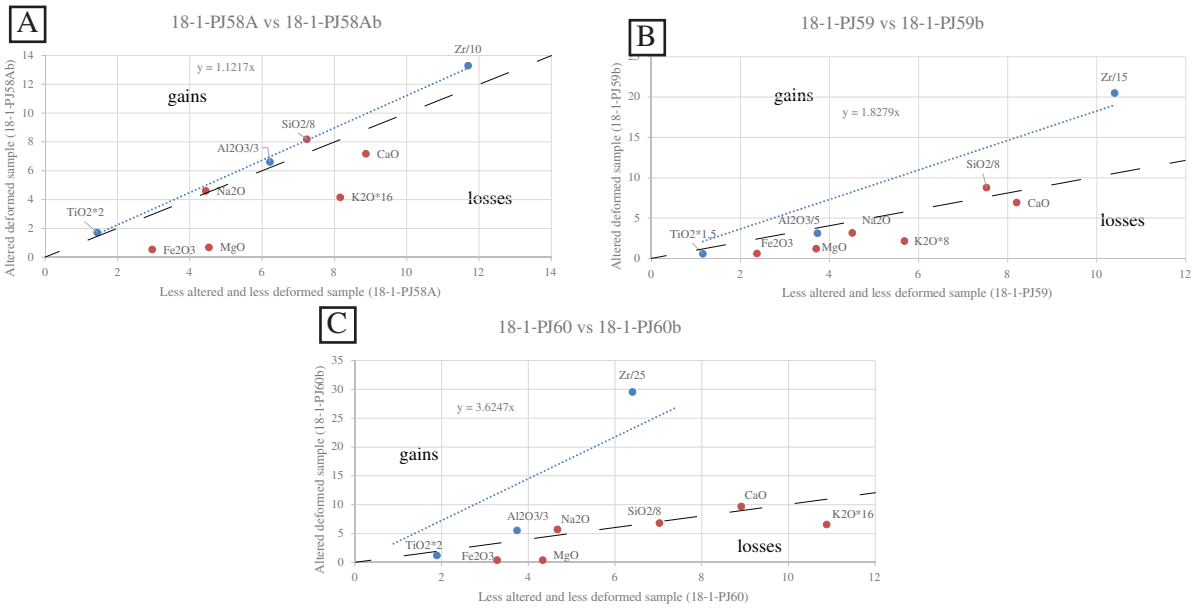


**Figure 30:** Isocon plots for less altered and more altered pairs from shear zone A within the hydrothermally-altered zone. **A)** 18-1-PJ58A vs 18-1-PJ58Ab, **B)** 18-1-PJ59 vs 18-1-PJ59b, and **C)** 18-1-PJ60 vs 18-1-PJ60b. The values are scaled weight percents except for Zr which is a scaled ppm of Zr. The blue circles on each graph are immobile elements, and a best fit trend line of the immobile elements can be used to calculate the change in volume for each sample. Change in volume: **A)** -11%, **B)** -45%, and **C)** -72%. The red circles are mobile elements, which are relatively increased above the blue line and relatively decreased below. The black dashed line is a 1:1 line of constant volume.

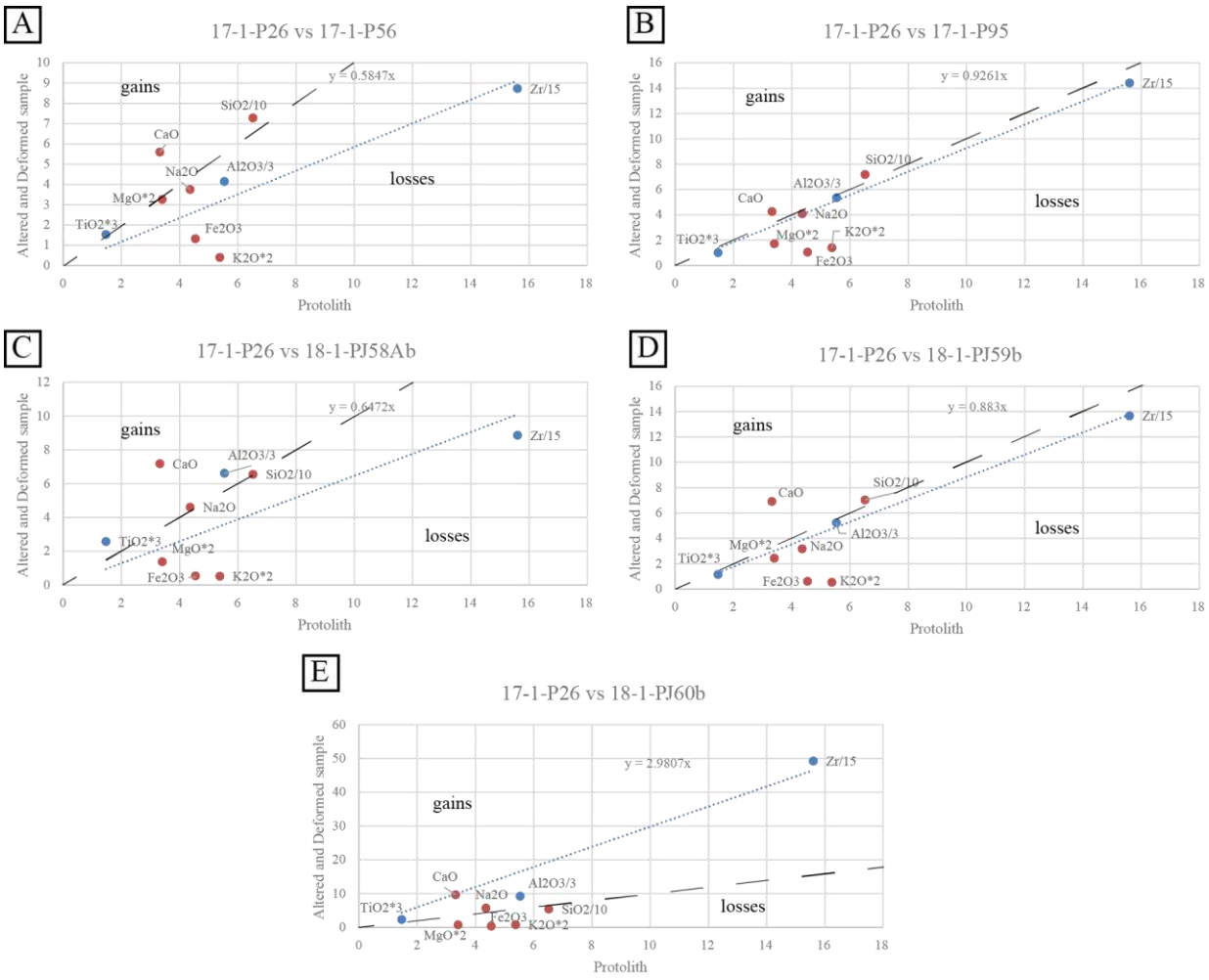


**Figure 31:** Isocon plots for altered and deformed samples vs samples of the protolith from shear zone A. Unstrained Early Cretaceous granodiorite (17-1-P26) is compared to different strained and altered samples from the hydrothermally-altered zone from shear zone A. **A)** 17-1-P26 vs 17-1-P56, **B)** 17-1-P26 vs 17-1-P95, **C)** 17-1-P26 vs 18-1-PJ58Ab, **D)** 17-1-P26 vs 18-1-PJ59b, and **E)** 17-1-P26 vs 18-1-PJ60b. The values are scaled weight percents except for Zr which is a scaled ppm of Zr. The blue circles on each graph are immobile elements, and a best fit trend line of the immobile elements can be used to calculate the change in volume for each sample. Change in volume: **A)** 71%, **B)** 8%, **C)** 55%, **D)** 13%, and **E)** -66%. The area above the blue dashed best fit trend line represents a relative gain and the area below the blue line represents an area of relative loss. The red circles are mobile elements, which are relatively increased above the blue line and relatively decreased below. The black dashed line is a 1:1 line of constant volume.

one of the other LJ-EK granodiorites deformed by shear zone A. We also show all of the trace and major elements on a plot with the data separated into three categories: unaltered, moderately altered, and intensely altered. There is no obvious pattern of alteration in the trace elements, but

we do see an increase in CaO and a decrease in $K_2O$ as alteration intensity increases (Appendix 4). This hydrothermal alteration episode resulted in an overall loss of mafic phases and alteration of feldspar to suassurite and white mica.

### *2.4.3. Microstructures, kinematics, and rheological controls on deformation*

Mylonitic fabrics in shear zone A exhibit sinistral shear, although minor discrete dextral and reverse shears are present in the <50% mylonite unit. The average mylonitic foliation in shear zone A is 038/61 SE and the average stretching lineation is 17/211 (Fig. 12). The majority of the samples from shear zone A have sinistral shear sense indicators (asymmetric porphyroclasts, fractured porphyroclast, and oblique grain shape fabrics) (Figs. 14a and b). However, some samples have symmetric fabrics, and symmetric or conflicting shear sense indicators are common (Fig. 14c).

Within the hydrothermally-altered zone in shear zone A, there is a unique outcrop (P43, Plate 1) with elongate LJ-EK granodiorite clasts within a black matrix (Figs. 19 a, b and 32). The black matrix in thin section contains fine-grained actinolite, fine-grained chlorite, fine-grained plagioclase, and plagioclase porphyroclasts (Fig. 33). The mineralogy of unstrained mafic dikes is also similar. These unstrained dikes contain phenocrysts of hornblende and plagioclase, as well as fine-grained chlorite, hornblende, and plagioclase. When comparing the composition of the mafic material to the unstrained mafic dikes, they have similar concentrations of $SiO_2$, $Fe_2O_3$, MgO, and $Na_2O$ and slightly less $K_2O$ and CaO possibly due to minor alteration during deformation (Tables 2 and 3 and Figs. 34a-c). From these mineralogical and geochemical observations, we assume that the foliated matrix is mafic and is probably a transposed mafic dike (Tables 2 and 3 and Fig. 34a, b, and c). The strained granodioritic clasts are commonly angular and have a wide range of sizes, and in some areas the dark material cuts across the granodiorite, resembling pseudotachylyte (Figs.

**Figure 32:** Outcrop photo of an example of the black material cutting across the granodiorite, resembling pseudotachylyte.

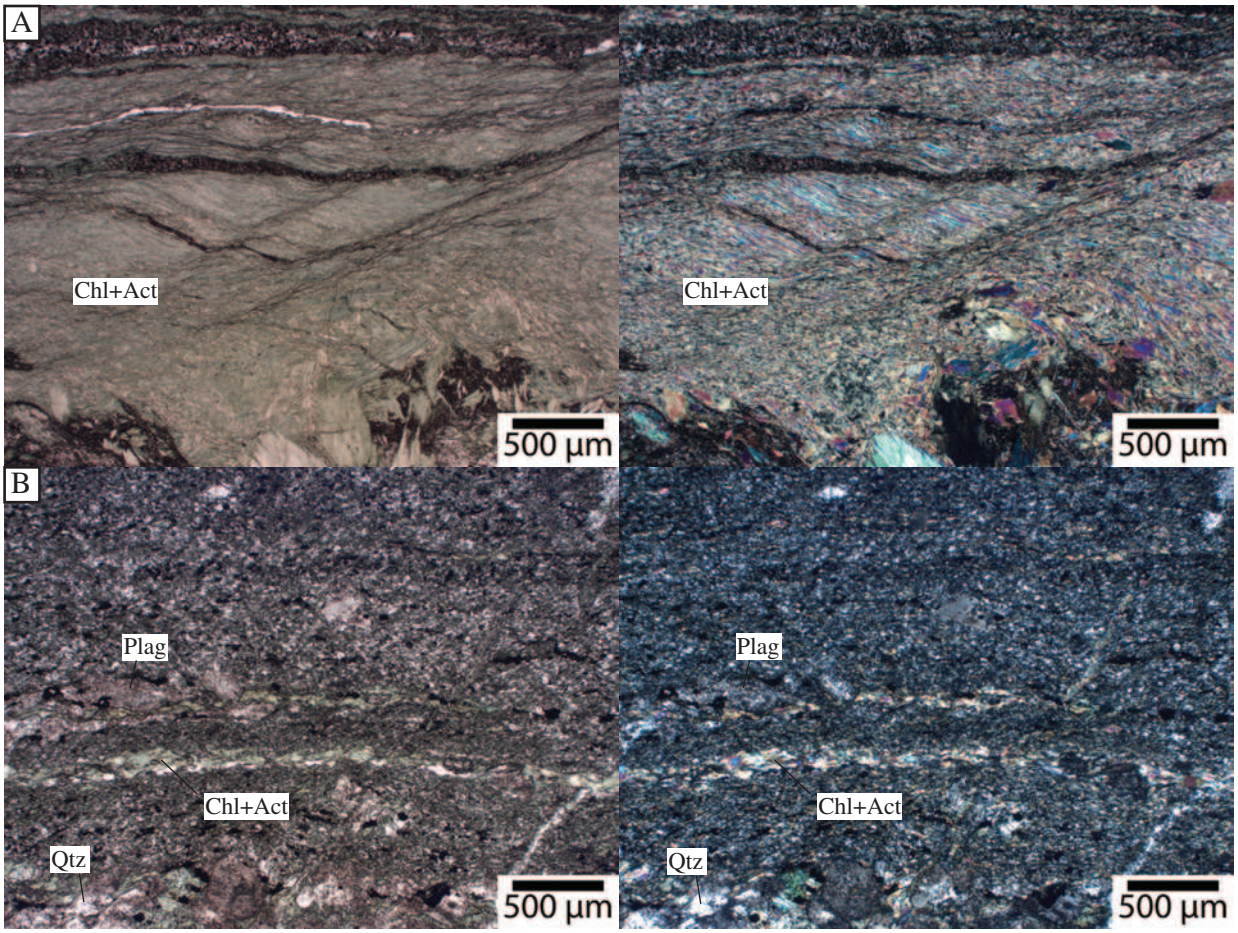


**Figure 33:** Plane-polarized (left) and cross-polarized (right) light photomicrographs with aligned fine-grained actinolite and chlorite defining the foliation. **A)** 17-1-P117b (mafic matrix sample, derived from a basaltic dike, within the hydrothermally-altered zone) and **B)** 16-1-P30a (mafic matrix sample, derived from a basaltic dike, within the hydrothermally-altered zone).

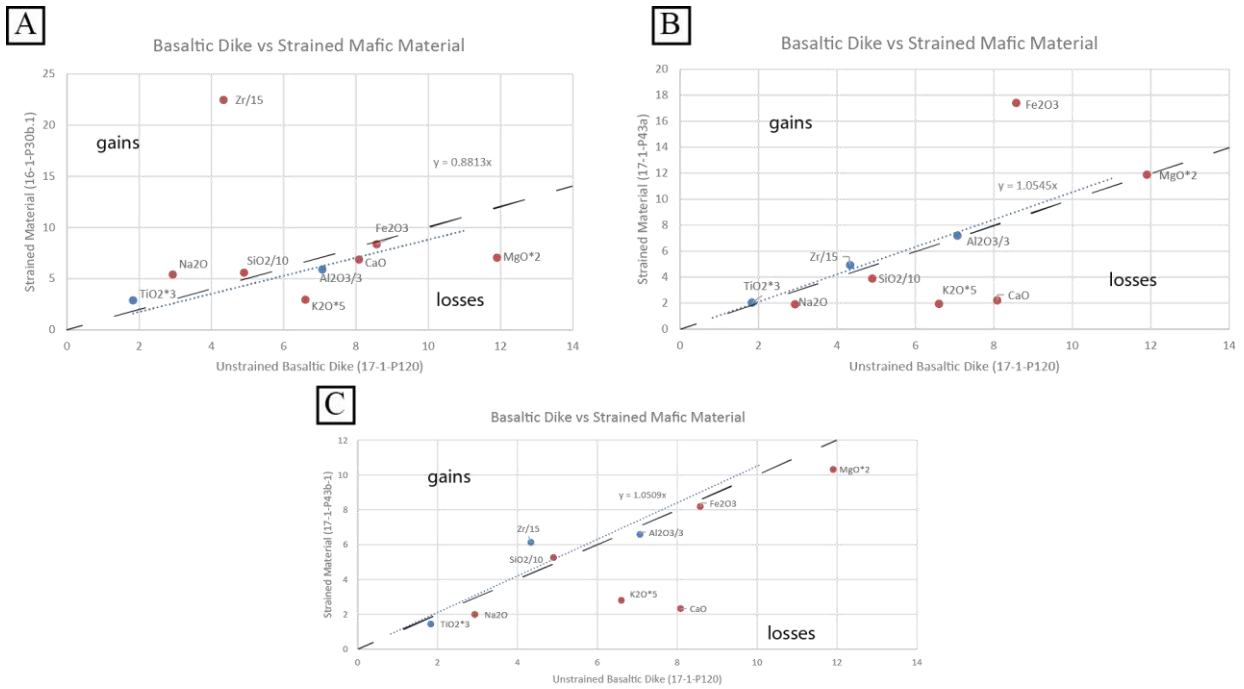


**Figure 34:** Isocon plots for deformed mafic matrix (hydrothermally-altered zone, 16-1-P30.1, 17-1-P43a, 17-1-P43b) vs undeformed basaltic dike (hydrothermally-altered zone, 17-1-P120) from shear zone A. **A)** 17-1-P120 vs 16-1-P30.1, **B)** 17-1-P120 vs 17-1-P43a, and **C)** 17-1-P120 vs 17-1-P43b-1. The values are scaled weight percents except for Zr which is a scaled ppm of Zr. The blue circles on each graph are immobile elements, and a best fit trend line of the immobile elements can be used to calculate the change in volume for each sample. Change in volume: **A)** 13%, **B)** -5%, and **C)** -5%. The red circles are mobile elements, which are relatively increased above the blue line and relatively decreased below. The black dashed line is a 1:1 line showing constant volume.

19 and 32). Based on this wide size distribution and angular shape we interpret this outcrop to record cataclasis and brittle mixing of the LJ-EK granodiorite and mafic dikes. The clasts are consistently flattened parallel to the foliation in adjacent mylonites and stretched parallel to the adjacent stretching lineation, and the black matrix is foliated with chlorite and fine-grained actinolite defining the foliation (Fig. 33). These observations suggest that brittle deformation and mixing of granodiorite with mafic dikes was followed by mylonitization of both the granodiorite clasts and mafic matrix. Strain data presented in chapter 1 suggest this outcrop and possibly shear zone A, in general, record a flattening strain (Fig. 20).

Dilational quartz-filled veins with fluid inclusions are also present in one of the samples from the unique outcrop described above (P43, Plate 1). The quartz in this veinlet displays

undulatory extinction and locally subgrains, suggesting that it formed during the late stages of plastic deformation (Fig. 35). The fluid inclusion assemblage we studied is pseudosecondary, steeply oriented, and slightly curviplanar (Fig. 36). The fluid inclusions are roughly ~2-4 µm, irregularly shaped, and have two phases with a fluid liquid proportion of ~0.9-0.95. The fluid inclusions were measured to determine the salinity and temperature of homogenization to help determine conditions of vein formation. From two-phase melting temperatures, we were able to determine the fluid is made up of 2.2% NaCl and 12.7% $CaCl_2$, which is consistent with the relative

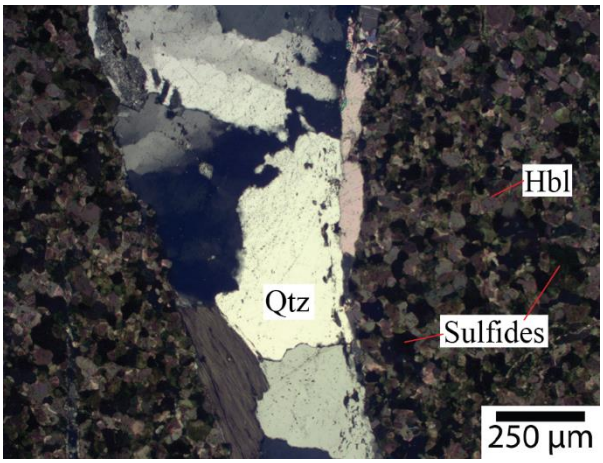


**Figure 35:** Cross-polarized light photomicrograph of the quartz veinlet in sample 17-1-P43a from the hydrothermally-altered zone. There are subgrains in the quartz and some grains have undulatory extinction. This suggests that these quartz veinlets formed near the end of plastic deformation and may record the conditions at the BPT. Fluid inclusion trails within these quartz veins were studied.

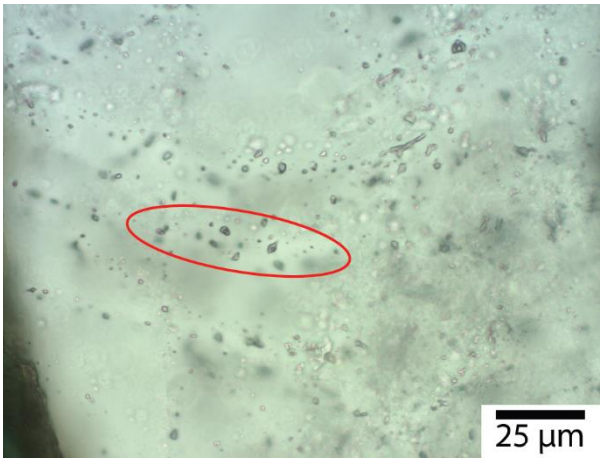


**Figure 36:** Photomicrograph of a portion of the pseudosecondary fluid inclusion trail studied in this paper.

increase of sodium and calcium observed in the geochemical data (Table 4). In order to determine rough temperature constraints for fluid inclusion formation we need to make an assumption about the pressure of formation. Al-in-hornblende geobarometry from plutons in surrounding parts of the Coastal Cordillera suggests Early Cretaceous plutons were emplaced at ~9 km depths (Gonzalez, 1996; Scheuber and Gonzalez, 1999; Kurth, 2000). Using 9 km as a lower limit and 6 km as an upper limit and assuming a fluid pressure gradient that ranges between hydrostatic and lithostatic, we estimate a pressure of formation for these fluid inclusions to be between 0.58 and 2.33 kbar. Using these pressure constraints and the isochores, we predict that the temperature of formation of these fluid inclusions and possibly the temperature at the BPT is 260-370°C (Fig. 37). This estimate can be more tightly constrained with more information on pressure gradient, pressure conditions at formation, and thermal gradient.

In several samples throughout shear zone A, using ImageJ, we measured the dynamically recrystallized quartz oblique grain shape fabric orientation, relative to the foliation, to evaluate the relative significance of simple shear vs. pure shear in shear zone A. The dominant orientation of long axes is 5-19° clockwise from the north end of the lineation (Figs. 16a-e), which is compatible with sinistral shear, but locally grain shape fabrics lack clear asymmetry. Assuming that grains rotate toward the shear zone plane during deformation, the maximum angle between the lineation (or the trace of foliation on the X:Z plane) and the grain long axes approximates the angle between the instantaneous stretching axis (ISA) and the finite strain X-direction (e.g. Dell'Angelo and Tullis, 1989; Wallis, 1995). This angle is a function of kinematic vorticity and can provide a

**Table 4:** Phase melting temperatures and homogenization temperatures of fluid inclusions from a fluid inclusion assemblage.

| Fluid Inclusion Assemblage #2 | 1 | 2 | 3 | 4 | 5 | 6 | Average |
|---|---|---|---|---|---|---|---|
| Initial Melt Temp (°C) | -56 | -56 | -55.5 | -60 | -52.7 | -55.9 | -56.0 |
| High Relief Phase 1 melt Temp (°C) | -29.7 | -30.3 | -30.8 | -30.9 | -30 | -30.8 | -30.4 |
| Ice melt Temp (°C) | -10.7 | -10.8 | -11.4 | -10.8 | -11.3 | -11 | -11.0 |
| Homogenization Temp (°C) | 235 | 223 | 233 | 223 | 237 | 224 | 229.2 |

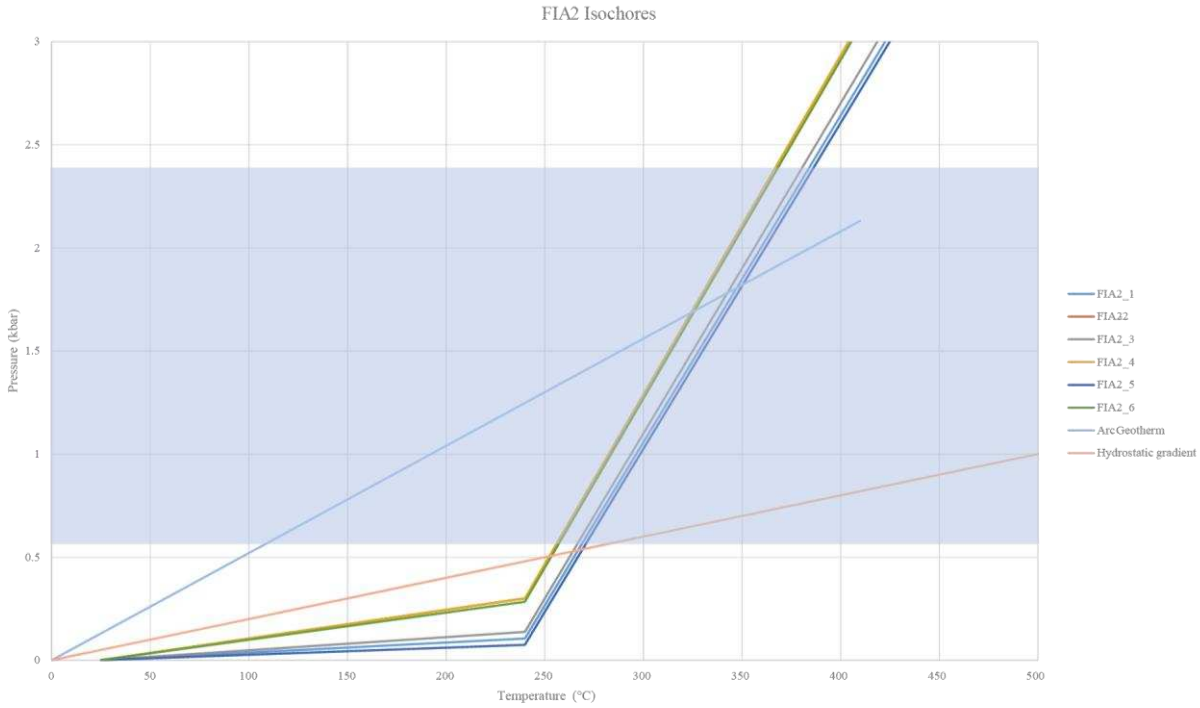


**Figure 37:** Results for a fluid inclusion trail in quartz from a dilational vein. The plotted medium blue, orange, grey, yellow, dark blue, and green lines are isochores for different fluid inclusions, the light blue line is an arc geothermal gradient (50 °C/km) at lithostatic pressure, and the orange line is an arc geothermal gradient (50 °C/km) at hydrostatic pressure. The blue region marks the pressure constraints from nearby barometry from pluton emplacement.

minimum constraint on the percent simple shear during deformation (Wallis, 1995). The average maximum angle of grain long axes is ~30°, providing a minimum of 67% simple shear.

In shear zone A, feldspar porphyroclasts are fractured, and regions of pure quartz are dynamically recrystallized. The dynamically recrystallized grains have a polygonal shape and are of similar size to subgrains within adjacent quartz, suggesting subgrain rotation was dominant (Fig. 14c and 38) (Hirth and Tullis, 1992; Stipp et al., 2002). We conducted electron backscatter diffraction (EBSD) analyses on four samples from shear zone A within quartz-rich regions to determine the recrystallized grain size and slip systems active in the dynamically recrystallized quartz. The c-axis pole figures for samples from the hydrothermally-altered zone have central point maxima, and a few have a slight girdle which would suggest a combination of mostly prism <a> slip, with some rhomb <a> and basal <a> slip, and the lack of asymmetry in the c-axes and a-axes

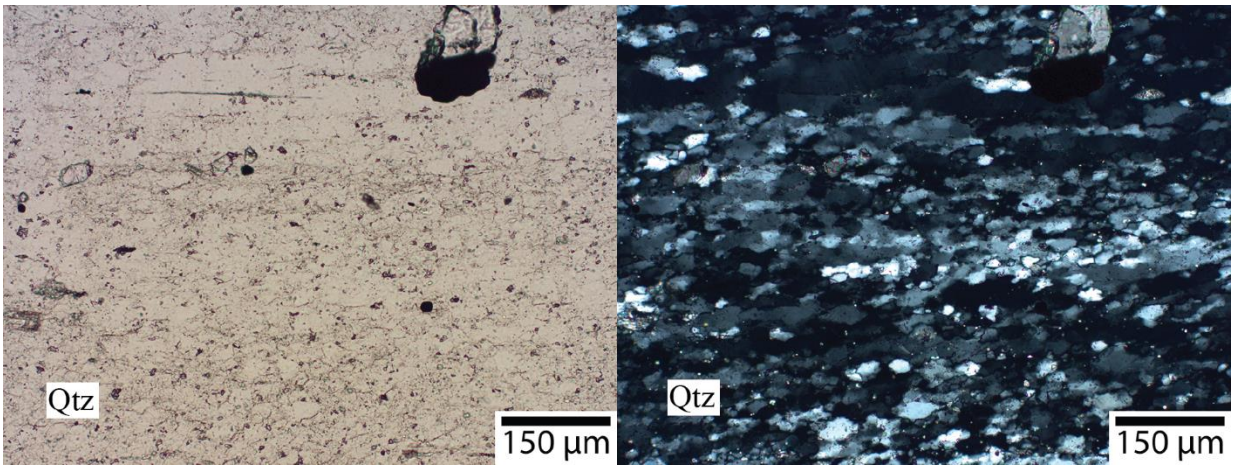


**Figure 38:** Plane-polarized (left) and cross-polarized (right) light photomicrographs of quartz dynamic recrystallization in the hydrothermal zone through subgrain rotation. Sample is 16-1-P23a from the hydrothermally-altered zone.

is consistent with coaxial-dominated deformation (Figs. 39a-d). The quartz in this zone primarily deformed through subgrain rotation dynamic recrystallization (Figs. 14c and 38). We measured recrystallized grain sizes of 5 samples manually using ImageJ (Appendix 5) rather than from misorientation maps because EBSD grain filtering would not eliminate all artifacts which resulted in underestimating the recrystallized grain size. The root mean square (RMS) from all 5 samples

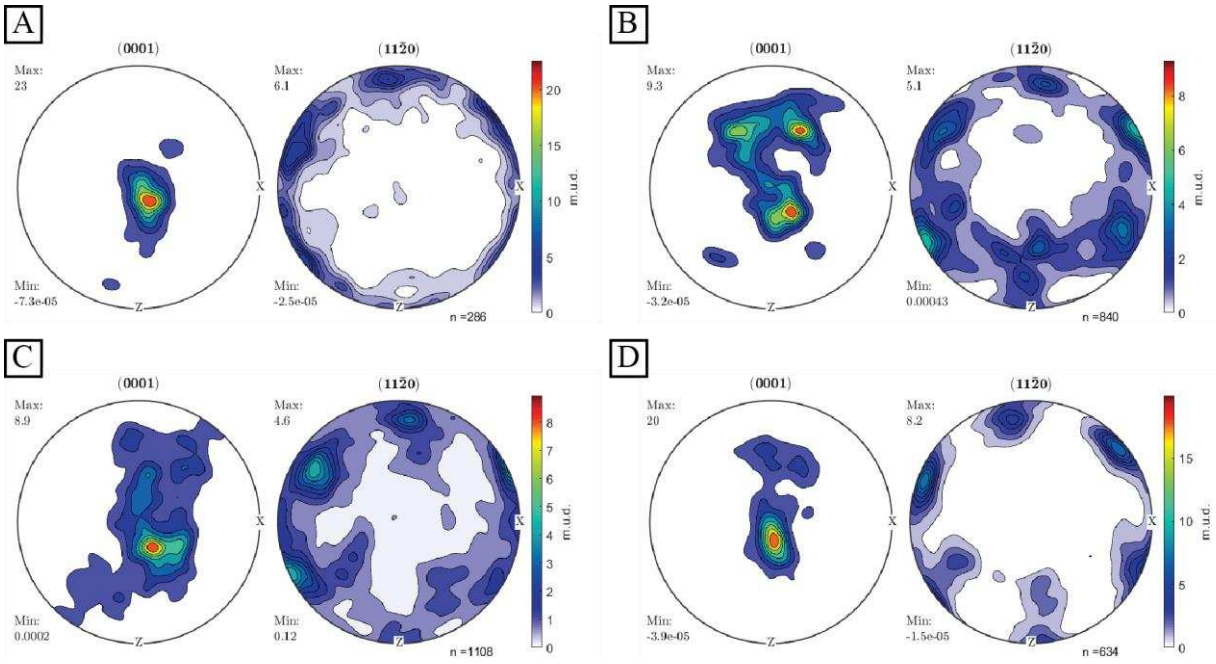


**Figure 39:** Pole figures for quartz from **A)** 16-1-P23a, **B)** 17-1-P9, **C)** 17-1P45, and **D)** 17-1-P95 within the hydrothermally-altered zone. All samples are from the Late Jurassic-Early Cretaceous granodiorite. The reference frame is looking down with north on the left.

of recrystallized grain diameters is ~25 µm, which corresponds to a differential stress of ~38 MPa using the Stipp and Tullis (2003) quartz recrystallized grain size piezometer with the calibration correction by Holyoke and Kronenberg (2010). However, most of these samples have a two-phase mixture of fine-grained feldspar and quartz as the dominant matrix phase, suggesting that a quartz piezometer may not be representative of the bulk rheology.

The two-phase mixture is commonly ~80% feldspar and ~20% quartz with minor amounts of white mica and chlorite along the grain boundaries of feldspar and quartz (Figs. 40a, b). We collected EBSD data on the two-phase mixture from sample 16-1-P30a (LJ-EK granodiorite) with many different feldspar species indexed. The two major feldspar phases the EBSD detected were

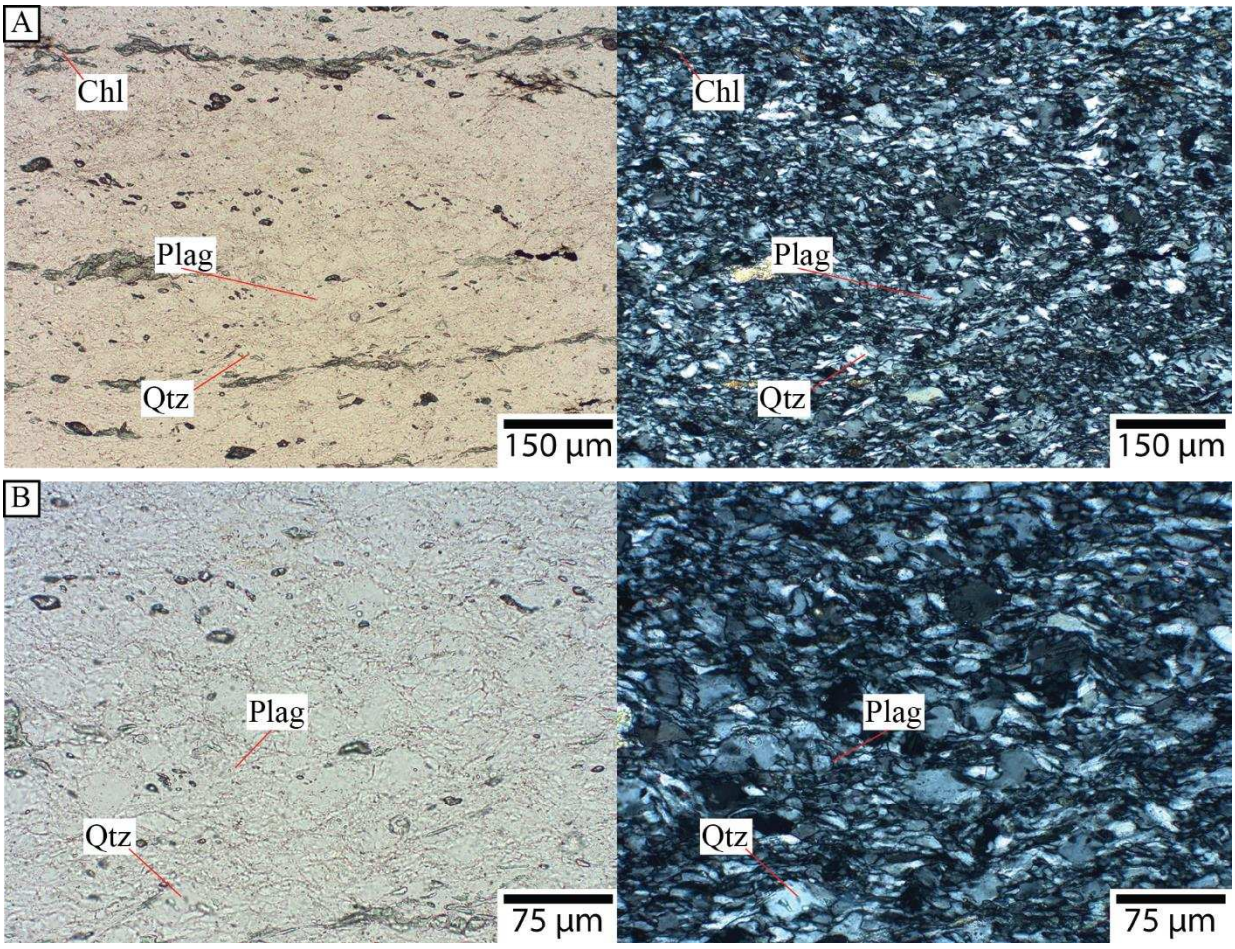


**Figure 40:** Plane-polarized (left) and cross-polarized (right) light photomicrographs of an example of the quartz-feldspar two-phase mixture **A)** lower magnification, **B)** higher magnification. Sample: 16-1-P30c (Late Jurassic-Early Cretaceous granodiorite)

anorthite and albite. The lack of a clear pattern in the feldspar pole figures, suggest there is no crystallographic preferred orientation (CPO) (Fig. 41a and b). The lack of CPO in feldspar, suggests that grain boundary sliding in these two-phase mixtures accommodates most of the strain in shear zone A rather than quartz dislocation creep (Rutter et al., 1994).

Given the two-phase mixture of fine-grained feldspar and quartz (with chlorite and white mica along grain boundaries) dominates the rheology of shear zone A, we cannot accurately make a rheological model for this shear zone yet. Platt (2015) created a flow law from experimental data for diffusion creep in fine-grained feldspar and water assisted thin film pressure solution creep in

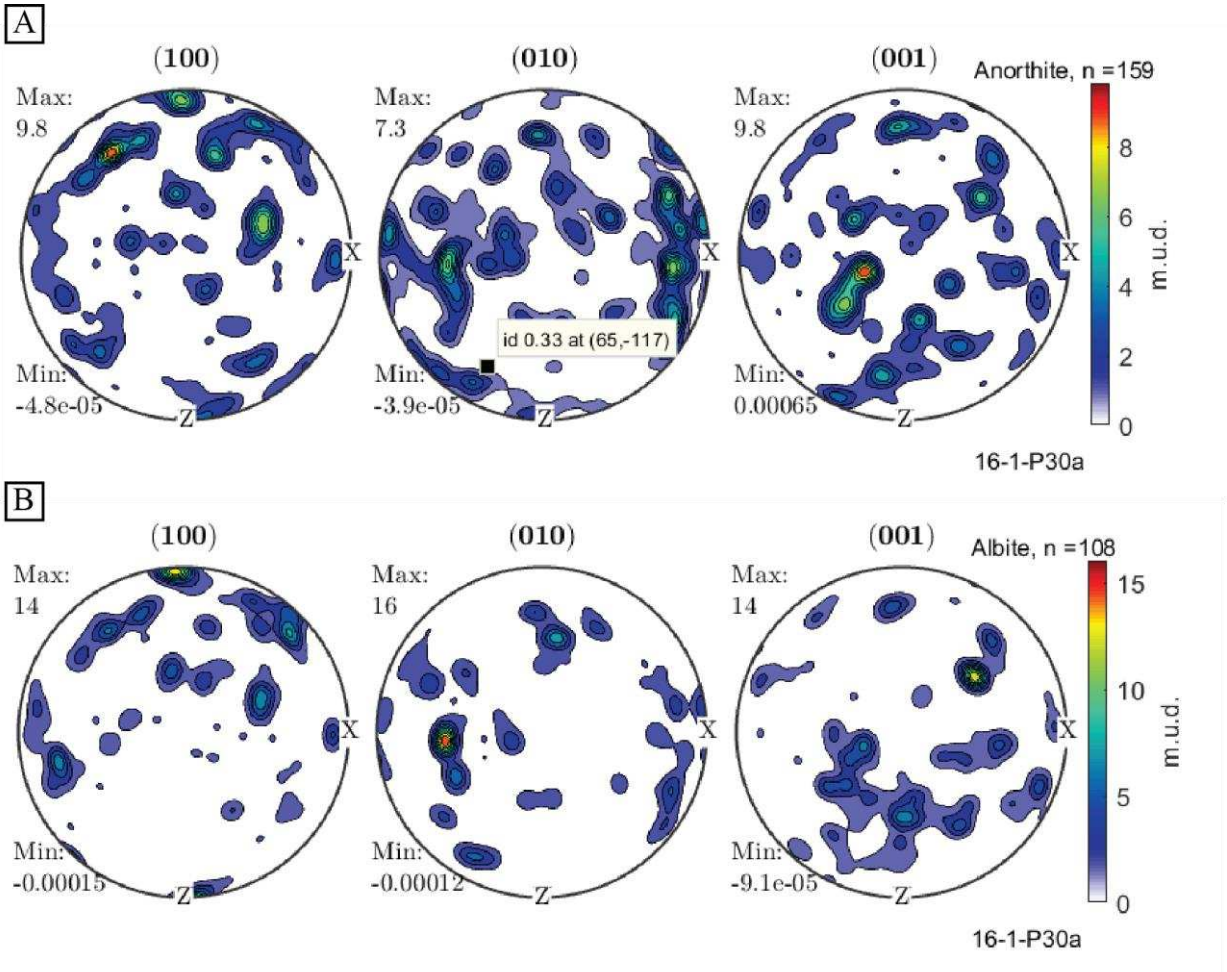


**Figure 41:** Pole figures from the two phase mixture in sample 16-1-P30a for **A)** anorthite and **B)** albite. The reference frame is the X:Z plane. Within this reference frame, the pole figures are looking down-dip with the north end of the lineation on the right.

quartz. However, it is unclear if these deformation mechanisms apply to the shear zone. In addition, the Platt (2015) flow law uses sodic plagioclase and does not account for the white mica and chlorite-coated grain boundaries, so it is not clear how applicable the flow law is to shear zone A.

## 2.5.Shear zone in Early Cretaceous tonalite (shear zone B)

### *2.5.1. Characteristics of shear zone B*

The Early Cretaceous tonalite is medium-grained (~1-3 mm), with ≤20% hornblende and ≤10% biotite or chloritized biotite and abundant late chlorite veinlets. This tonalite is mostly protomylonitic (Fig. 9e) with a few higher strain zones abutting the Paposo fault gouge zone. This unit has a U-Pb zircon age of 136.0 ± 1.6 Ma (Chapter 1, Appendix 1 and 2). The timing of mylonitization is bracketed by the age of the tonalite and a (U-Th)/He zircon cooling age of 116.6 ± 5.4 Ma in Late Jurassic granodiorite adjacent to the tonalite (Chapter 1, Fig. 8b). Shear zone B lacks pervasive hydrothermal alteration. The strained tonalite in thin section has better preserved feldspars, suggesting there is less hydrothermal alteration than in the hydrothermally-altered shear zone A. However, there is less mafic material in strained tonalite than unstrained tonalite suggesting some amount of hydrothermal alteration. Shear zone B within the Early Cretaceous tonalite lacks mafic dikes and pervasive hydrothermal alteration that characterize shear zone A.

### *2.5.2. Geochemical data*

To characterize the relatively minor hydrothermal alteration in shear zone B, we collected samples of unstrained protolith, protomylonite, and ultramylonite. Geochemistry from both the protomylonite-protolith pair and the ultramylonite-protolith pair suggests a relative gain of $SiO_2$ and $K_2O$, a relative loss in MgO, $Fe_2O_3$, and CaO, and little change in $Na_2O$ (Fig. 42a and b) in the deformed rocks. Percent volume change was calculated from the best fit trend line through the

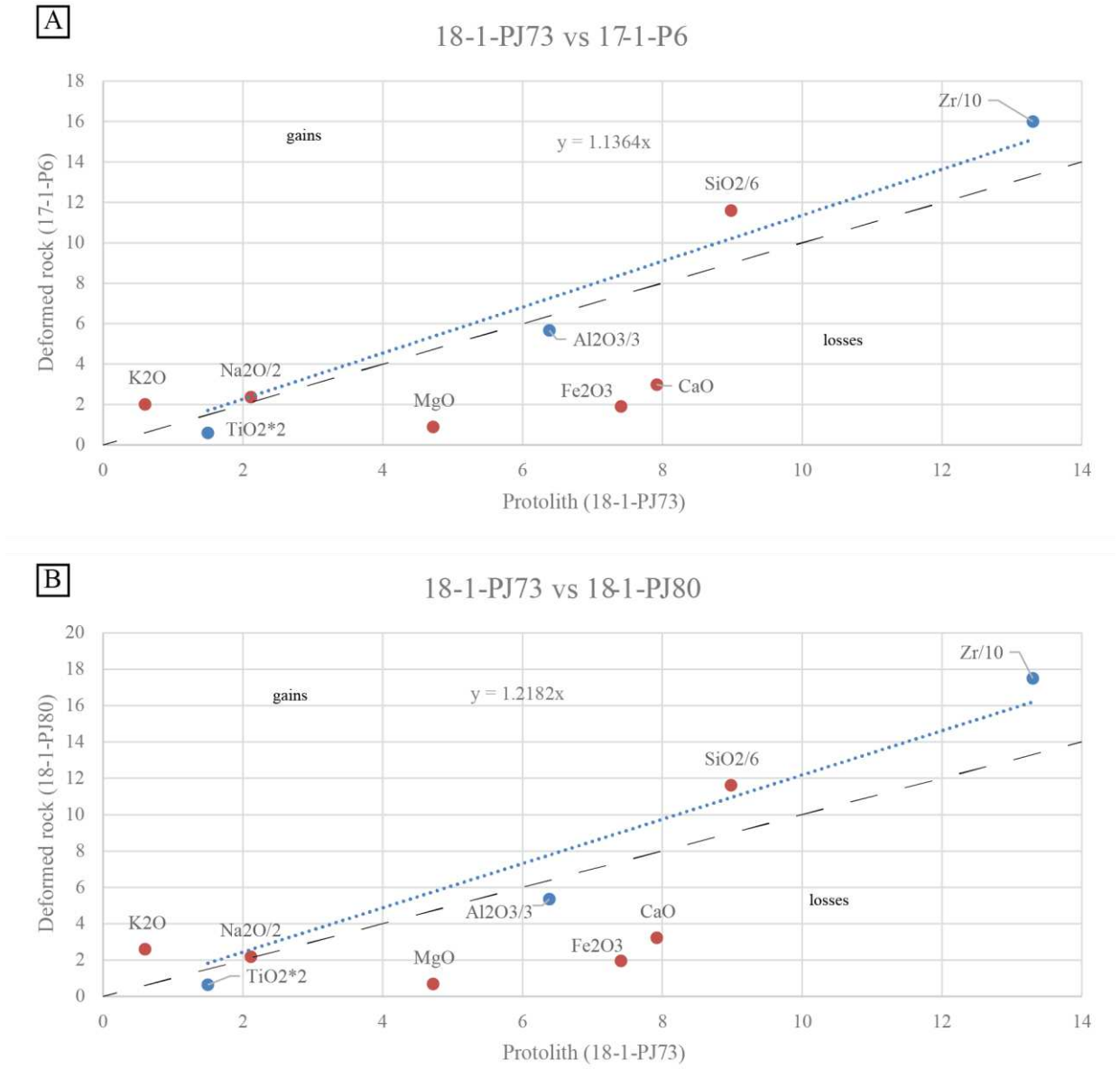


**Figure 42:** Isocon plots for deformed tonalite (17-1-P6, 18-1-PJ80) vs undeformed tonalite (19-1-PJ73). **A)** 18-1-PJ73 vs17-1-P6 (protomylonite) and **B)** 18-1-PJ73 vs 18-1-PJ80 (ultramylonite). The values are scaled weight percents except for Zr which is a scaled ppm of Zr. The blue circles on each graph are immobile elements, and a best fit trend line (dotted blue line) of the immobile elements can be used to calculate the change in volume for each sample. Change in volume: **A)** -12% and **B)** -18%. The red circles are mobile elements, which are relatively increased above the blue line and relatively decreased below. The black dashed line is a 1:1 line showing constant volume.

assumed immobile elements (Zr, $Ti_2O$, and $Al_2O_3$). Compared to shear zone A, inferred volume loss is relatively minor: ~12% in the protomylonite and ~18% in the ultramylonite (Fig. 42a and b). This shear zones alteration is characterized by a relatively small increase in $SiO_2$ and $K_2O$, and a relatively large decrease in MgO, CaO, and $Fe_2O_3$.

### *2.5.3. Microstructures, kinematics, and rheological controls on deformation*

Foliations and lineations in this unit are not well developed due to overall low strain, and are locally difficult to measure due to pervasive fracturing and poor exposure. The average foliation and lineation in shear zone B is 051/69 SE and 31/219, respectively (Fig. 43), and there is a slight relationship between distance from the gouge zone and strike of the foliations suggesting foliation may have rotated towards parallelism with the Paposo fault (Fig. 15). Protomylonitic fabrics grade into mylonite and locally ultramylonitic fabrics within a few meters of the gouge zone. These relationships suggest the shear zone is kinematically related to the brittle Paposo fault zone. In thin section the protomylonite samples record sinistral-reverse shear indicators such as oblique grain shape fabrics (Fig. 44). None of the samples have symmetric microstructures, but some samples have variable foliations which wrap around porphyroclasts and make shear sense difficult to determine. Elongate quartz zones extend across the thin section and form the dominant

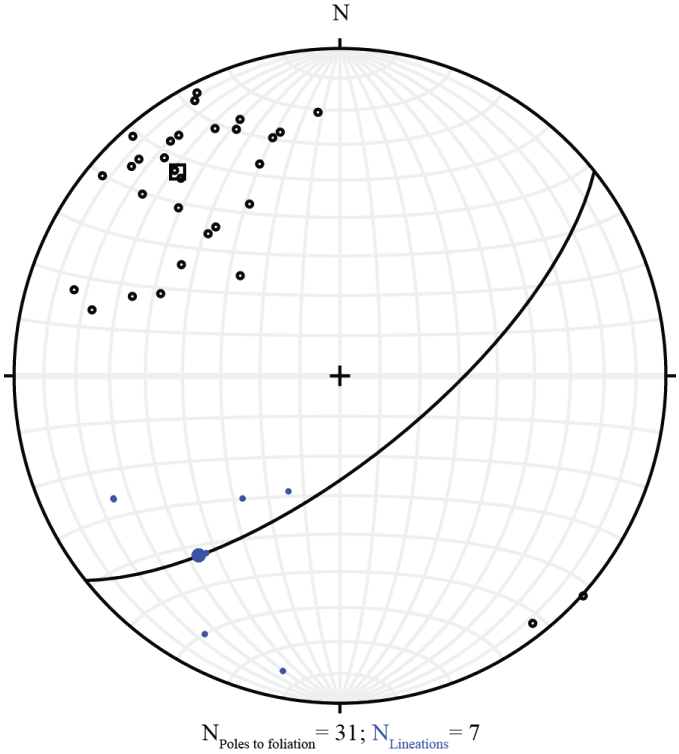


**Figure 43:** Stereoplot of poles to foliation (hollow black circles) and lineations (blue circles) from shear zone B with the average pole to foliation (large hollow square), average lineation (large blue circle) and average foliation plane (black arc).

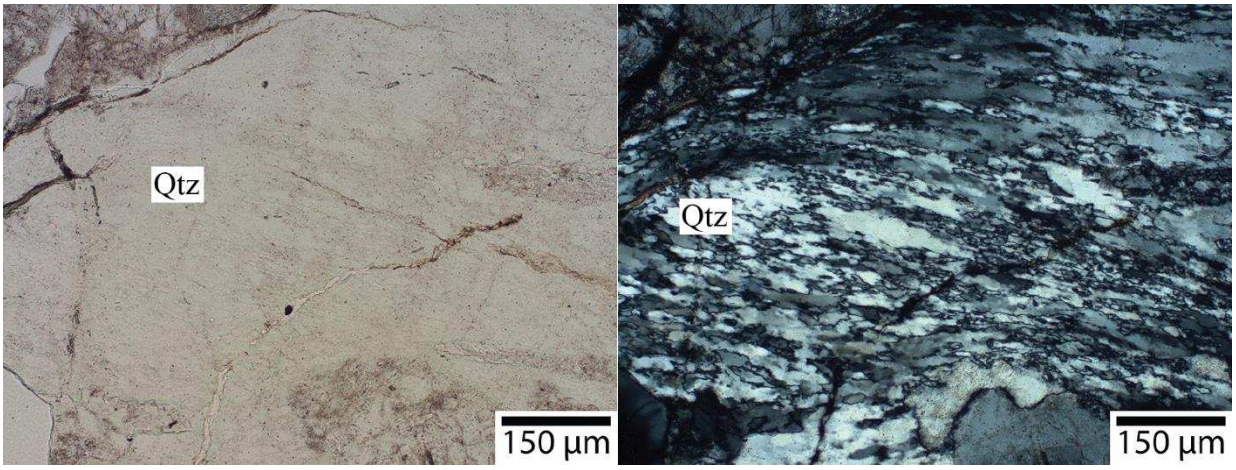


**Figure 44:** Photomicrograph of a plane-polarized light image and cross-polarized light image of dynamically recrystallized quartz oblique grain shape fabric from shear zone B (sample: 17-1-P50 from Early Cretaceous tonalite). This is photomicrograph shows evidence for bulge nucleation recrystallization and some evidence for subgrain rotation. Bulge nucleation recrystallization is the dominant deformation mechanism with some subgrain rotation.

through-going weak phase in shear zone B, with a sinistral shear sense indicated by an oblique recrystallized grain shape fabric (Fig. 44). Feldspars deform brittlely through fracturing, and about 20-50% of the quartz is dynamically recrystallized. The majority of dynamically recrystallized grains are along grain boundaries of relatively undeformed quartz which suggests bulge nucleation is dominant (Fig. 44). However, some quartz grains have subgrains and some dynamically recrystallized quartz is polygonal, suggesting there is some subgrain recrystallization (Fig. 44). In outcrops near the gouge zone there are also foliation parallel cataclasites (~1 cm) and near the gouge zone recrystallized quartz zones are fractured (Figs. 45a and b).

We determined the mean dynamically recrystallized quartz grain size and grain shape fabric orientation on 5 samples from shear zone B (Appendix 5). The mode angles of quartz long axes are 15-23° clockwise from the north end of the lineation, which is compatible with sinistral shear (Figs. 17a-e). The average maximum angle of grain elongation angle is ~36° from the north end of the lineation and gives a minimum constraint of 80% simple shear for shear zone B. The percent of simple shear and relatively high oblique grain shape fabric suggests that this shear zone accommodated transpression through non-coaxial-dominated sinistral-reverse shear.

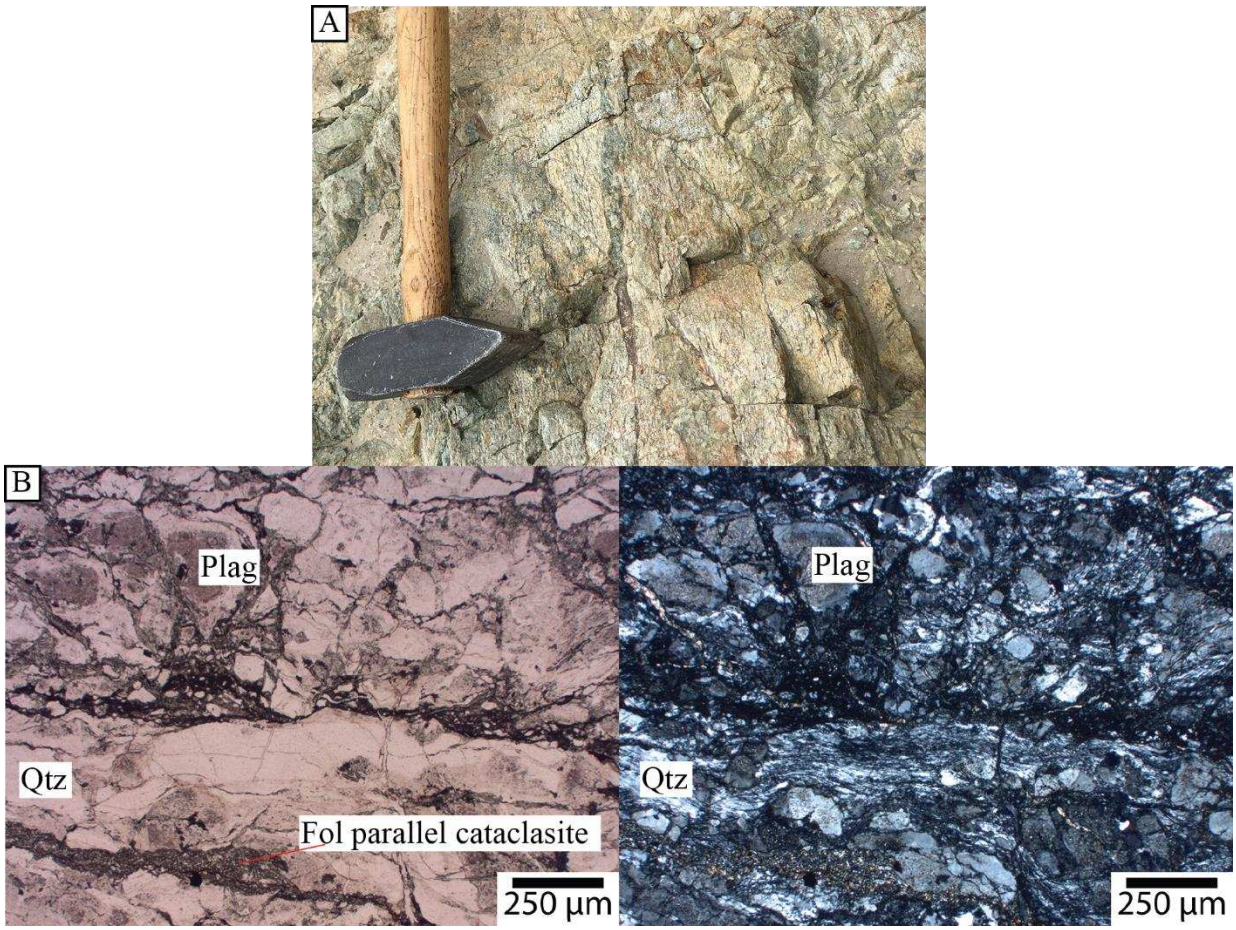


**Figure 45: A)** An outcrop photo of the foliation- parallel cataclasite within the Early Cretaceous tonalite. **B)** Plane-polarized (left) and cross-polarized (right) light photomicrographs of a foliation parallel cataclasite in sample 17-1-P6 from the Early Cretaceous tonalite.

We conducted electron backscatter diffraction (EBSD) analyses on samples with quartz-rich regions to determine active slip systems of quartz and the average dynamically recrystallized grain sizes. When cutting billets for EBSD analyses, we did our best to determine and cut parallel to the X:Z plane. However, lineations are very poorly developed in the protomylonite, so billets were cut parallel to the average lineation from the deformed EK tonalite. Pole figures appear to be slightly misaligned with typical X:Z plan symmetry patterns, so the data were rotated by 15 degrees in MTEX, a Matlab program for analyzing EBSD data, to partially correct this misalignment (Fig. 46a, b, c, and d). The foliation in the Y direction may also be locally misaligned for sample 17-1-P50 due to wrapping of foliation around porphyroclasts, but we have not corrected for this because

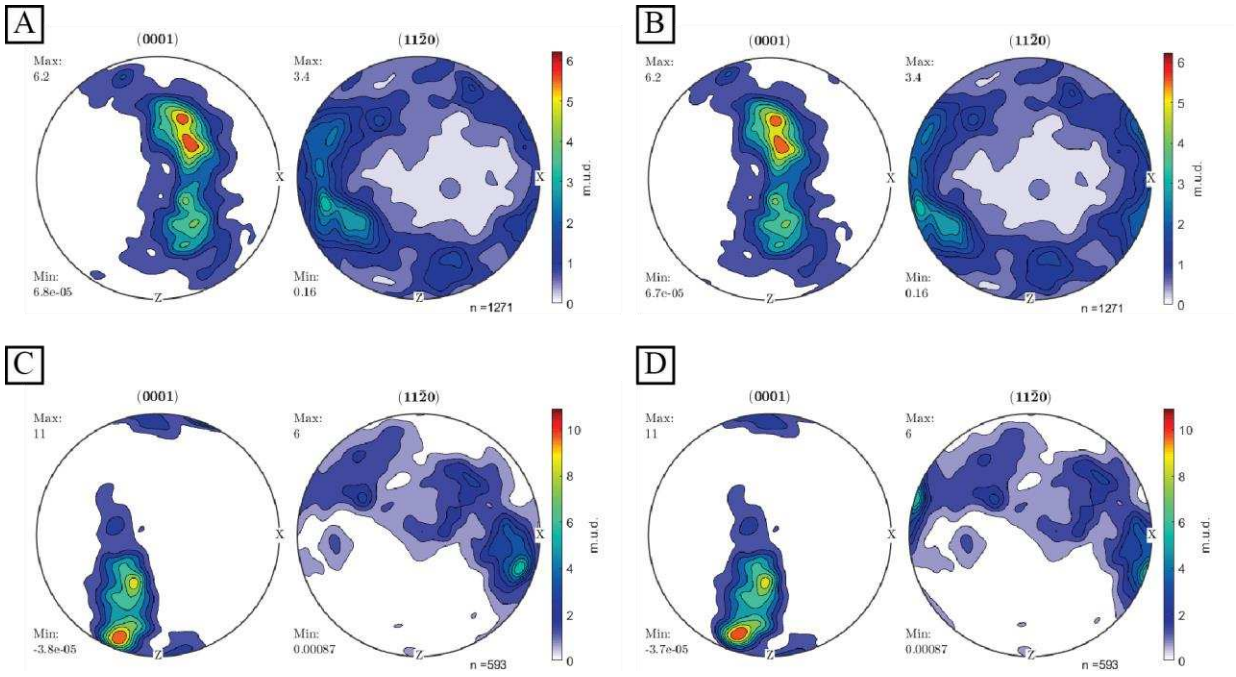


**Figure 46:** Pole figures for quartz from **A)** and **B)** 17-1-P6 and **C)** and **D)** 17-1P50. The raw pole figures for the respective samples are on the left and the slightly rotated pole figures are on the right. The protomylonite does not have good lineations so the X:Z plane was cut parallel to a kinematically averaged lineation of nearby measurements. This was slightly off so the pole figure for 17-1-P6 has been rotated by 15 degrees in the X-vector about Z and the pole figure for 17-1-P50 has been rotated by -15 degrees in the X-vector about Z.

the sample was cut perpendicular to the overall foliation. The c-axis pole figures from samples 17-1-P6 and 17-1-P50 have girdles, which suggest that the active slip systems in quartz are primarily basal <a> and rhomb <a> slip. Overall the c-axes and a-axes are slightly asymmetric and suggest sinistral non-coaxial shear (Fig. 46b and d). These active slip systems suggest deformation at relatively low temperatures (Passchier and Trouw, 2005). The abundance of quartz recrystallization and presence of a CPO in quartz, suggests that the main quartz deformation mechanism is dislocation creep.

We measured the recrystallized grain size and the oblique grain shape fabric for five samples using ImageJ and found that the quartz has on average been dynamically recrystallized to ~10 µm which corresponds to a differential stress of ~78 MPa using the Stipp and Tullis (2003) quartz recrystallized grain size piezometer with the calibration correction by Holyoke and

Kronenberg (2010). The sample that contains foliation-parallel cataclasite zones (Fig. 45a and b) has the smallest recrystallized grain size (~6 μm), indicating differential stress was ~117 MPa. These small recrystallized grain sizes and presence of foliation-parallel cataclasite (Fig. 45a and b), suggest these rocks deformed near the BPT, where the peak strength of the crust resides.

We constructed a rheological model for shear zone B matching the BPT strength based on typical strain rates and coefficients of friction with the estimated BPT strength from piezometry. The model was constructed using brittle curves defined by frictional slip of a strike-slip fault regime with coefficients of friction of $\mu = 0.85$ (Byerlee, 1978), 0.6, and 0.4 and a stress ratio ($\Phi$) of 0.4. The stress ratio is the difference between $\sigma_2$ and $\sigma_1$ divided by the difference between $\sigma_3$ and $\sigma_1$. The stress ratio denotes how close the stress field is from pure uniaxial tension (transpression; $\Phi<0.5$) or from pure uniaxial tension (transtension; $\Phi>0.5$). Since there is evidence this shear zone is slightly transpressional we use a $\Phi$ of 0.4. Strain rate curves for $\dot{e} = 10^{-15}$, $\dot{e} = 10^{-14}$, $\dot{e} = 10^{-13}$, and $\dot{e} = 10^{-12}$, were constructed with a water fugacity of 11.7, assuming hydrostatic fluid pressure at 400 °C, an assumed geothermal gradient of 50 °C/km (Scheuber and Ruetter, 1992), using the quartzite flow law from Hirth et al. (2001), and the stress of shear zone B was estimated using the quartz piezometer from Stipp and Tullis (2003) with the calibration correction from Holyoke and Kronenberg (2010) from the sample with the smallest average recrystallized grain size (Fig. 47). Our estimate of the peak strength of the crust matches the modelled strength profile with a strain rate between $10^{-13}$ and $10^{-14}$, hydrostatic fluid pressure, a coefficient of friction of 0.85, and a shallow BPT (~6 km).

### 2.6.Gouge Zone

The gouge zone consists primarily of foliated illite with brittlely-fractured EJ granodiorite clasts derived from the west side of the fault. S-C-C' fabrics in the gouge suggest sinistral slip

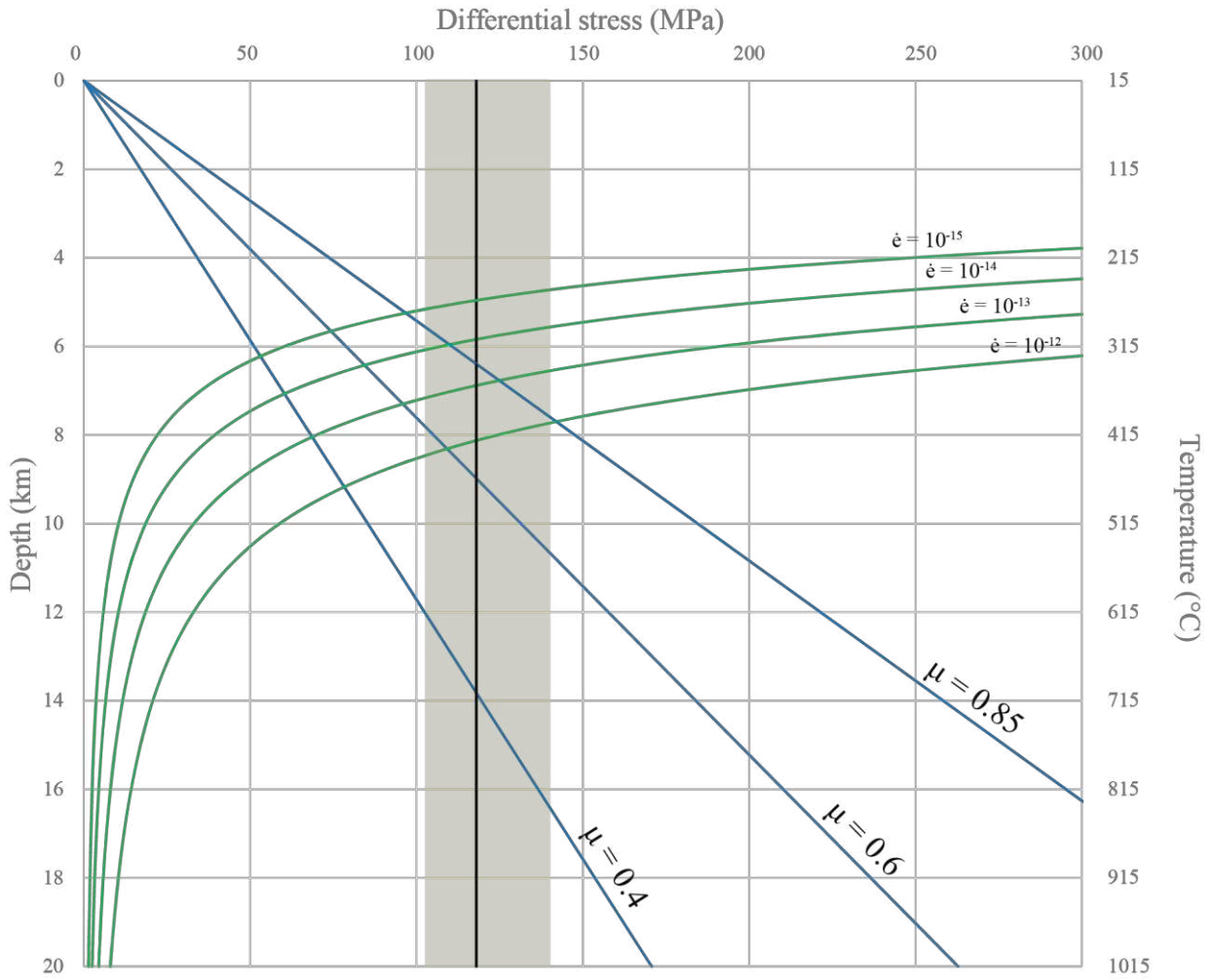


**Figure 47:** Rheological model of shear zone B. The vertical bold black line is a stress estimate from quartz piezometry with a one standard deviation error bar (transparent yellow region). The blue lines are strength profiles for hydrostatic fluid pressure with coefficients of friction of 0.85, 0.6, and 0.4. The green arcs are quartz flow laws calculated using a geothermal gradient of 50ºC/km and strain rates of 10-12, 10-13, 10-14, and 10-15. This rheological model was made using the quartz piezometer from Stipp and Tullis (2003) with the calibration correction from Holyoke and Kronenberg (2010) and the quartzite flow law from Hirth et al. (2001).

(Fig. 23). The average gouge foliation orientation is 027/82 E which is ~10° clockwise of the Paposo fault trend and also consistent with sinistral slip (Fig. 24). Slickenlines are not well developed in this zone but the few slickenlines measured have a moderate to shallow plunge suggesting a component of reverse slip. This zone is made up of quartz, albite, illite, chlorite, calcite, and hematite. Qualitatively, illite makes up a large proportion of this mineralogy, and illite

has a coefficient of friction of ~0.4 (Morrow et al., 1992). The frictional strength of illite likely dominated the strength of this zone.

## 2.7.Discussion

We have found evidence for two brittle-plastic transitions, one within the Late Jurassic-Early Cretaceous granodiorite and the other in the Early Cretaceous tonalite. Shear zone A, in the Late Jurassic-Early Cretaceous granodiorite is characterized by intense hydrothermal alteration, synkinematic mafic dike emplacement, quartz fabrics with a significant orthorhombic symmetry, and a matrix dominated by a two-phase mixture of fine-grained feldspar and quartz. Shear zone B in the Early Cretaceous tonalite lacks mafic dikes and intense hydrothermally alteration, has quartz as the through-going weak phase, and has more asymmetric quartz fabrics compared to shear zone A. The geochemical data from the shear zones suggest alteration was different. The rocks in shear zone A show an increase in Si, Ca, and Na, whereas the rocks in shear zone B are enriched in Si and Na. Both shear zones exhibit sinistral-reverse shear along a steeply SE-dipping zone, with evidence of more coaxial strain along shear zone A and a larger reverse, non-coaxial component along shear zone B.

In shear zone A, the most pervasive strain is localized within the hydrothermally-altered zone. In this zone, dynamically recrystallized quartz grain size is relatively large, even at locations where mixing between granodiorite and mafic dikes record conditions at the brittle-plastic transition. High strain zones within the <50% and >50% mylonite units are spatially associated with hydrothermal alteration, and within the hydrothermal alteration zone where outcrops are heterogeneously altered, more altered areas are also higher strained. All of these observations suggest that the hydrothermally-altered zone is rheologically weak.

In shear zone A we observe, symmetric oblique grain shape fabrics and symmetric and low asymmetry porphyroclasts. In shear zone B we observe higher angle more asymmetric oblique grain shape fabrics and asymmetric porphyroclasts. We also found the average maximum angle of grain elongation for shear zone A, ~30º, and for shear zone B, ~36º (Fig. 16 and 17). From these oblique grain shape fabrics, we are able to determine a minimum percent simple shear for the shear zones. The minimum estimate for percent simple shear of shear zone A is ~67% and ~80% for shear zone B. The lower angle of oblique grain shape fabrics and symmetric fabrics in shear zone A suggest that strain was accommodated via sinistral transpression with a coaxial pure shear component. The higher angle of oblique grain shape fabrics and asymmetric microstructures in shear zone B suggest that it accommodated transpression via sinistral-reverse shear with larger component of simple shear. However, strain in both is compatible with overall sinistral transpression along the Paposo fault.

Because of the difference in through-going phases the two shear zones have different rheologies. Platt (2015) discusses which through-going phase dominates the bulk rheology. When stress is relatively low and the grain size of the two-phase mixture is small, diffusion creep of the two-phase mixture will dominate (Platt, 2015). These feldspar-quartz mixtures deform at higher strain rates than pure quartz or pure feldspar with the same stresses and grain size, which suggests that these two-phase mixtures are weaker than their single-phase counterparts. The difference in recrystallized quartz grain size between these two shear zones could suggest that the recrystallized quartz grain size is recording lower stresses in shear zone A because the strength of this zone is controlled by the weaker two-phase mixture of quartz and feldspar.

The average recrystallized quartz grain sizes from the samples with the smallest dynamically recrystallized grain sizes for the shear zones are ~20 µm (shear zone A) and ~6 µm

(shear zone B). The average recrystallized grain size for all samples from shear zone A and shear zone B are ~25 µm and ~10 µm, respectively. These average grain sizes are relatively consistent across each shear zone (Fig. 48). Since the dominant through-going phases in shear zone A are regions of two-phase mixtures and not regions of pure quartz, we believe that quartz piezometry underestimates the strength of the crust in shear zone A. Hydrothermal alteration resulting in this two-phase mixture of fine-grained feldspar and quartz with chlorite- and white mica-coated grain boundaries, most likely significantly lowered the strength of granodiorite in shear zone A (e.g. Oliot et al., 2010; Goncalves et al., 2012). While the two-phase mixtures' strength may be uncertain, it is definitely weaker than the rigid feldspar porphyroclasts that are common in shear zone B.

The smallest average recrystallized grain size from the two shear zones is comparable to the smallest recrystallized grain sizes from brittle-plastic shear zones studies by Singleton et al. (2018) (normal fault), Behr and Platt (2011, 2013) (normal fault), and Kidder et al. (2012) (thrust fault regime) and slightly smaller than grain sizes from Gottardi and Teyssier (2013) (normal fault regime) and Kidder et al. (2014) (strike-slip, Alpine fault). This similarity suggests that they the peak strength of faults from these different tectonics settings were also relatively similar. When making a rheological model for shear zone B, we assume typical coefficients of friction ($\mu$=0.4, 0.6, and 0.85) and strain rates ($10^{-13}$and $10^{-14}$) and estimate the peak strength of shear zone B to be ~6 km depth with a 50 °C/km geothermal gradient. If we consider the same conditions for this shear zone but use a more typical geothermal gradient of 25 °C/km (possible conditions outside of the magmatic arc), the BPT has a depth of ~11 km and an estimated shear stress ~1.8 times higher than the stress we calculate through quartz piezometry (Fig. 49). This strength profile models suggests that the high geothermal gradients resulted in a weak crust. The observation that ductile

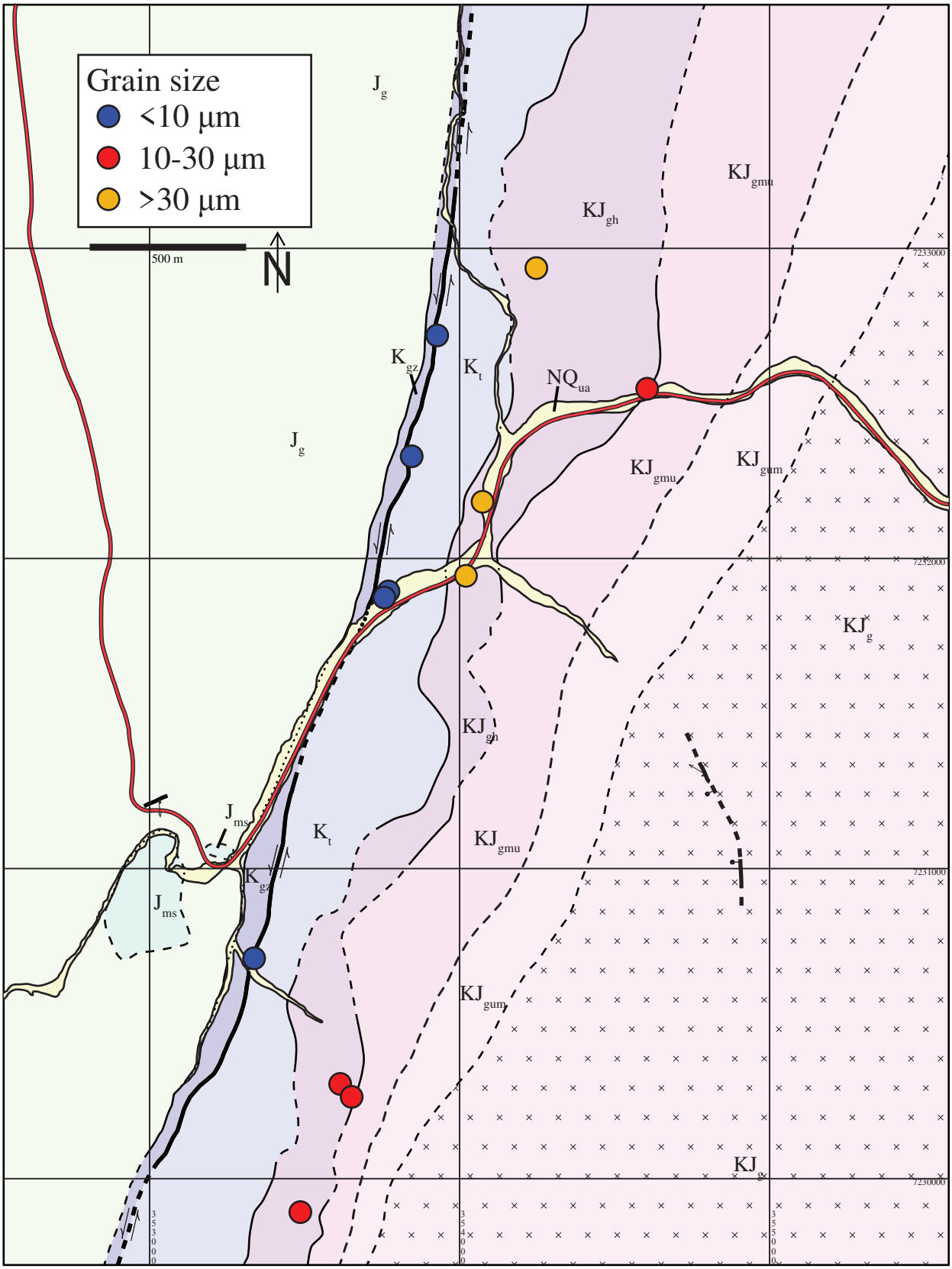


**Figure 48:** Distribution of measured recrystallized quartz grain sizes.

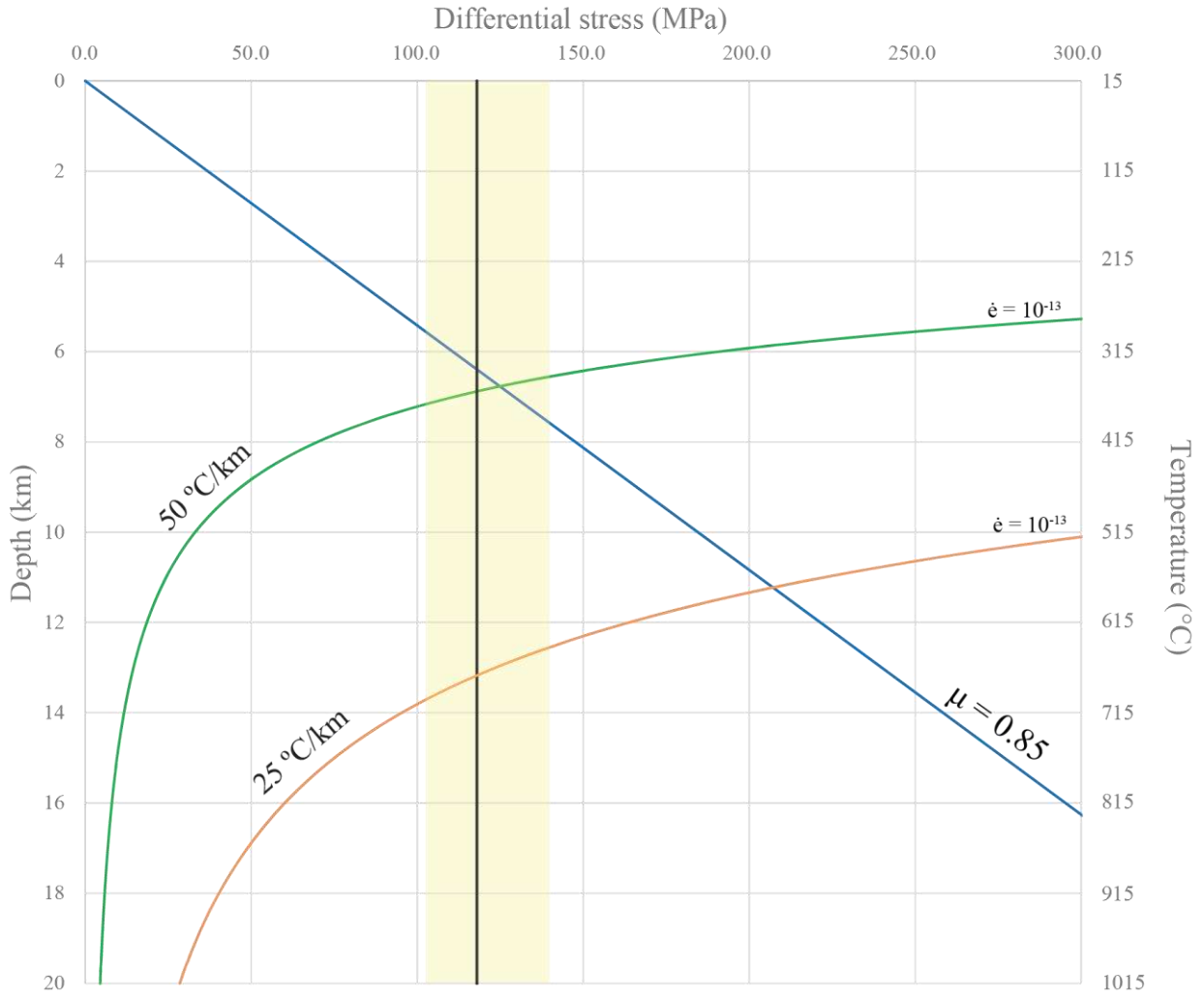


**Figure 49:** Rheological model of shear zone B. The vertical bold black line is a stress estimate from quartz piezometry with a one standard deviation error bar (transparent yellow region). The blue line is a strength profile for hydrostatic fluid pressure with a coefficient of friction of 0.85. The green arc is a strain rate curve of 10-13 calculated using a geothermal gradient of 50 ºC/km, and the orange arc is a strain rate curve of 10-13 calculated using a geothermal gradient of 25 ºC/km. This rheological model was made using the quartz piezometer from Stipp and Tullis (2003) with the calibration correction from Holyoke and Kronenberg (2010) and the quartzite flow law from Hirth et al. (2001).

shear zones are found within synkinematic plutons also suggests that shear zones are in fact being localized within hot, fluid-rich, rheologically weak plutons. These shear zones are weaker than a typical mid-crust. Shear zone A is weaker because of hydrothermal alteration resulted in reaction weakening, and deformation was coeval with magmatism in a high geothermal gradient resulting in a shallow BPT. Shear zone B is also weak because deformation was coeval with magmatism, and the high geothermal gradient resulted in a shallow BPT. In addition, the frictionally weak

gouge zone appears to be kinematically related to the tonalite shear zone, suggesting that the Paposo fault continued to be a relatively weak structure in the brittle regime.

## 2.8.Conclusions

The older shear zone A is characterized by deformation associated with hydrothermal alteration and dike emplacement, a weak two-phase mixture of quartz and altered feldspar, and quartz fabrics with high degrees of symmetry. The younger shear zone B is characterized by lack of pervasive hydrothermal alteration, quartz as the through-going weak phase, and more asymmetric fabrics. The rheological model of shear zone B suggests that intra-arc strike-slip fault systems are weak and become localized in hot, fluid rich plutons due to thermal weakening and reaction softening. The depth predicted for the BPT is much shallower than other systems due to this high geothermal gradient. Magmatism and hydrothermal alteration of shear zone A fundamentally changed the rheology of the shear zone to be weaker and more deformable.

## REFERENCES


Abad, I. 2007. Physical meaning and applications of the illite Kübler index: Measuring reaction progress in low-grade metamorphism, in Diagenesis and Low-Temperature Metamorphism, Theory, Methods and Regional Aspects, Seminarios, F. Nieto and J. J. Millán (Editors), Sociedad Espanola Mineralogia, Jaén, Spain, 3, 53–64.

Allmendinger, R.W., Cardozo, N., Fisher, D., 2012. Structural Geology Algorithms: Vectors and Tensors in Structural Geology. Cambridge University Press.

Alvarez, J.A., Jorquera, R.B., Miralles, C.G., Padel, M., and Martinez, P.E. 2016. Cartas Punta Posallaves y Sierra Vicuna Mackenna. Sernageomin, scale: 100,000.

Arancibia G., Fujita, K., Kenichi, H., Mitchell, T.M., Cembrano, J., Gomila, R., Morata, D., Faulkner, D.R., and Rempe, M. 2014. Hydrothermal alteration in an exhumed crustal fault zone: Testing geochemical mobility in the Caleta Coloso Fault, Atacama Fault System, Northern Chile. Tectonophysics, 623, 147-168.

Avė Lallemant, H.G., Schmidt, W.J., Kraft, J.L. 1985. Major Late-Triassic strike-slip displacement in the Seven Devils terrane, Oregon and Idaho: A result of left-oblique plate convergence. Tectonophysics, 119, 299-328.

Behr, W.M. and Platt, J.P. 2011. A naturally constrained stress profile through the middle crust in an extensional terrane. Earth and Planetary Science Letters. vol. 303. p. 181-192.

Behr, W.M. and Platt, J.P. 2013. Rheological evolution of a Mediterranean subduction complex. Journal of Structural Geology, 54, 136-155.

Blacic, J.D. 1975. Plastic-deformation mechanisms in quartz: The effect of water. Tectonophysics, 27, 271-294.

Brandon, M.T. 1995. Analysis of geologic strain data in strain-magnitude space. Journal of Structural Geology, 17, 10, 1375-1385.

Brown, M., Diáz, F., and Grocott, J. 1993. Displacement history of the Atacama fault system 25°00'S-27°00'S, northern Chile. Geological Society of America Bulletin, 105, 1165-1174.

Busby-Spera, C.J. and Saleeby, J.B. 1990. Intra-arc strike-slip fault exposed at batholithic levels in southern Sierra Nevada, California. Geology, 18, 255-259.

Byerlee, J. 1978. Friction of rocks. Pageoph., 116, 615-626.

Cardozo, N., and Allmendinger, R.W. 2013. Spherical projections with OSXStereonet: Computers & Geosciences, 51, 193 – 205.

Cembrano, J., González, G., Arancibia, G., Ahumada, I., Olivares, V., and V. Herrera. 2005. Fault zone development and strain partitioning in an extensional strike-slip duplex: A case study from the Mesozoic Atacama fault system, Northern Chile. Tectonophysiscs, 400, 105-125.

Chisholm, E.I., Sircombe, K.N. and DiBugnara, D.L. 2014. Handbook of Geochronology Mineral Separation Laboratory Techniques. Record 2014/46. Geoscience Australia, Canberra.

Dallmeyer, R.D., Brown, M., Grocott, J., Taylor, G.K., Treloar, P.J. 1996. Mesozoic magmatic and tectonic events within the Andean Plate boundary zone, 26°-27°30'S, North Chile: Constraints from $^{40}Ar/^{39}Ar$ mineral ages. The Journal of Geology, 104, 9-40.

Dell'Angelo, L.N., and Tullis, J. 1996. Textural and mechanical evolution with progressive strain in experimentally deformed aplite. Tectonophysics, 256, 57-82.

Escribano, J.A., Martinez, P.E., Domagala, J., Padel, M., Espinoza, M.V., Jorquera, R.B., Contreras, J.P.F., de La Cruz, R.S., and Calderon, M.N. 2013 Cartas Bahia Isla Blanca y Taltal. Sernageomin, scale: 1:100,000.

Glazner, A.F. 1991. Plutonism, oblique subduction, and continental growth: An example from the Mesozoic of California. Geology, 19, 784-786.

Gomila, R., Arancibia, G., Mitchell, T.M., Cembrano, J.M., and Faulkner, D.R. 2016. Paleopermeatbility structure within fault-damage zones: A snap-shot from microfracture analyses in a strike-slip system. Journal of Structural Geology, 83, 103-120.

Goncalves, P., Oliot, E., Marquer, D., and Connolly, J.A.D. 2012. Role of chemical processes on shear zone formation: An example from the Grimsel metagranodiorite (Aar massif, Central Alps. Journal of Metamorphic Geology, 30, 703-722.

González, G.L., Dunai, T., Carrizo, D., and Allmendinger, R. 2006. Young displacements on the Atacama Fault System, northern Chile from field observations and cosmogenic $^{21}Ne$ concentrations. Tectonics, 25, 1-15.

Gottardi, R. and Teyssier, C. 2013. Thermomechanics of an extensional shear zone, Raft River metamorphic core complex, NW Utah. Journal of Structural Geology, 53, 54-69.

Grocott, J. and Taylor, G.K. 2002. Magmatic arc fault systems, deformation partitioning and emplacement of granitic complexes in the Coastal Cordillera, north Chilean Andes (25º30'S to 27 º00'S). Journal of the Geological Society, London, 159, 425-442.

Handy, M.R., Hirth, G., and Burgmann, R. 2007. Continental fault structure and rheology from the frictional-to-viscous transition downward. In Tectonic Faults: Agents of Change on a Dynamic Earth, ed. MR Handy, G Hirth, N Hovius, 139–81. Cambridge, MA: MIT.

Hirth, G. and Tullis, J. 1992. Dislocation creep regimes in quartz aggregates. Journal of Structural Geology, 14, 2, 145-159.

Holyoke, C.W. and Kronenberg, A.K. 2010. Accurate differential stress measurement using the molten salt cell and solid salt assemblies in the Griggs apparatus with applications to strength, piezometers, and rheology. Tectonophysics, 494, 17-31.

Jensen, E., Cembrano, J., Faulkner, D., Veloso, E., and Arancibia, G. 2011. Development of a self-similar strike-slip system in the Atacama Fault system, Chile. Journal of Structural Geology, 33, 1611-1626

Kidder, S., Avouac, J.P., and Chan, YC. 2012. Constraints from rocks in the Taiwan orogen on crustal stress levels and rheology. Journal of Geophysical Research, 117, 1-13.

Kidder, S.B., Toy, V.G., Prior, D.J. 2014. Transient Stress Magnitudes in the Middle Crust along the Alpine Fault. AGU Fall meeting Abstracts. T21D-03.

Kjøll, H.J., Viola, G., Menegon, L., and Sorensen, B.E. 2015. Brittle-viscous deformation of vein quartz under fluid-rich lower greenschist facies conditions. Solid Earth, 6, 681-699.

Kurth, D. 2000. The north-Chilean Costal Cordillera at Taltal: Shear-zones and forearc-sliver in the Jurassic and lower Cretaceous magmatic arc. [Ph.D. thesis]. Fachbereich Geowissenschaften, Freie Universität Berlin. p. 143.

Loveless, J.P., Allmendinger, R.W., Pritchard, M.E., and González, G. 2010. Normal and reverse faulting driven by the subduction zone earthquake cycle in the northern Chilean forearc. Tectonics, 29, 1-16. Marrett, R. A., and Allmendinger, R. W., 1990, Kinematic analysis of fault-slip data: Journal of Structural Geology, 12, 973-986.

Marsh, J.H. and Stockli, D.F. 2015. Zircon U-Pb and trace element zoning characteristics in an anatectic granulite domain: insights from LASS-ICP-MS depth profiling. Lithos, 239, 170-185.

Means, W.D. 1981. The Concept of Steady-State Foliation. Tectonophysics. vol. 78. p. 179-199.

Mitchell, T.M. and Faulkner, D.R. 2009. The nature and origin of off-fault damage surrounding strike-slip fault zones with a wide range of displacements: A field study from the Atacama fault system, northern Chile. Journal of Structural Geology, 31, 802-816.

Molnar, P. and Dayem, K.E. 2010. Major intracontinental strike-slip faults and contrasts in lithospheric strength. Geosphere, 6, 4, 444-467.

Morrow, C., Radney, B., and Byerlee, J.D. 1992. Frictional strength and the effective pressure law of montmorillonite and illite clays, in: B. Evans (Ed.), Fault Mechanics and Transport Properties of Rocks; A Festschrift in Honor of W.F. Brace, Academic Press, San Diego, CA, 69 - 88.

Nadin, E.S, Saleeby, J., and Wong, M. 2016. Thermal evolution of the Sierra Nevada batholith, California, and implications for strain localization. Geosphere, 12, 2, 377-399.

Oliot, E., Goncalves, P., and Marquer, D. 2010. Role of plagioclase and reaction softening in a metagranite shear zone at mid-crustal conditions (Gotthard massif, Swiss Central Alps). Journal of Metamorphic Geology, 28, 849-871.

Passchier, C.W. and Trouw, R.A.J. 2005. *Microtectonics*. Springer. Berlin. 56-57

Platt, J.P. 2015. Rheology of two-phase systems: A microphysical and observational approach. Journal of Structural Geology, 77, 213-227.

Rasband, W.S., ImageJ, U. S. National Institutes of Health, Bethesda, Maryland, USA, https://imagej.nih.gov/ij/, 1997-2016.

Reiners, P.W., Farley, K.A., and Hickes, H.J. 2002. He diffusion and (U-Th)/He thermochronometry of zircon: Initial results from Fish Canyon Tuff and Gold Butte. Tectonophysics, 349, 297–308.

Reiners, P.W., Spell, T., Nicolescu, S., and Zanetti, K. 2004. Zircon (U–Th)/He thermochronometry: He diffusion and comparisons with Ar-40/Ar-39 dating. Geochim. Cosmochim. Acta, 68, 1857–1887.

Reutter, K.J. and Scheuber, E. 1988. Relation between tectonics and magmatism in the Andes of northern Chile and adjacent areas between 21º and 25º S. Congreso Geológico Chileno, 1, A345–A363.

Robin, P.F., 2002. Determination of fabric and strain ellipsoids from measured sectional ellipses – theory. Journal of Structural Geology, 24, 531-544.

Rutter, E.H., Casey, M., and Burlini, L. 1994. Preferred crystallographic orientation development during the plastic and superplastic flow of calcite rocks. Journal of Structural Geology, 16, 10, 1431-1446.

Rutter, E.H., Faulkner, D.R., Brodie, K.H., Phillips, R.J., and Searle, M.P. 2007. Journal of Structural Geology, 29, 1315-1326.

Saint Blanquat, M., Tikoff, B., Teyssier, C., and Vingenresse, J.L. 1998. Transpressional kinematics and magmatic arcs. In: Holdsworth, R.E., Strachan, R.A., and Dewey, J.F. (eds.) 1998. Continental Transpressional and Transtensional tectonics. Geological Society, London. Special Publications, 135, 327-340.

Scheuber, E. and Andriessen, P.A. 1990. The kinematic and geodynamic significance of the Atacama fault zone, northern Chile. Journal of Structural Geology, 12, 2, 243 – 257.

Scheuber, E. and Gonzalez, G. 1999. Tectonics of the Jurassic-EC magmatic arc of the north Chilean Coastal Cordillera (22°-26°S): A story of crustal deformation along a convergent plate boundary. Tectonics, 18, 895-910.

Scheuber, E., Hammerschmidt, K., and Friedrichsen, H. 1995. $^{40}Ar/^{39}Ar$ and Rb-Sr analyses from ductile shear zones from the Atacama Fault Zone, northern Chile: the age of deformation. Tectonophysics, 250, 61-87.

Scheuber, E. and Reutter, K.J. 1992. Magmatic arc tectonics in the Central Andes between 21° and 25°S. Tectonophysics, 205, 127-140.

Schmidt, M.W. 1992. Amphibole composition in tonalite as a function of pressure: an experimental calibration of the Al-in-hornblende barometer. Contributions to Mineralogy and Petrology, 110, 304-310.

Shan, Y., 2008. An analytical approach for determining strain ellipsoids from measurements on planar surfaces. Journal of Structural Geology, 30, 539-546.

Sibson, R.H. 1977. Fault rocks and fault mechanisms. Journal of the Geological Society London, 133, 121-213.

Singleton, J.S., Wong, M.S., and Johnston, S.M., 2018, The role of calcite-rich metasedimentary mylonites in localizing detachment fault strain and influencing the structural evolution of the Buckskin-Rawhide metamorphic core complex: Lithosphere, 10, 172-193.

Stockhert, B., Brix, M.R., Kleinschrodt, R., Hurford, A.J., and Wirth, R. 1999. Thermochronometry and microstructures of quartz - A comparison with experimental flow laws and predictions on the temperature of the brittle-plastic transition: Journal of Structural Geology, 21, 351–369

Stockli, D. F. 2005. Application of low-temperature thermochronometry to extensional tectonic settings. Rev. Mineral. Geochem., 58, 411–448.

Stipp, M. and Kunze, K. 2008. Dynamic recrystallization near the brittle-plastic transition in naturally and experimentally deformed quartz aggregates. Tectonophysics, 448, 77-97.

Stipp, M., Stünitz, H., Heilbronner, R., and Schmid, S.M. 2002. The eastern Tonale fault zone: a 'natural laboratory' for crystal plastic deformation of quartz over a temperature range from 250 to 700 ºC. Journal of Structural Geology, 24, 1861-1884.

Tagami, T., Farley, K.A., and Stockli, D.F. 2003 (U-Th)/He geochronology of single zircon grains of known Tertiary eruption age. Earth and Planetary Science Letters, 207, 57-67.

Tikoff, B. and Saint Blanquat, M. 1997. Transpressional shearing and strike-slip partitioning in the Late Cretaceous Sierra Nevada magmatic arc, California. Tectonics, 16, 3, 442-459.

Toy, V.G., Prior, D.J., and Norris, R.J. 2008. Quartz fabrics in the Alpine fault mylonites: Influence of pre-existing preferred orientations on fabric development during progressive uplift. Journal of Structural Geology, 30, 602-621.

Veloso, E.E., Gomila, R., Cembrano, J., González, R., Jensen, E., and Arancibia, G. 2015. Stress fields recorded on large-scale strike-slip fault systems: Effects on the tectonic evolution of crustal slivers during oblique subduction. Tectonophysics, 664, 244-255.

Verdel, C., Niemi, N., van der Pluijm, B.A. 2011. Variations in the illite to muscovite transition related to metamorphic conditions and detrital muscovite content: insight from the Paleozoic passive margin of the southwestern United States. The Journal of Geology, 119, 419-437.

Vollmer, F.W., 2018. Automatic contouring of geologic fabric and finite strain data on the unit hyperboloid. Computers & Geosciences, 115, 134-142

Wallis, D., Lloyd, G.E., Phillips, R.J., Parsons, A.J., Walshaw, R.D. 2015. Low effective fault strength due to frictional-viscous flow in phyllonites, Karakoram fault zone, NW India. Journal of Structural Geology, 77, 45-61.

White, S.H., Burrows, S.E., Carreras, J., Shaw, N.D., and Humphreys, F.J. 1980. On mylonites in ductile shear zones. Journal of Structural Geology, 2, ½, 175-187.

Wolfe, M.R. and Stockli, D.F. 2010. Zircon (U-Th)/He thermochronometry in the KTB drill hole, Germany, and its implications for bulk He diffusion kinetics in zircon. Earth Planet. Sci. Lett., 295, 69–82.

# APPENDICES

**Appendix 1:** Table of isotope ratios collected for samples from the Late Jurassic granodiorite (16-1-P31), the Early Cretaceous granodiorite (17-1-P26), the aplite sill (17-1-P124), the Early Cretaceous tonalite (18-1-PJ73), and the Early Jurassic granodiorite (18-1-PJ81). The columns are ratios of $^{207}Pb/^{235}U$, 2 internal standard error of $^{207}Pb/^{235}U$, ratios of $^{206}Pb/^{238}U$, 2 internal standard error of $^{206}Pb/^{238}U$, ratios of $^{207}Pb/^{206}Pb$, 2 internal standard error of $^{207}Pb/^{206}Pb$, the error correlation between ratios $^{206}Pb/^{238}U$ and $^{207}Pb/^{235}U$, and the error correlation between $^{238}U/^{206}Pb$ and $^{207}Pb/^{206}Pb$ for columns 1, 2, 3, 4, 5, 6, 7, and 8, respectively.

| | 1 | 2 | 3 | 4 | 5 | 6 | 7 | 8 |
|---|---|---|---|---|---|---|---|---|
| Sample | Final207_235 | Final207_235_Int2SE | Final206_238 | Final206_238_Int2SE | Final207_206 | Final207_206_Int2SE | ErrorCorrelation_6_38vs7_35 | ErrorCorrelation_38_6vs7_6 |
| 16-1-P31 | 0.1701 | 0.0027 | 0.02426 | 0.00025 | 0.05016 | 0.00067 | 0.52463 | 0.12112 |
| 16-1-P31 | 0.283 | 0.055 | 0.02532 | 0.00076 | 0.077 | 0.011 | 0.95462 | -0.88285 |
| 16-1-P31 | 0.1728 | 0.0029 | 0.02411 | 0.00029 | 0.05158 | 0.0008 | 0.45423 | 0.26379 |
| 16-1-P31 | 0.1653 | 0.0027 | 0.02399 | 0.00021 | 0.04937 | 0.00076 | 0.33979 | 0.2035 |
| 16-1-P31 | 0.278 | 0.021 | 0.02503 | 0.00059 | 0.0783 | 0.005 | 0.56503 | -0.37599 |
| 16-1-P31 | 0.1581 | 0.0024 | 0.02298 | 0.00027 | 0.04939 | 0.00081 | 0.22155 | 0.47829 |
| 16-1-P31 | 0.1719 | 0.003 | 0.02418 | 0.00025 | 0.05114 | 0.0009 | 0.23489 | 0.38787 |
| 16-1-P31 | 0.1666 | 0.0028 | 0.02454 | 0.00029 | 0.049 | 0.00078 | 0.4652 | 0.28456 |
| 16-1-P31 | 0.1636 | 0.0022 | 0.02399 | 0.00027 | 0.04927 | 0.00064 | 0.45813 | 0.37409 |
| 16-1-P31 | 0.1724 | 0.0029 | 0.02417 | 0.00024 | 0.05153 | 0.00088 | 0.27449 | 0.30116 |
| 16-1-P31 | 0.1696 | 0.0031 | 0.02355 | 0.00031 | 0.05174 | 0.00099 | 0.29637 | 0.47437 |
| 16-1-P31 | 0.251 | 0.014 | 0.02351 | 0.00045 | 0.0767 | 0.0037 | 0.38864 | -0.019173 |
| 16-1-P31 | 0.1579 | 0.0022 | 0.02292 | 0.00027 | 0.04998 | 0.00074 | 0.34527 | 0.48505 |
| 16-1-P31 | 0.1618 | 0.0029 | 0.02283 | 0.00025 | 0.05125 | 0.00089 | 0.31814 | 0.33415 |
| 16-1-P31 | 0.1606 | 0.0029 | 0.02336 | 0.00024 | 0.04997 | 0.00078 | 0.50752 | -0.0088209 |
| 16-1-P31 | 0.287 | 0.05 | 0.02457 | 0.00071 | 0.076 | 0.0087 | 0.94144 | -0.85429 |
| 16-1-P31 | 0.1794 | 0.0038 | 0.0222 | 0.00024 | 0.0588 | 0.0013 | 0.20653 | 0.29798 |
| 16-1-P31 | 0.1631 | 0.003 | 0.02403 | 0.00035 | 0.04929 | 0.00077 | 0.56355 | 0.29814 |
| 16-1-P31 | 0.1668 | 0.0018 | 0.02437 | 0.00023 | 0.04967 | 0.00062 | 0.20677 | 0.55241 |
| 16-1-P31 | 0.1622 | 0.0036 | 0.02281 | 0.00025 | 0.0516 | 0.0011 | 0.31552 | 0.30095 |
| 16-1-P31 | 0.182 | 0.0056 | 0.02421 | 0.00018 | 0.0551 | 0.0017 | 0.37709 | -0.22368 |
| 16-1-P31 | 0.1726 | 0.0017 | 0.02525 | 0.00021 | 0.04963 | 0.00045 | 0.54275 | 0.31512 |
| 16-1-P31 | 0.189 | 0.011 | 0.02463 | 0.0003 | 0.0566 | 0.0031 | 0.4297 | -0.27903 |
| 16-1-P31 | 0.1525 | 0.0031 | 0.0224 | 0.00034 | 0.04934 | 0.00076 | 0.6682 | 0.15485 |
| 16-1-P31 | 0.1672 | 0.0022 | 0.02457 | 0.00022 | 0.0494 | 0.00058 | 0.48948 | 0.22017 |
| 16-1-P31 | 0.1565 | 0.0019 | 0.02291 | 0.00018 | 0.04991 | 0.00057 | 0.37297 | 0.30539 |
| 16-1-P31 | 0.1664 | 0.0023 | 0.02396 | 0.00023 | 0.05052 | 0.00079 | 0.31168 | 0.38058 |

| | | | | | | | | |
|---|---|---|---|---|---|---|---|---|
| 16-1-P31 | 0.1675 | 0.0028 | 0.02385 | 0.00024 | 0.05108 | 0.00084 | 0.31676 | 0.25172 |
| 16-1-P31 | 0.1698 | 0.004 | 0.02354 | 0.00033 | 0.0524 | 0.001 | 0.50713 | 0.086943 |
| 16-1-P31 | 0.1596 | 0.0022 | 0.02335 | 0.00023 | 0.04956 | 0.00059 | 0.4773 | 0.32561 |
| Sample | Final207_235 | Final207_235_Int2SE | Final206_238 | Final206_238_Int2SE | Final207_206 | Final207_206_Int2SE | ErrorCorrelation_6_38vs7_35 | ErrorCorrelation_38_6vs7_6 |
| 17-1-P26 | 0.1494 | 0.006 | 0.02088 | 0.0003 | 0.0523 | 0.0022 | 0.096329 | 0.25623 |
| 17-1-P26 | 0.1549 | 0.0066 | 0.0218 | 0.00033 | 0.0517 | 0.0023 | 0.15035 | 0.27273 |
| 17-1-P26 | 0.303 | 0.028 | 0.02407 | 0.0006 | 0.0891 | 0.0072 | 0.4488 | -0.19266 |
| 17-1-P26 | 0.203 | 0.012 | 0.02228 | 0.00033 | 0.0651 | 0.0034 | 0.44178 | -0.17308 |
| 17-1-P26 | 0.1699 | 0.006 | 0.02235 | 0.00038 | 0.055 | 0.0021 | -0.065591 | 0.38635 |
| 17-1-P26 | 0.1612 | 0.0084 | 0.02205 | 0.00036 | 0.0531 | 0.0028 | 0.11442 | 0.16868 |
| 17-1-P26 | 0.1588 | 0.0069 | 0.02216 | 0.00037 | 0.0518 | 0.0023 | 0.056679 | 0.29335 |
| 17-1-P26 | 0.1521 | 0.0085 | 0.02165 | 0.00053 | 0.0505 | 0.0027 | 0.19723 | 0.28249 |
| 17-1-P26 | 0.1518 | 0.0049 | 0.02157 | 0.00032 | 0.0511 | 0.0017 | 0.14488 | 0.33202 |
| 17-1-P26 | 0.1497 | 0.0057 | 0.02168 | 0.00038 | 0.0503 | 0.002 | 0.12204 | 0.3219 |
| 17-1-P26 | 0.276 | 0.016 | 0.02406 | 0.0005 | 0.083 | 0.0044 | 0.3318 | -0.050839 |
| 17-1-P26 | 0.209 | 0.017 | 0.02236 | 0.00048 | 0.0677 | 0.0052 | 0.21201 | -0.0022789 |
| 17-1-P26 | 0.141 | 0.0058 | 0.02135 | 0.0004 | 0.0483 | 0.002 | 0.20913 | 0.23344 |
| 17-1-P26 | 0.1447 | 0.0061 | 0.02151 | 0.00041 | 0.049 | 0.0021 | 0.2125 | 0.28927 |
| 17-1-P26 | 0.17 | 0.015 | 0.02264 | 0.00085 | 0.0548 | 0.0044 | 0.28686 | 0.15703 |
| 17-1-P26 | 0.1572 | 0.0088 | 0.02131 | 0.00045 | 0.0551 | 0.0034 | 0.16917 | 0.25403 |
| 17-1-P26 | 0.2024 | 0.0076 | 0.02133 | 0.00044 | 0.0686 | 0.0027 | 0.10268 | 0.37131 |
| 17-1-P26 | 0.259 | 0.014 | 0.02209 | 0.00051 | 0.0868 | 0.0048 | 0.31924 | 0.011294 |
| 17-1-P26 | 0.1681 | 0.0079 | 0.02266 | 0.00046 | 0.0544 | 0.0026 | 0.16312 | 0.092893 |
| 17-1-P26 | 0.1555 | 0.0062 | 0.02297 | 0.00053 | 0.0494 | 0.002 | 0.33566 | 0.34431 |
| 17-1-P26 | 0.803 | 0.048 | 0.0277 | 0.00089 | 0.207 | 0.01 | 0.5529 | -0.075985 |
| 17-1-P26 | 0.209 | 0.02 | 0.02215 | 0.0005 | 0.0673 | 0.0057 | 0.2865 | -0.081996 |
| 17-1-P26 | 0.1629 | 0.0077 | 0.02184 | 0.00037 | 0.0542 | 0.0025 | 0.13968 | 0.16447 |
| 17-1-P26 | 0.1434 | 0.0048 | 0.01926 | 0.00041 | 0.0544 | 0.0019 | 0.38848 | 0.3043 |
| 17-1-P26 | 0.1418 | 0.006 | 0.02186 | 0.00043 | 0.0472 | 0.0021 | 0.15136 | 0.38068 |
| 17-1-P26 | 0.1541 | 0.0071 | 0.02192 | 0.00056 | 0.0516 | 0.0024 | 0.22175 | 0.091422 |
| 17-1-P26 | 0.1435 | 0.008 | 0.02126 | 0.00044 | 0.0488 | 0.0026 | 0.21477 | 0.19779 |
| 17-1-P26 | 0.69 | 0.032 | 0.02687 | 0.00073 | 0.1919 | 0.0088 | 0.59094 | -0.024161 |
| 17-1-P26 | 0.1722 | 0.0099 | 0.02286 | 0.0009 | 0.0545 | 0.0029 | 0.45551 | 0.34842 |
| Sample | Final207_235 | Final207_235_Int2SE | Final206_238 | Final206_238_Int2SE | Final207_206 | Final207_206_Int2SE | ErrorCorrelation_6_38vs7_35 | ErrorCorrelation_38_6vs7_6 |
| 17-1-P124 | 0.238 | 0.012 | 0.02316 | 0.00033 | 0.0762 | 0.0039 | 0.21277 | 0.064486 |
| 17-1-P124 | 0.171 | 0.011 | 0.02236 | 0.00049 | 0.0552 | 0.0035 | 0.046926 | 0.34485 |

| | | | | | | | | |
|---|---|---|---|---|---|---|---|---|
| 17-1-P124 | 0.1472 | 0.0095 | 0.02243 | 0.00045 | 0.0482 | 0.0032 | 0.090445 | 0.22764 |
| 17-1-P124 | 0.139 | 0.014 | 0.02249 | 0.00067 | 0.0471 | 0.0049 | -0.022805 | 0.27526 |
| 17-1-P124 | 0.1963 | 0.0092 | 0.02203 | 0.00037 | 0.0653 | 0.0033 | -0.078652 | 0.38414 |
| 17-1-P124 | 0.1492 | 0.0018 | 0.02187 | 0.00013 | 0.04986 | 0.00062 | 0.21576 | 0.30799 |
| 17-1-P124 | 0.162 | 0.011 | 0.02254 | 0.00044 | 0.0535 | 0.0038 | -0.042937 | 0.29899 |
| 17-1-P124 | 0.176 | 0.011 | 0.02321 | 0.00052 | 0.0559 | 0.0036 | 0.16462 | 0.15098 |
| 17-1-P124 | 0.1482 | 0.0094 | 0.02179 | 0.00042 | 0.0507 | 0.0034 | -0.072067 | 0.35303 |
| 17-1-P124 | 0.1483 | 0.0065 | 0.02186 | 0.0004 | 0.0499 | 0.0022 | 0.12307 | 0.26325 |
| 17-1-P124 | 0.161 | 0.012 | 0.02196 | 0.00063 | 0.0547 | 0.0043 | 0.01196 | 0.37355 |
| 17-1-P124 | 0.198 | 0.0094 | 0.0225 | 0.00024 | 0.0636 | 0.0027 | 0.2516 | -0.060229 |
| 17-1-P124 | 0.154 | 0.0036 | 0.02211 | 0.00019 | 0.0505 | 0.0011 | 0.16224 | 0.1571 |
| 17-1-P124 | 0.143 | 0.0096 | 0.02154 | 0.00045 | 0.0498 | 0.0035 | 0.10297 | 0.17454 |
| 17-1-P124 | 0.1679 | 0.0065 | 0.02221 | 0.00027 | 0.0555 | 0.0023 | -0.058463 | 0.33341 |
| 17-1-P124 | 0.0218 | 0.0027 | 0.00331 | 0.00012 | 0.0494 | 0.006 | 0.12699 | 0.25497 |
| 17-1-P124 | 0.163 | 0.0029 | 0.02252 | 0.0002 | 0.05293 | 0.00096 | 0.19992 | 0.25357 |
| 17-1-P124 | 0.2036 | 0.0062 | 0.02278 | 0.00018 | 0.065 | 0.0017 | 0.47274 | -0.27898 |
| 17-1-P124 | 0.194 | 0.018 | 0.02321 | 0.00058 | 0.0619 | 0.006 | 0.017689 | 0.25962 |
| 17-1-P124 | 0.16 | 0.0025 | 0.02307 | 0.00016 | 0.05071 | 0.00077 | 0.24413 | 0.20038 |
| 17-1-P124 | 0.2054 | 0.0095 | 0.02237 | 0.00035 | 0.0671 | 0.0031 | 0.092211 | 0.23067 |
| 17-1-P124 | 0.1694 | 0.0035 | 0.02391 | 0.00024 | 0.0518 | 0.001 | 0.34811 | 0.13704 |
| 17-1-P124 | 0.1842 | 0.0077 | 0.02348 | 0.00025 | 0.0591 | 0.0032 | 0.20309 | -0.04113 |
| 17-1-P124 | 1.101 | 0.038 | 0.03121 | 0.00052 | 0.2579 | 0.0068 | 0.74371 | -0.41853 |
| 17-1-P124 | 0.147 | 0.012 | 0.02206 | 0.00052 | 0.048 | 0.0038 | 0.056316 | 0.25444 |
| 17-1-P124 | 0.1553 | 0.0053 | 0.02264 | 0.00028 | 0.0501 | 0.0017 | 0.076443 | 0.26786 |
| 17-1-P124 | 0.1626 | 0.0029 | 0.02255 | 0.00019 | 0.0527 | 0.001 | 0.014478 | 0.38608 |
| 17-1-P124 | 0.277 | 0.028 | 0.02291 | 0.00063 | 0.0874 | 0.0084 | 0.34609 | -0.11839 |
| 17-1-P124 | 0.1503 | 0.0051 | 0.02227 | 0.00025 | 0.0493 | 0.0018 | 0.031678 | 0.2757 |
| 17-1-P124 | 0.2106 | 0.007 | 0.02302 | 0.00026 | 0.066 | 0.0022 | -0.14511 | 0.45625 |
| 17-1-P124 | 0.162 | 0.0034 | 0.02288 | 0.00019 | 0.0514 | 0.0011 | 0.093748 | 0.28943 |
| 17-1-P124 | 0.1531 | 0.0016 | 0.02215 | 0.00012 | 0.05044 | 0.0005 | 0.37281 | 0.16683 |
| Sample | Final207_235 | Final207_235_Int2SE | Final206_238 | Final206_238_Int2SE | Final207_206 | Final207_206_Int2SE | ErrorCorrelation_6_38vs7_35 | ErrorCorrelation_38_6vs7_6 |
| 18-1-PJ73 | 0.333 | 0.018 | 0.02158 | 0.0005 | 0.1129 | 0.0065 | 0.098748 | 0.31925 |
| 18-1-PJ73 | 0.1393 | 0.0087 | 0.02102 | 0.00045 | 0.0485 | 0.0032 | -0.03589 | 0.36102 |
| 18-1-PJ73 | 0.1467 | 0.0071 | 0.02192 | 0.00038 | 0.0493 | 0.0023 | 0.31471 | -0.03072 |
| 18-1-PJ73 | 0.1457 | 0.0063 | 0.02157 | 0.00038 | 0.0499 | 0.0024 | -0.030716 | 0.32391 |
| 18-1-PJ73 | 0.1626 | 0.0071 | 0.02178 | 0.00029 | 0.0553 | 0.0026 | 0.059073 | 0.19786 |
| 18-1-PJ73 | 0.1475 | 0.0052 | 0.0214 | 0.00025 | 0.0498 | 0.0017 | 0.19135 | 0.1746 |

| | | | | | | | | |
|---|---|---|---|---|---|---|---|---|
| 18-1-PJ73 | 0.1581 | 0.0056 | 0.02076 | 0.00024 | 0.0552 | 0.002 | 0.15423 | 0.17885 |
| 18-1-PJ73 | 0.1531 | 0.0077 | 0.02137 | 0.00036 | 0.0522 | 0.0026 | 0.14358 | 0.18184 |
| 18-1-PJ73 | 0.209 | 0.01 | 0.02103 | 0.0004 | 0.0711 | 0.0032 | 0.2582 | 0.14108 |
| 18-1-PJ73 | 0.1577 | 0.0088 | 0.02119 | 0.00042 | 0.0537 | 0.003 | 0.22181 | 0.10705 |
| 18-1-PJ73 | 0.1582 | 0.0065 | 0.02176 | 0.00028 | 0.053 | 0.0021 | 0.24475 | -0.026774 |
| 18-1-PJ73 | 0.223 | 0.014 | 0.02205 | 0.00033 | 0.0736 | 0.0043 | 0.33039 | -0.11428 |
| 18-1-PJ73 | 0.1483 | 0.0071 | 0.02079 | 0.00032 | 0.0521 | 0.0025 | 0.15295 | 0.16533 |
| 18-1-PJ73 | 0.1438 | 0.0076 | 0.02081 | 0.00043 | 0.0514 | 0.0029 | 0.2167 | 0.17326 |
| 18-1-PJ73 | 0.1646 | 0.0089 | 0.02051 | 0.00035 | 0.0579 | 0.0028 | 0.37195 | 0.0072934 |
| 18-1-PJ73 | 0.141 | 0.0064 | 0.02101 | 0.00032 | 0.0482 | 0.0021 | 0.10228 | 0.19394 |
| 18-1-PJ73 | 0.234 | 0.012 | 0.02254 | 0.00042 | 0.075 | 0.0042 | -0.093519 | 0.44094 |
| 18-1-PJ73 | 0.2149 | 0.0073 | 0.0219 | 0.00028 | 0.0711 | 0.0023 | 0.32774 | 0.064295 |
| 18-1-PJ73 | 0.171 | 0.013 | 0.02248 | 0.00053 | 0.0547 | 0.0039 | 0.29154 | 0.06258 |
| 18-1-PJ73 | 0.6 | 0.025 | 0.02638 | 0.00054 | 0.1672 | 0.0067 | 0.35628 | 0.13122 |
| 18-1-PJ73 | 0.369 | 0.033 | 0.02517 | 0.00061 | 0.1045 | 0.008 | 0.48744 | -0.29149 |
| 18-1-PJ73 | 0.395 | 0.019 | 0.02377 | 0.0005 | 0.1231 | 0.006 | 0.25446 | 0.10624 |
| 18-1-PJ73 | 0.41 | 0.021 | 0.02348 | 0.00042 | 0.1272 | 0.0061 | 0.40439 | -0.073599 |
| 18-1-PJ73 | 0.1389 | 0.0073 | 0.02182 | 0.00039 | 0.047 | 0.0025 | 0.14238 | 0.21829 |
| 18-1-PJ73 | 0.221 | 0.013 | 0.02172 | 0.0004 | 0.0746 | 0.0043 | 0.22538 | 0.058537 |
| 18-1-PJ73 | 0.147 | 0.0085 | 0.02028 | 0.0004 | 0.0538 | 0.0033 | 0.10979 | 0.24725 |
| 18-1-PJ73 | 0.224 | 0.015 | 0.02197 | 0.00029 | 0.0745 | 0.0048 | 0.45159 | -0.2318 |
| 18-1-PJ73 | 0.1495 | 0.0065 | 0.02063 | 0.00034 | 0.0523 | 0.0023 | 0.062884 | 0.30398 |
| Sample | Final207_235 | Final207_235_Int2SE | Final206_238 | Final206_238_Int2SE | Final207_206 | Final207_206_Int2SE | ErrorCorrelation_6_38vs7_35 | ErrorCorrelation_38_6vs7_6 |
| 18-1-PJ81 | 0.1972 | 0.0051 | 0.02793 | 0.00026 | 0.0517 | 0.0013 | 0.25805 | 0.093123 |
| 18-1-PJ81 | 0.1803 | 0.0047 | 0.02619 | 0.00032 | 0.0502 | 0.0014 | 0.20067 | 0.1751 |
| 18-1-PJ81 | 0.1991 | 0.0056 | 0.02883 | 0.00034 | 0.0501 | 0.0015 | 0.045919 | 0.35039 |
| 18-1-PJ81 | 0.2033 | 0.0087 | 0.02928 | 0.00039 | 0.0501 | 0.0021 | 0.18152 | 0.15736 |
| 18-1-PJ81 | 0.1873 | 0.0071 | 0.02707 | 0.00047 | 0.0506 | 0.0019 | 0.28793 | 0.22608 |
| 18-1-PJ81 | 0.2089 | 0.0071 | 0.02873 | 0.00034 | 0.0526 | 0.0018 | 0.091796 | 0.26082 |
| 18-1-PJ81 | 0.2007 | 0.0055 | 0.02828 | 0.00027 | 0.0515 | 0.0015 | 0.0053923 | 0.34529 |
| 18-1-PJ81 | 0.1868 | 0.0075 | 0.02879 | 0.00038 | 0.0471 | 0.0019 | 0.11937 | 0.19313 |
| 18-1-PJ81 | 0.1984 | 0.0046 | 0.02842 | 0.00027 | 0.0511 | 0.0012 | 0.22073 | 0.2084 |
| 18-1-PJ81 | 0.1878 | 0.0064 | 0.028 | 0.00038 | 0.0488 | 0.0017 | 0.13213 | 0.30282 |
| 18-1-PJ81 | 0.2119 | 0.0069 | 0.02912 | 0.00033 | 0.053 | 0.0018 | 0.04606 | 0.28491 |
| 18-1-PJ81 | 0.1959 | 0.0051 | 0.02775 | 0.00035 | 0.0513 | 0.0014 | 0.17169 | 0.31447 |
| 18-1-PJ81 | 0.1895 | 0.0064 | 0.02757 | 0.00042 | 0.0501 | 0.0018 | 0.029543 | 0.36349 |
| 18-1-PJ81 | 0.1913 | 0.0054 | 0.02602 | 0.00034 | 0.0528 | 0.0016 | 0.14751 | 0.31901 |

| | | | | | | | | |
|---|---|---|---|---|---|---|---|---|
| 18-1-PJ81 | 0.1906 | 0.0046 | 0.02751 | 0.00026 | 0.0502 | 0.0012 | 0.22666 | 0.19605 |
| 18-1-PJ81 | 0.1997 | 0.0071 | 0.02889 | 0.00034 | 0.05 | 0.0019 | 0.03196 | 0.30428 |
| 18-1-PJ81 | 0.1964 | 0.0068 | 0.0288 | 0.00035 | 0.0493 | 0.0018 | -0.10318 | 0.38494 |
| 18-1-PJ81 | 0.2011 | 0.0049 | 0.02905 | 0.00029 | 0.0502 | 0.0012 | 0.1701 | 0.24025 |
| 18-1-PJ81 | 0.1845 | 0.0061 | 0.02691 | 0.00034 | 0.0496 | 0.0017 | 0.099631 | 0.269 |
| 18-1-PJ81 | 0.193 | 0.0079 | 0.02683 | 0.00044 | 0.0521 | 0.0021 | 0.21543 | 0.23198 |
| 18-1-PJ81 | 0.1991 | 0.0054 | 0.02733 | 0.00033 | 0.0531 | 0.0015 | 0.2116 | 0.20476 |
| 18-1-PJ81 | 0.1913 | 0.0039 | 0.02786 | 0.00022 | 0.05 | 0.0011 | 0.13611 | 0.25659 |
| 18-1-PJ81 | 0.1852 | 0.0044 | 0.02756 | 0.00026 | 0.0488 | 0.0012 | 0.064818 | 0.30298 |
| 18-1-PJ81 | 0.1979 | 0.006 | 0.02843 | 0.00038 | 0.0506 | 0.0017 | 0.10531 | 0.29841 |
| 18-1-PJ81 | 0.1976 | 0.0046 | 0.0283 | 0.00025 | 0.0509 | 0.0012 | 0.12409 | 0.26027 |
| 18-1-PJ81 | 0.1899 | 0.008 | 0.02663 | 0.00036 | 0.0526 | 0.0024 | 0.020146 | 0.34008 |
| 18-1-PJ81 | 0.1795 | 0.0047 | 0.02634 | 0.00029 | 0.0496 | 0.0014 | 0.19209 | 0.17801 |
| 18-1-PJ81 | 0.195 | 0.0032 | 0.02804 | 0.00035 | 0.05061 | 0.00074 | 0.57422 | 0.3787 |
| 18-1-PJ81 | 0.2023 | 0.0052 | 0.02977 | 0.00032 | 0.0495 | 0.0013 | 0.1138 | 0.26549 |
| 18-1-PJ81 | 0.2079 | 0.0069 | 0.0287 | 0.0003 | 0.0531 | 0.0019 | 0.23563 | 0.022619 |
| 18-1-PJ81 | 0.2213 | 0.0081 | 0.02938 | 0.00039 | 0.0547 | 0.0021 | -0.019264 | 0.36201 |
| 18-1-PJ81 | 0.186 | 0.0047 | 0.02666 | 0.00034 | 0.0506 | 0.0012 | 0.34337 | 0.18794 |
| 18-1-PJ81 | 0.2119 | 0.007 | 0.02836 | 0.0003 | 0.0543 | 0.0018 | 0.09101 | 0.22582 |
| 18-1-PJ81 | 0.1953 | 0.0034 | 0.02797 | 0.00028 | 0.05079 | 0.00095 | 0.16097 | 0.39559 |
| 18-1-PJ81 | 0.2035 | 0.0077 | 0.029 | 0.00042 | 0.0513 | 0.0021 | 0.056893 | 0.31293 |
| 18-1-PJ81 | 0.2047 | 0.0067 | 0.02773 | 0.00025 | 0.0534 | 0.0017 | 0.22189 | 0.02236 |
| 18-1-PJ81 | 0.1951 | 0.0063 | 0.02839 | 0.0003 | 0.0497 | 0.0016 | 0.097504 | 0.24549 |
| 18-1-PJ81 | 0.1929 | 0.0093 | 0.02792 | 0.00043 | 0.0502 | 0.0026 | -0.0078653 | 0.33984 |
| 18-1-PJ81 | 0.1837 | 0.0063 | 0.02728 | 0.0004 | 0.0491 | 0.0019 | 0.028662 | 0.37322 |
| 18-1-PJ81 | 0.1899 | 0.0046 | 0.02738 | 0.00025 | 0.0505 | 0.0013 | 0.10996 | 0.26056 |
| 18-1-PJ81 | 0.1829 | 0.0049 | 0.02702 | 0.00031 | 0.0495 | 0.0013 | 0.18012 | 0.24438 |

**Appendix 2:** Table of isotope ratios collected for samples from the Late Jurassic granodiorite (16-1-P31), the Early Cretaceous granodiorite (17-1-P26), the aplite sill (17-1-P124), the Early Cretaceous tonalite (18-1-PJ73), and the Early Jurassic granodiorite (18-1-PJ81). The columns are duration of measurement, the dates using $^{207}Pb/^{235}U$ (my), the 2 internal standard error dates using $^{207}Pb/^{235}U$ (my), the dates using $^{206}Pb/^{238}U$ (my), the 2 internal standard error dates using $^{206}Pb/^{238}U$ (my), the dates using $^{207}Pb/^{206}Pb$ (my), and the 2 internal standard error dates using $^{207}$ Pb/ (my) columns 1, 2, 3, 4, 5, 6, and 7, respectively.

| | 1 | 2 | 3 | 4 | 5 | 6 | 7 |
|---|---|---|---|---|---|---|---|
| **Sample** | **Duration (sec)** | **FinalAge 207_235** | **FinalAge 207_235_Int2SE** | **FinalAge 206_238** | **FinalAge 206_238_Int2SE** | **FinalAge 207_206** | **FinalAge 207_206_Int2SE** |
| 16-1-P31 | 28 | 159.4 | 2.4 | 154.5 | 1.6 | 199.0 | 30.0 |
| 16-1-P31 | 29 | 237.0 | 35.0 | 161.1 | 4.8 | 810.0 | 180.0 |
| 16-1-P31 | 29 | 161.8 | 2.5 | 153.6 | 1.8 | 257.0 | 34.0 |
| 16-1-P31 | 24 | 155.2 | 2.4 | 152.8 | 1.3 | 163.0 | 34.0 |
| 16-1-P31 | 29 | 244.0 | 16.0 | 159.3 | 3.7 | 980.0 | 120.0 |
| 16-1-P31 | 24 | 149.0 | 2.1 | 146.4 | 1.7 | 169.0 | 37.0 |
| 16-1-P31 | 24 | 161.0 | 2.6 | 154.0 | 1.6 | 243.0 | 40.0 |
| 16-1-P31 | 24 | 156.4 | 2.4 | 156.3 | 1.8 | 146.0 | 34.0 |
| 16-1-P31 | 24 | 153.8 | 1.9 | 152.8 | 1.7 | 159.0 | 28.0 |
| 16-1-P31 | 24 | 161.4 | 2.5 | 153.9 | 1.5 | 259.0 | 38.0 |
| 16-1-P31 | 24 | 159.3 | 2.8 | 150.1 | 2.0 | 273.0 | 44.0 |
| 16-1-P31 | 27 | 225.0 | 11.0 | 149.8 | 2.9 | 1024.0 | 97.0 |
| 16-1-P31 | 24 | 148.8 | 2.0 | 146.1 | 1.7 | 187.0 | 32.0 |
| 16-1-P31 | 24 | 152.2 | 2.5 | 145.5 | 1.6 | 247.0 | 40.0 |
| 16-1-P31 | 24 | 151.1 | 2.5 | 148.8 | 1.5 | 193.0 | 35.0 |
| 16-1-P31 | 29 | 237.0 | 30.0 | 156.4 | 4.5 | 930.0 | 170.0 |
| 16-1-P31 | 24 | 167.4 | 3.3 | 141.6 | 1.5 | 539.0 | 48.0 |
| 16-1-P31 | 24 | 153.7 | 2.7 | 153.0 | 2.2 | 159.0 | 34.0 |
| 16-1-P31 | 29 | 156.6 | 1.6 | 155.2 | 1.5 | 175.0 | 28.0 |
| 16-1-P31 | 24 | 153.0 | 3.3 | 145.4 | 1.6 | 267.0 | 50.0 |
| 16-1-P31 | 27 | 169.4 | 4.7 | 154.2 | 1.1 | 398.0 | 65.0 |
| 16-1-P31 | 24 | 161.6 | 1.5 | 160.8 | 1.3 | 175.0 | 21.0 |
| 16-1-P31 | 29 | 173.1 | 7.9 | 156.9 | 1.9 | 382.0 | 85.0 |
| 16-1-P31 | 24 | 144.0 | 2.7 | 142.8 | 2.1 | 160.0 | 33.0 |
| 16-1-P31 | 24 | 156.9 | 1.9 | 156.5 | 1.4 | 165.0 | 26.0 |
| 16-1-P31 | 24 | 147.6 | 1.7 | 146.0 | 1.2 | 186.0 | 26.0 |
| 16-1-P31 | 24 | 156.2 | 2.0 | 152.6 | 1.4 | 211.0 | 34.0 |
| 16-1-P31 | 24 | 157.2 | 2.4 | 151.9 | 1.5 | 241.0 | 37.0 |
| 16-1-P31 | 29 | 159.0 | 3.4 | 150.0 | 2.1 | 292.0 | 43.0 |
| 16-1-P31 | 24 | 150.3 | 1.9 | 148.8 | 1.5 | 170.0 | 27.0 |
| **Sample** | **Duration (sec)** | **FinalAge 207_235** | **FinalAge 207_235_Int2SE** | **FinalAge 206_238** | **FinalAge 206_238_Int2SE** | **FinalAge 207_206** | **FinalAge 207_206_Int2SE** |

| | | | | | | | |
|---|---|---|---|---|---|---|---|
| 17-1-P26 | 38 | 140.7 | 5.3 | 133.2 | 1.9 | 248.0 | 80.0 |
| 17-1-P26 | 38 | 146.0 | 5.9 | 139.0 | 2.1 | 229.0 | 85.0 |
| 17-1-P26 | 18 | 263.0 | 21.0 | 153.3 | 3.8 | 1250.0 | 170.0 |
| 17-1-P26 | 38 | 185.5 | 9.6 | 142.1 | 2.1 | 668.0 | 99.0 |
| 17-1-P26 | 28 | 158.8 | 5.2 | 142.5 | 2.4 | 390.0 | 85.0 |
| 17-1-P26 | 38 | 150.4 | 7.2 | 140.6 | 2.3 | 268.0 | 97.0 |
| 17-1-P26 | 38 | 148.7 | 6.0 | 141.3 | 2.4 | 253.0 | 89.0 |
| 17-1-P26 | 22 | 142.9 | 7.4 | 138.0 | 3.4 | 200.0 | 110.0 |
| 17-1-P26 | 38 | 143.0 | 4.3 | 137.6 | 2.0 | 218.0 | 66.0 |
| 17-1-P26 | 38 | 141.0 | 5.0 | 138.2 | 2.4 | 184.0 | 75.0 |
| 17-1-P26 | 33 | 244.0 | 12.0 | 153.3 | 3.2 | 1190.0 | 110.0 |
| 17-1-P26 | 38 | 189.0 | 14.0 | 142.5 | 3.0 | 630.0 | 140.0 |
| 17-1-P26 | 38 | 133.3 | 5.2 | 136.2 | 2.5 | 111.0 | 80.0 |
| 17-1-P26 | 38 | 136.5 | 5.4 | 137.2 | 2.6 | 132.0 | 81.0 |
| 17-1-P26 | 13 | 158.0 | 13.0 | 144.3 | 5.4 | 330.0 | 160.0 |
| 17-1-P26 | 19 | 148.7 | 8.1 | 135.9 | 2.8 | 340.0 | 120.0 |
| 17-1-P26 | 19 | 186.6 | 6.4 | 136.1 | 2.8 | 854.0 | 86.0 |
| 17-1-P26 | 26 | 232.0 | 11.0 | 140.8 | 3.2 | 1270.0 | 120.0 |
| 17-1-P26 | 38 | 156.6 | 6.8 | 144.8 | 3.0 | 315.0 | 91.0 |
| 17-1-P26 | 28 | 146.8 | 5.6 | 146.4 | 3.4 | 159.0 | 79.0 |
| 17-1-P26 | 24 | 586.0 | 27.0 | 176.0 | 5.6 | 2815.0 | 86.0 |
| 17-1-P26 | 27 | 188.0 | 16.0 | 141.2 | 3.1 | 730.0 | 150.0 |
| 17-1-P26 | 38 | 152.9 | 6.8 | 139.2 | 2.3 | 352.0 | 95.0 |
| 17-1-P26 | 28 | 135.7 | 4.3 | 123.0 | 2.6 | 370.0 | 69.0 |
| 17-1-P26 | 38 | 133.9 | 5.3 | 139.4 | 2.7 | 62.0 | 80.0 |
| 17-1-P26 | 27 | 144.8 | 6.2 | 139.8 | 3.5 | 225.0 | 88.0 |
| 17-1-P26 | 24 | 135.4 | 7.0 | 135.6 | 2.8 | 140.0 | 100.0 |
| 17-1-P26 | 21 | 532.0 | 20.0 | 170.9 | 4.6 | 2716.0 | 77.0 |
| 17-1-P26 | 13 | 160.6 | 8.6 | 145.7 | 5.6 | 370.0 | 110.0 |
| **Sample** | **Duration (sec)** | **FinalAge 207_235** | **FinalAge 207_235_Int2SE** | **FinalAge 206_238** | **FinalAge 206_238_Int2SE** | **FinalAge 207_206** | **FinalAge 207_206_Int2SE** |
| 17-1-P118 | 38 | 180.0 | 10.0 | 181.0 | 3.3 | 180.0 | 110.0 |
| 17-1-P118 | 38 | 182.0 | 10.0 | 185.2 | 4.0 | 180.0 | 120.0 |
| 17-1-P118 | 38 | 189.0 | 10.0 | 179.8 | 4.2 | 300.0 | 120.0 |
| 17-1-P118 | 38 | 177.2 | 9.3 | 182.8 | 3.8 | 130.0 | 100.0 |
| 17-1-P118 | 38 | 184.0 | 11.0 | 181.8 | 3.9 | 210.0 | 120.0 |
| 17-1-P118 | 38 | 180.6 | 7.3 | 183.3 | 2.8 | 159.0 | 83.0 |
| 17-1-P118 | 38 | 179.6 | 7.3 | 183.4 | 2.9 | 147.0 | 84.0 |
| 17-1-P118 | 38 | 187.9 | 8.8 | 183.1 | 3.2 | 233.0 | 99.0 |
| 17-1-P118 | 38 | 184.0 | 10.0 | 185.2 | 3.5 | 190.0 | 110.0 |
| 17-1-P118 | 38 | 187.5 | 7.5 | 185.1 | 3.2 | 231.0 | 90.0 |
| 17-1-P118 | 38 | 173.0 | 13.0 | 179.8 | 4.3 | 100.0 | 140.0 |
| 17-1-P118 | 38 | 176.0 | 11.0 | 186.6 | 4.0 | 110.0 | 120.0 |
| 17-1-P118 | 38 | 175.9 | 9.7 | 184.8 | 3.9 | 100.0 | 110.0 |
| 17-1-P118 | 38 | 174.0 | 11.0 | 183.4 | 3.6 | 60.0 | 120.0 |

| | | | | | | | |
|---|---|---|---|---|---|---|---|
| 17-1-P118 | 38 | 185.0 | 11.0 | 182.7 | 3.6 | 190.0 | 120.0 |
| 17-1-P118 | 38 | 186.0 | 9.9 | 183.0 | 3.3 | 210.0 | 110.0 |
| 17-1-P118 | 37 | 226.0 | 11.0 | 183.9 | 3.2 | 610.0 | 110.0 |
| 17-1-P118 | 38 | 186.9 | 9.4 | 179.9 | 3.0 | 250.0 | 100.0 |
| 17-1-P118 | 38 | 181.0 | 10.0 | 186.9 | 3.6 | 110.0 | 110.0 |
| 17-1-P118 | 38 | 167.4 | 9.4 | 182.6 | 3.5 | 50.0 | 110.0 |
| 17-1-P118 | 38 | 183.0 | 11.0 | 179.3 | 3.8 | 250.0 | 120.0 |
| 17-1-P118 | 38 | 178.0 | 12.0 | 181.7 | 4.2 | 130.0 | 130.0 |
| 17-1-P118 | 38 | 182.8 | 9.8 | 185.8 | 3.3 | 160.0 | 110.0 |
| 17-1-P118 | 38 | 178.0 | 10.0 | 180.3 | 3.7 | 160.0 | 110.0 |
| 17-1-P118 | 38 | 174.7 | 9.7 | 180.5 | 3.2 | 130.0 | 110.0 |
| 17-1-P118 | 38 | 182.8 | 9.9 | 183.0 | 3.4 | 150.0 | 100.0 |
| 17-1-P118 | 38 | 182.9 | 9.7 | 177.7 | 3.6 | 240.0 | 110.0 |
| 17-1-P118 | 38 | 180.0 | 9.2 | 182.2 | 3.5 | 160.0 | 110.0 |
| 17-1-P118 | 38 | 173.9 | 7.5 | 180.2 | 2.6 | 118.0 | 89.0 |
| 17-1-P118 | 38 | 183.0 | 12.0 | 181.4 | 4.1 | 210.0 | 140.0 |
| 17-1-P118 | 38 | 182.6 | 7.7 | 187.0 | 2.7 | 144.0 | 89.0 |
| 17-1-P118 | 38 | 181.0 | 10.0 | 184.2 | 3.6 | 150.0 | 120.0 |
| 17-1-P118 | 38 | 345.0 | 18.0 | 197.4 | 4.0 | 1380.0 | 120.0 |
| 17-1-P118 | 38 | 181.0 | 10.0 | 183.2 | 3.7 | 160.0 | 110.0 |
| 17-1-P118 | 38 | 185.7 | 8.6 | 181.3 | 3.0 | 231.0 | 99.0 |
| **Sample** | **Duration (sec)** | **FinalAge 207_235** | **FinalAge 207_235_Int2SE** | **FinalAge 206_238** | **FinalAge 206_238_Int2SE** | **FinalAge 207_206** | **FinalAge 207_206_Int2SE** |
| 17-1-P124 | 38 | 214.4 | 9.3 | 147.6 | 2.1 | 951.0 | 98.0 |
| 17-1-P124 | 38 | 157.7 | 9.2 | 142.5 | 3.1 | 340.0 | 120.0 |
| 17-1-P124 | 38 | 137.7 | 8.3 | 143.0 | 2.8 | 80.0 | 110.0 |
| 17-1-P124 | 37 | 129.0 | 12.0 | 143.3 | 4.2 | -40.0 | 160.0 |
| 17-1-P124 | 38 | 180.4 | 7.8 | 140.5 | 2.3 | 670.0 | 100.0 |
| 17-1-P124 | 38 | 141.2 | 1.6 | 139.5 | 0.8 | 183.0 | 27.0 |
| 17-1-P124 | 38 | 150.3 | 9.4 | 143.7 | 2.8 | 250.0 | 130.0 |
| 17-1-P124 | 25 | 164.3 | 9.7 | 147.9 | 3.3 | 360.0 | 120.0 |
| 17-1-P124 | 38 | 138.6 | 8.2 | 138.9 | 2.6 | 150.0 | 120.0 |
| 17-1-P124 | 38 | 139.6 | 5.7 | 139.3 | 2.5 | 164.0 | 83.0 |
| 17-1-P124 | 28 | 149.0 | 11.0 | 140.0 | 4.0 | 300.0 | 150.0 |
| 17-1-P124 | 28 | 182.4 | 7.7 | 143.4 | 1.5 | 705.0 | 90.0 |
| 17-1-P124 | 38 | 145.2 | 3.2 | 141.0 | 1.2 | 211.0 | 46.0 |
| 17-1-P124 | 38 | 134.9 | 8.6 | 137.4 | 2.8 | 120.0 | 120.0 |
| 17-1-P124 | 25 | 157.0 | 5.7 | 141.6 | 1.7 | 384.0 | 86.0 |
| 17-1-P124 | 38 | 21.7 | 2.6 | 21.3 | 0.8 | 40.0 | 190.0 |
| 17-1-P124 | 38 | 153.2 | 2.5 | 143.5 | 1.2 | 310.0 | 40.0 |
| 17-1-P124 | 33 | 187.6 | 5.1 | 145.2 | 1.1 | 742.0 | 57.0 |
| 17-1-P124 | 19 | 177.0 | 15.0 | 147.9 | 3.7 | 490.0 | 180.0 |
| 17-1-P124 | 38 | 150.5 | 2.2 | 147.0 | 1.0 | 217.0 | 34.0 |
| 17-1-P124 | 38 | 188.1 | 7.9 | 142.6 | 2.2 | 756.0 | 97.0 |
| 17-1-P124 | 16 | 158.8 | 3.0 | 152.3 | 1.5 | 266.0 | 43.0 |

| | | | | | | | |
|---|---|---|---|---|---|---|---|
| 17-1-P124 | 16 | 171.2 | 6.4 | 149.6 | 1.5 | 523.0 | 98.0 |
| 17-1-P124 | 15 | 754.0 | 19.0 | 198.1 | 3.3 | 3221.0 | 43.0 |
| 17-1-P124 | 38 | 137.0 | 10.0 | 140.6 | 3.3 | 80.0 | 140.0 |
| 17-1-P124 | 38 | 146.0 | 4.6 | 144.3 | 1.7 | 190.0 | 69.0 |
| 17-1-P124 | 37 | 153.2 | 2.6 | 143.8 | 1.2 | 308.0 | 43.0 |
| 17-1-P124 | 10 | 245.0 | 22.0 | 146.0 | 4.0 | 1210.0 | 220.0 |
| 17-1-P124 | 38 | 141.7 | 4.5 | 142.0 | 1.6 | 151.0 | 68.0 |
| 17-1-P124 | 16 | 193.7 | 5.8 | 146.7 | 1.6 | 797.0 | 75.0 |
| 17-1-P124 | 38 | 152.2 | 3.0 | 145.8 | 1.2 | 254.0 | 46.0 |
| 17-1-P124 | 38 | 144.6 | 1.4 | 141.2 | 0.8 | 210.0 | 22.0 |
| **Sample** | **Duration (sec)** | **FinalAge 207_235** | **FinalAge 207_235_Int2SE** | **FinalAge 206_238** | **FinalAge 206_238_Int2SE** | **FinalAge 207_206** | **FinalAge 207_206_Int2SE** |
| 18-1-PJ73 | 17.016 | 290 | 14 | 137.6 | 3.2 | 1760 | 110 |
| 18-1-PJ73 | 27.674 | 131.3 | 7.7 | 134.1 | 2.9 | 120 | 120 |
| 18-1-PJ73 | 27.674 | 138.2 | 6.3 | 139.8 | 2.4 | 162 | 91 |
| 18-1-PJ73 | 24.122 | 138.3 | 5.7 | 137.5 | 2.4 | 164 | 91 |
| 18-1-PJ73 | 25.011 | 153.2 | 6.4 | 138.9 | 1.8 | 387 | 92 |
| 18-1-PJ73 | 23.529 | 139.4 | 4.6 | 136.5 | 1.6 | 184 | 70 |
| 18-1-PJ73 | 25.898 | 148.6 | 4.9 | 132.5 | 1.5 | 379 | 74 |
| 18-1-PJ73 | 27.675 | 143.8 | 6.8 | 136.3 | 2.3 | 244 | 98 |
| 18-1-PJ73 | 25.602 | 191.3 | 8.4 | 134.1 | 2.5 | 890 | 100 |
| 18-1-PJ73 | 26.194 | 147.7 | 7.8 | 135.2 | 2.6 | 310 | 110 |
| 18-1-PJ73 | 27.675 | 148.6 | 5.5 | 138.8 | 1.8 | 285 | 75 |
| 18-1-PJ73 | 25.898 | 203 | 11 | 140.6 | 2.1 | 890 | 120 |
| 18-1-PJ73 | 27.674 | 139.6 | 6.2 | 132.7 | 2 | 269 | 98 |
| 18-1-PJ73 | 20.273 | 135.8 | 6.7 | 132.7 | 2.7 | 220 | 110 |
| 18-1-PJ73 | 22.05 | 153.8 | 7.7 | 130.9 | 2.2 | 470 | 100 |
| 18-1-PJ73 | 20.866 | 133.5 | 5.7 | 134 | 2 | 133 | 88 |
| 18-1-PJ73 | 22.049 | 212.2 | 9.8 | 143.7 | 2.7 | 1000 | 110 |
| 18-1-PJ73 | 23.233 | 197.1 | 6 | 139.6 | 1.8 | 922 | 70 |
| 18-1-PJ73 | 23.233 | 159 | 11 | 143.3 | 3.3 | 320 | 140 |
| 18-1-PJ73 | 23.825 | 475 | 16 | 167.8 | 3.4 | 2488 | 69 |
| 18-1-PJ73 | 24.417 | 313 | 24 | 160.2 | 3.8 | 1520 | 160 |
| 18-1-PJ73 | 27.675 | 335 | 14 | 151.4 | 3.2 | 1905 | 89 |
| 18-1-PJ73 | 27.674 | 346 | 16 | 149.6 | 2.7 | 2017 | 92 |
| 18-1-PJ73 | 24.418 | 131.4 | 6.5 | 139.1 | 2.4 | 55 | 97 |
| 18-1-PJ73 | 27.674 | 201 | 11 | 138.5 | 2.5 | 910 | 120 |
| 18-1-PJ73 | 24.715 | 138.3 | 7.5 | 129.4 | 2.5 | 300 | 120 |
| 18-1-PJ73 | 30.043 | 203 | 12 | 140.1 | 1.8 | 950 | 120 |
| 18-1-PJ73 | 17.904 | 141.1 | 5.7 | 131.6 | 2.2 | 278 | 90 |
| **Sample** | **Duration (sec)** | **FinalAge 207_235** | **FinalAge 207_235_Int2SE** | **FinalAge 206_238** | **FinalAge 206_238_Int2SE** | **FinalAge 207_206** | **FinalAge 207_206_Int2SE** |
| 18-1-PJ81 | 27.674 | 182.4 | 4.3 | 177.6 | 1.7 | 262 | 56 |
| 18-1-PJ81 | 27.674 | 168 | 4 | 166.7 | 2 | 209 | 58 |
| 18-1-PJ81 | 25.898 | 184 | 4.8 | 183.2 | 2.2 | 189 | 61 |

| | | | | | | | |
|---|---|---|---|---|---|---|---|
| 18-1-PJ81 | 21.954 | 187.1 | 7.3 | 186 | 2.4 | 176 | 83 |
| 18-1-PJ81 | 22.7 | 173.7 | 6.1 | 172.2 | 2.9 | 203 | 74 |
| 18-1-PJ81 | 27.675 | 191.9 | 5.9 | 182.6 | 2.1 | 289 | 70 |
| 18-1-PJ81 | 27.675 | 185.3 | 4.6 | 179.8 | 1.7 | 250 | 59 |
| 18-1-PJ81 | 27.675 | 173.1 | 6.4 | 183 | 2.4 | 81 | 77 |
| 18-1-PJ81 | 27.674 | 183.5 | 3.9 | 180.7 | 1.7 | 231 | 50 |
| 18-1-PJ81 | 27.675 | 174.2 | 5.4 | 178 | 2.4 | 141 | 69 |
| 18-1-PJ81 | 27.674 | 194.5 | 5.8 | 185 | 2 | 303 | 70 |
| 18-1-PJ81 | 25.307 | 181.3 | 4.3 | 176.5 | 2.2 | 239 | 57 |
| 18-1-PJ81 | 27.674 | 175.6 | 5.5 | 175.3 | 2.6 | 181 | 72 |
| 18-1-PJ81 | 25.011 | 177.4 | 4.6 | 165.6 | 2.2 | 306 | 62 |
| 18-1-PJ81 | 20.569 | 177.5 | 3.8 | 174.9 | 1.6 | 187 | 51 |
| 18-1-PJ81 | 27.674 | 184.2 | 6 | 183.6 | 2.2 | 177 | 75 |
| 18-1-PJ81 | 27.674 | 182.2 | 5.9 | 183 | 2.2 | 167 | 74 |
| 18-1-PJ81 | 27.675 | 185.8 | 4.1 | 184.6 | 1.8 | 198 | 51 |
| 18-1-PJ81 | 24.122 | 171.4 | 5.2 | 171.1 | 2.1 | 171 | 68 |
| 18-1-PJ81 | 21.753 | 178.6 | 6.7 | 170.6 | 2.8 | 271 | 81 |
| 18-1-PJ81 | 19.386 | 184.1 | 4.5 | 173.8 | 2.1 | 318 | 61 |
| 18-1-PJ81 | 27.674 | 177.6 | 3.3 | 177.3 | 1.4 | 188 | 45 |
| 18-1-PJ81 | 27.675 | 172.3 | 3.8 | 175.2 | 1.6 | 139 | 51 |
| 18-1-PJ81 | 27.674 | 182.9 | 5.1 | 180.7 | 2.4 | 208 | 67 |
| 18-1-PJ81 | 26.49 | 182.8 | 3.9 | 179.9 | 1.6 | 222 | 51 |
| 18-1-PJ81 | 19.385 | 175.9 | 6.9 | 169.4 | 2.3 | 274 | 93 |
| 18-1-PJ81 | 27.675 | 167.3 | 4 | 167.6 | 1.8 | 165 | 56 |
| 18-1-PJ81 | 17.312 | 180.8 | 2.8 | 178.3 | 2.2 | 218 | 33 |
| 18-1-PJ81 | 27.674 | 187.3 | 4.3 | 189.1 | 2 | 163 | 54 |
| 18-1-PJ81 | 27.675 | 191.2 | 5.8 | 182.4 | 1.9 | 313 | 74 |
| 18-1-PJ81 | 23.233 | 203.2 | 6.5 | 186.7 | 2.5 | 374 | 81 |
| 18-1-PJ81 | 27.674 | 172.9 | 4 | 169.6 | 2.1 | 210 | 50 |
| 18-1-PJ81 | 27.674 | 194.5 | 5.8 | 180.3 | 1.9 | 338 | 68 |
| 18-1-PJ81 | 27.674 | 181 | 2.9 | 177.8 | 1.7 | 222 | 41 |
| 18-1-PJ81 | 27.674 | 187.3 | 6.5 | 184.3 | 2.6 | 221 | 80 |
| 18-1-PJ81 | 27.675 | 188.5 | 5.6 | 176.3 | 1.6 | 326 | 67 |
| 18-1-PJ81 | 27.674 | 180.5 | 5.4 | 180.4 | 1.9 | 180 | 67 |
| 18-1-PJ81 | 13.169 | 178.5 | 8 | 177.5 | 2.7 | 190 | 100 |
| 18-1-PJ81 | 21.458 | 170.8 | 5.4 | 173.5 | 2.5 | 164 | 78 |
| 18-1-PJ81 | 27.675 | 176.2 | 4 | 174.1 | 1.6 | 206 | 53 |
| 18-1-PJ81 | 27.674 | 170.3 | 4.2 | 171.8 | 2 | 165 | 54 |

**Appendix 3:** Table of notes from all thin sections within the area. The grey highlighted sample bozes are strained oriented samples, the medium blue highlighted sample boxes are oversized oriented thin sections, the light blue are oriented samples that were doublely polished for electron backscatter diffraction analyses (EBSD), and the white samples are unoriented and/or unstrained samples.

| Thin Section Name | Rock Unit | Kinematics | Microstructure shear sense | Modal Abundance Mineral: | Modal Abundance | Mineral Condition | Notes/ Photos | IUGS Q:P:K | Quartz recrystallized grain size (μm) |
|---|---|---|---|---|---|---|---|---|---|
| 161-24 | Early Cretaceous tonalite | sinistral | Variable foliation makes it difficult to tell shear sense but looks top to the N | **Mineral:** | **%:** | | Late epidote veins, fractures, small cataclasite seams along fractures. Variable foliation and late fractures make it difficult to determine shear sense. There is a large foliation parallel cataclastic zone in the bottom of the thin section. It is bounded on both sides by cataclastic fractures. | | 10.6 |
| | | | | Quartz | 30% | dynamically recrystallized | | | |
| | | | | Unknown Feldspar | 25% | so sericitized and altered that I can't identify it. It's probably 5:1 plag:k-spar | | | |
| | | | | Plagioclase | 35% | sericitized/saussuritized, fractured | | | |
| | | | | K-spar | 5% | fractured and altered but can still see some tartan twinning | | | |
| | | | | Epidote | 5% | Late veins | | | |
| p161-28 | Barite sample from north of the field area | None | Barite | **Mineral:** | **%:** | | Late barite vein, with trace amounts of CPX and late veins filled with iron oxide | | |
| | | | | Barite | ~99% | Recrystallized barite | | | |
| | | | | Amphibole | ~1% | | | | |
| 161-30a | Hydrothermally-altered zone | sinistral | Asymmetrical Porphyroblasts and S fabric look top to the N | **Mineral:** | **%:** | | In some granodiorite clasts the quartz is dynamically recrystallized (~25 microns) and other areas, between clasts, quartz recrystallization is much smaller (~6 microns). In most areas of through going matrix, strain is localized into | | |
| | | | | Quartz | 30% | usually fine grained sometimes recrystallized where exclusively quartz in matrix and clasts | | | |
| | | | | Unknown Feldspar | 15% | | | | |

| | | | | | | | | | |
|---|---|---|---|---|---|---|---|---|---|
| | | | | Plagioclase | 25% | Some sericitized, mostly unaltered, preserved albitic twinning, fractured, some antithetic domino plag grains suggest top to the N | areas of comminuted feldspars, oxides, fine quartz, and actinolite. Sections of the thin sections are almost purely actinolite. Possibly transposed basaltic dike that brecciated granodiorite. (photos for vorticity) | | |
| | | | | K-spar | 5% | | | | |
| | | | | Actinolite | 20% | most likely transposed basaltic dike | | | |
| | | | | Oxides | 5% | likely from the dike | | | |
| P161-30c | Hydrothermally-altered zone | sinistral | Quartz shear bands top to the N | **Mineral:** | **%:** | | Modal mineralogies are approximate. This sample is extremely fine grained. With quartz plag comminuted zones (Photos for vorticity) | | |
| | | | | Quartz | 30% | | | | |
| | | | | Unknown Feldspar | 45% | | | | |
| | | | | Plagioclase | 8% | | | | |
| | | | | K-spar | 0% | | | | |
| | | | | Actinolite | 15% | | | | |
| | | | | Oxides | 2% | | | | |
| 17-1-P2 | Deformed Early Jurassic granodiorite | none | Sausauritized grunge | | | | extremely comminuted mixture of quartz and feldspar, late calcite precipitation | | |
| 17-1-P5 | Gouge zone | none | grungy mess, brecciated, no SS | | | calcite veins and precipitated | taken from east of the fault right at the margin of the gouge zone. A sample of brecciated fractured mylonite with cataclastic zone. Photo of fracture mylonite. | | |
| 17-1-P5B | Early Jurassic granodiorite clast within the gouge zone | none | grungy, no SS | | | | brecciated granitic clasts most likely originating from the west side Jurassic granitoid because there is no evidence of ductile deformation | | |
| 17-1- | Early | none | SW | **Mineral:** | | | foliation parallel | | 6 |

| | | | | | | | | | |
|---|---|---|---|---|---|---|---|---|---|
| P6c | Cretaceous tonalite | | | Quartz | 45% | through going quartz layers localize strain, vorticity and grain shape fabric measured | cataclasite, with through going quartz veins that localized the strain. Late cataclastic zones parallel foliation, some cross cut. | | |
| | | | | Unknown Feldspar | 35% | probably almost all plagioclase | | | |
| | | | | Plagioclase | 10% | sericitized/sa ussuritized, fractured | | | |
| | | | | K-spar | 0% | ? No noticeable k-spar features | | | |
| | | | | Chlorite | 7% | Fine grained within the cataclastic zones | | | |
| | | | | Oxides | 3% | | | | |
| 17-1-P18 | <50% mylonite within the Late Jurassic-Early Cretaceous granodiorite | none | top away from notch but shear sense iffy because fol is variable | **Mineral:** | | | The rest of this sample is altered iron stained clays? It looks like this sample was a granitoid but the plagioclase has been altered to clays of some sort and everything has been iron stained | | |
| | | | | Quartz | 20% | | | | |
| | | | | Oxides | 4% | | | | |
| 17-1-P32 | <50% mylonite within the Late Jurassic-Early Cretaceous granodiorite | sinistral | shear bands at very low angle to foliation but appear top to the north | **Mineral:** | | | through going fine grained quartz and plagioclase. Probably about 45 to 65 quartz, feldspar assumed from the percent of the thin section that is sericitized. Regions of more quartz have a larger grain size than expected, because the fine quartz feldspar mixture is the through going deformation phase | | |
| | | | | Quartz | 35% | extremely fine grained except in certain areas | | | |
| | | | | Unknown Feldspar | 55% | extremely fined grained and sericitized | | | |
| | | | | Epidote | 8% | | | | |
| | | | | Oxides | 2% | | | | |
| 17-1-P43a | Hydrothermally-altered zone | none | fol variable no ss, late | **Mineral:** | | | Sample from the hydrothermally | | |
| | | | | Amphibole | 55% | | | | |

| | | | | | | | | | |
|---|---|---|---|---|---|---|---|---|---|
| | | | unstrained quartz veins | Quartz<br>Feldspar<br>Oxides | 10%<br>30%<br>5% | | altered zone. Extensional quartz veins most likely associated with the hydrothermal alteration at the brittle ductile transition. Fluid inclusions in quartz veins. | | |
| 17-1-P43c | Hydrothermally-altered zone | sinistral | fol var. but appears top to the North | **Mineral:**<br>Quartz<br>Feldspar<br><br><br><br>Amphibole<br>Oxides | <br>20%<br>35%<br><br><br><br>35%<br>5% | <br><br>sericitized/saussuritized, fractured | Extremely fine grained zones composed of amphibole, feldspar, oxides, and quartz. Quartz and feldspar zones with very little amphibole are likely granitoid clasts. In the top of the thin section, there is a clast with quartz regions that have a larger recrystallized grain size than would be expected at the brittle ductile transition. | | 23.7 |
| 17-1-P45 | Hydrothermally-altered zone | sinistral | not very recrystallized, but in areas appears top to the north | **Mineral:**<br>Quartz<br>Unknown Feldspar<br>Amphibole | <br>25%<br>55%<br>20% | <br><br>Sericitized | Fine grained quartz and feldspar with some areas of pure quartz which would be good for calculating vorticity. Stringers of amphibole possibly transposed mafic dikes | | |
| 17-1-P50 | Early Cretaceous tonalite | sinistral | fol variable but looks top to the north | **Mineral:**<br>Quartz<br>Unknown Feldspar<br>Chlorite | <br>35%<br>55%<br>10% | | Through going quartz localized strain. | | 17.8 |
| 17-1-P56 | Hydrothermally-altered zone | sinistral | shear bands at low angle to foliation but is top to the north | **Mineral:**<br>Quartz<br>Unknown Feldspar<br>Chlorite | <br>45%<br>45%<br>10% | | Through going quartz regions in this sample | | |
| 17-1-P84 | Hydrothermally-altered zone | sinistral | top to the north but bands at low angle to fol, some are opposite shear sense | **Mineral:**<br>Quartz<br>Unknown Feldspar<br>Chlorite<br>Oxides<br>Actinolite | <br>25%<br>40%<br>10%<br>5%<br>20% | | relatively more mafic than other samples, comes from within the bleached zone which has a lot of transposed dikes | | 19.8 |
| 17-1-P133 | <50% mylonite within the Late | dextral | top to the south | **Mineral:**<br>Quartz | <br>30% | | | | |

| | | | | | | | | | |
|---|---|---|---|---|---|---|---|---|---|
| | Jurassic-Early Cretaceous granodiorite | | | Unknown Feldspar<br>Chlorite<br>Oxides<br>Actinolite | 60%<br>4%<br>1%<br>5% | | | | |
| 18-1-PJ68A | Early Cretaceous tonalite | Sinistral | s fabric of dynamically recrystallized quartz shows top to the North slip sense (sinistral) | **Mineral:**<br>Quartz<br>Unknown Feldspar<br><br><br>Plagioclase<br>Chlorite | <br>25%<br>65%<br><br><br>5%<br>5% | <br><br>sericitized/saussuritized, fractured | Some isolated quartz rich areas but most of the strain is localized in the fine grained quartz, feldspar zones. Late fractures run throughout the section | | |
| 18-1-PJ72 | Early Cretaceous tonalite | Sinistral | top towards N but hard to tell as evidenced by domino feldspar and slight oblique grain shape fabric | **Mineral:**<br>Quartz<br>Unknown Feldspar<br>Titanite<br>Oxides | <br>20%<br>76%<br>3%<br>1% | | Some larger porphyroclasts of plagioclase that are fractured | | |
| 18-1-PJ77 | Early Cretaceous tonalite | Sinistral | top away from S, indicated by oblique grain shape fabric | | | | | | 12.6 |
| 18-1-PJ80 | Early Cretaceous tonalite | none | very slightly asymmetric clasts suggest top away from N (dextral?) | | | | | | |
| 18-1-PJ80B | Early Cretaceous tonalite | none | too brecciated to tell original shear sense | | | | | | |
| 18-1-PS242 | <50% mylonite within the Late Jurassic-Early Cretaceous granodiorite | sinistral | Top to the N, beautiful asymmetric porphyroclasts | | | | | | |
| 17-1-P117b | Hydrothermally-altered zone | unclear | no SS, but C' suggest top away from notch, unclear if sinistral or dextral because of sample orientation | | | | Photos of mafic foliation | | |
| 17-1-P43b | Hydrothermally-altered zone | sinistral | top to the north but somewhat variable (some look top to the S) | | | | | | |
| 17-1-P117 | Hydrothermally-altered zone | None | not very dynamically recrystallized, very low angle to fol., No SS | | | | | | |

| | | | | | | | |
|---|---|---|---|---|---|---|---|
| 18-1-PJ58B | Hydrothermally-altered zone | Sinistral | Not very dynamically recrystallized, mostly asymmetric porphyroclasts, feldspar quartz through-going quartz | | oversized thin section of a less altered/more altered contact in the same thin section. Across the boundary in the more altered half, the feldspars are more altered, there are more quartz rich regions and there is no chlorite. | | |
| 161-22 | | sinistral | | | | | |
| P161-23a | Early Cretaceous tonalite | sinistral | Oblique grain shape fabric top to the SW, sinistral | | | | |
| 161-29 | | None | No SS | | | | |
| 161-30a | Hydrothermally-altered zone | sinistral | | | | | |
| 161-30b | Hydrothermally-altered zone | None | No SS | | | | |
| 17-1-P6 | Early Cretaceous tonalite | sinistral | Fine grained but C' suggest top N | | | | 7.6 |
| 17-1-P9 | Hydrothermally-altered zone | sinistral | low angle shear bands suggest top to the N | | | | 33.3 |
| 17-1-P36 | >50% mylonite zone within the Late Jurassic-Early Cretaceous granodiorite | sinistral | Asymmetric porphyroblasts suggest top to the N, shear bands are at a very low angle to the foliation | | | | |
| 17-1-P45b | Hydrothermally-altered zone | None | Some top to the N some top to the S | | | | |
| 17-1-P79 | Early Cretaceous tonalite | sinistral | Top to the N | | | | 93.4 |
| 17-1-P93 | Hydrothermally-altered zone | sinistral | Rare quartz seems look top to the N, but asymmetric porphyroblasts look top to the S | | | | |
| 17-1-P95 | Hydrothermally-altered zone | sinistral | Top to the N | | | | 25.4 |
| 17-1-P124 | Hydrothermally-altered zone | None | No SS bad for EBSD (mostly extremely fine grained | | | | |
| 17-1-P50 | Early Cretaceous tonalite | sinistral | fol variable but looks top to the north | **Mineral:**<br>Quartz 35%<br>Unknown 55%<br>Feldspar<br>Chlorite 10% | Through going quartz localized strain. | | |

| | | | | | | | |
|---|---|---|---|---|---|---|---|
| 17-1-P133 | <50% mylonite within the Late Jurassic-Early Cretaceous granodiorite | dextral | top to the south | **Mineral:** | | | |
| P161-23c | | | | **Mineral:**<br>Quartz 20%<br>Unknown Feldspar 60%<br>Chlorite 5%<br>Actinolite 15% | | Actinolite rich zone was believed to be previously pseudotachylyte, fine-grained feldspar and quartz, no dynamic recrystallization of quartz | |
| P161-25 | | | | | | brittle fractured and comminuted, many calcite veins, cannot determine mineralogy through microscope | |
| P161-31 | | | | **Mineral:**<br>Quartz 18%<br>Unknown Feldspar 15<br>Plagioclase 45% extremely sericitized, usually zoned or has perthitic twinning<br>K-spar 5%<br>Biotite 2% almost all chloritized<br>Chlorite 2% most likely secondary after biotite<br>Amphibole 2%<br>Oxides 2% | | Dated Pluton: Coarser grained than the other plutons. Some interstitial quartz growth. Large plagioclase crystals are subhedral. | 18.8 : 75 : 6.3 |
| 17-1-P6b | Early Cretaceous tonalite | | | | | Sample from up against the gouge zone, extremely brittlely deformed ultramylonite, mineralogy is difficult to determine because of such a small grain size. There are some late possibly epidote veins | |
| 17-1-P17 | <50% mylonite within the Late Jurassic-Early Cretaceous granodiorite | | | Actinolite 50%<br>Oxides (probably sulfides) 50%<br>Plagioclase <1% | | | |

| | | | | | | | |
|---|---|---|---|---|---|---|---|
| 17-1-P23 | Unstrained Late Jurassic-Early Cretaceous granodiorite | | | | Altered granodiorite protolith. No foliation present. Feldspar is completely altered. Chlorite replacing biotite | | |
| 17-1-P24a | Unstrained Late Jurassic-Early Cretaceous granodiorite | | | | Altered granodiorite protolith however it is less altered than 17-1-P23. This sample also has a consistently larger grain size | | |
| 17-1-P26 | Unstrained Late Jurassic-Early Cretaceous granodiorite | | none | **Mineral:**<br>Quartz 25%<br>Unknown Feldspar 15% probably majorly plagioclase (5:1?)<br>Plagioclase 25% sericitized, zoned plagioclase<br>K-spar 10%<br>Chlorite 5% likely chloritized biotite<br>Biotite 6% Chloritized rims<br>Amphibole 3% commonly twinned<br>Oxides 1% seems to be an interstitial phase | Dated Pluton Granodiorite: Porphyritic to seriate texture. Most of the biotite has either been completely altered to biotite or the remaining biotite has a chloritic rim. Not a good candidate for Ar-Ar. interstitial plag and quartz. A lot of the plagioclase have growth zonation with cores preferentially altering to white micas. Some feldspars have anorthoclase tartan twinning (~5% out of whole section). Carlsbad twins used to distinguish k-spar. | 33.33 : 49.33 : 17.33 | |
| 17-1-P28 | Unstrained Late Jurassic-Early Cretaceous granodiorite | | | Quartz 30%<br>Unknown Feldspar 55% probably majorly plagioclase (5:1?)<br>Chlorite 8% chloritized biotite<br>Biotite 2% Chloritized<br>Oxides 5% seems to be an interstitial phase | Feldspar has been sericitized | | |
| 17-1-P62 | Undifferentiated Jurassic metasedimentary unit | | | Quartz 30%<br>Unknown Feldspar 55% probably majorly plagioclase (5:1?) | many spherules, porphyritic, phenocrysts of plagioclase, diner grain quartz as interstitial phase | | |

| | | | | | | | | | |
|---|---|---|---|---|---|---|---|---|---|
| | | | | Chlorite<br><br>Oxides | 8%<br><br>3% | chloritized biotite | | | |
| 17-1-P63 | Undifferentiated Jurassic metasedimentary unit | | | | | | mostly micritic with some lenses of silty quartz, calcite veins present | | |
| 17-1-P70 | Early Jurassic granodiorite | | | | | | Plagioclase laths in the matrix with a groundmass of what looks to be fine-grained epidote and chlorite, the larger phenocrysts are chloritized pyroxene | | |
| 17-1-P77 | Early Jurassic granodiorite | | | | | | carbonate mud with more silt rich layers | | |
| 17-1-P89 | Unstrained Late Jurassic-Early Cretaceous granodiorite | | | Quartz<br>Unknown Feldspar<br><br><br>Chlorite<br><br>Oxides | 37%<br>58%<br><br><br>4%<br><br>1% | <br>probably majorly plagioclase (5:2)<br>chloritized biotite | Slightly more k-spar rich protolith from the southeast portion of the map. Medium-grained. Relatively all the same grain size (not porphyritic or seriate) | | |
| 17-1-P100 | Early Cretaceous tonalite | | | | | | strained rock with extremely fine-grained recrystallized quartz which wraps around altered feldspar porphyroclasts. Fractured foliation is no longer continuous, some cataclastic zones present, chlorite veins seem to be associated with cataclasis, late calcite veins. | | |
| 17-1-P102 | Early Jurassic granodiorite | | | | | | extremely altered sample, seems to have a faint intrusive texture. I can make out some primary plagioclase twins but most features are obscured by alteration. I believe this is an extremely altered brittlely deformed piece of the west-side granodiorite. | | |

| | | | | | | | |
|---|---|---|---|---|---|---|---|
| 17-1-P104 | Gouge zone | | | | in hand sample this rock appears purple, in thin section the sample is almost all massive oxides. Abundant late calcite veins, some very clusters of fine-grained brittlely deformed feldspar and quartz | | |
| 17-1-P105 | Early Jurassic granodiorite | | | Plagioclase 70%<br>Epidote 9%<br>Chlorite 20%<br>Oxides 1% possibly magnetite | matrix of this andesitic dike is composed of plagioclase laths and a groundmass of fine-grained chlorite and epidote. The plagioclase laths are larger than the sample 17-1-P70. There are phenocrysts of plagioclase which have been altered partially to sericite | | |
| 17-1-P137 | >50% mylonite zone within the Late Jurassic-Early Cretaceous granodiorite | | | | granitoid with interstitial plag quartz and phenocrysts of plagioclase | | |
| 17-1-P142 | Undifferentiated Jurassic metasedimentary unit | | | | silty mudstone | | |
| 17-1-P146 | Early Jurassic granodiorite | | | | cataclastically deformed sample | | |
| 17-1-P120 | Undeformed basaltic dike within the hydrothermally-altered zone | | | | basaltic dike with altered phenocrysts, originally plagioclase pyroxene and hornblende, fine grained ground mass | | |
| 18-1-PJ48 | Early Jurassic granodiorite | | | **Mineral:**<br>Quartz 25%<br>Plagioclase 49%<br>K-spar 14%<br>Chlorite 10%<br>Biotite <1%<br>Oxides 1% | | | |

| | | | | | | | |
|---|---|---|---|---|---|---|---|
| 18-1-PJ50 | Early Jurassic granodiorite | | | | basaltic dike with groundmass of plagioclase laths and fine grained chlorite and epidote, phenocrysts are partially altered pyroxene and plag | | |
| 18-1-PJ61 | Early Jurassic granodiorite | | | | extremely altered andesitic dike | | |
| 18-1-PJ62 | Early Jurassic granodiorite | | | **Mineral:**<br>Quartz 27%<br>Plagioclase 40%<br>K-spar 19%<br>Chlorite 10%<br>Biotite 3%<br>Oxides 1% | Myrmekite | | |
| 18-1-PJ66 | Early Jurassic granodiorite | | | **Mineral:**<br>Quartz 25%<br>Plagioclase 45%<br>K-spar 15%<br>Chlorite 14%<br>Oxides 1% | | | |
| 18-1-PJ73 | Early Cretaceous tonalite | | Cataclastic zones, however since this sample is unoriented no shear sense is interpreted | **Mineral:**<br>Quartz 20%<br>Unknown Feldspar 15% plag to kspar probably almost all plagioclase<br>Plagioclase 30% many plagioclase crystals are zoned and their cores are preferentially altering to sericite<br>K-spar 4%<br>Chlorite 8% Probably some primary chlorite, but most of it looks like it is associated with cataclastic veins. Also one crystal of chlorite looks like it is replacing biotite<br>Amphibole 20%<br>Oxides 2% | **Dated Pluton:** Porphyritic to seriate growth texture. | 28.6 : 65.7 : 5.7 | |

| | | | | | | | | | |
|---|---|---|---|---|---|---|---|---|---|
| 18-1-PJ81 | Early Jurassic granodiorite | | | **Mineral:** | | | **Dated Pluton:** coarse grained plagioclase with interstitial quartz. The feldspars are extremely altered almost to the point that you can no longer see twins or zoned plagioclase | 18.1 : 72.3 : 9.6 | |
| | | | | Quartz | 20% | | | | |
| | | | | Unknown Feldspar | 40% | extremely saussuritized, most likely all plag | | | |
| | | | | Plagioclase | 20% | extremely altered | | | |
| | | | | K-spar | 3% | extremely altered | | | |
| | | | | Calcite | 2% | sparry calcite, possibly late discrete veins or maybe source from altering calcium feldspar | | | |
| | | | | Chlorite | 10% | due to the presence of oxides associated with the chlorite, it is likely that this chlorite is secondary after biotite | | | |
| | | | | Oxides | 5% | All found within chlorite | | | |
| 18-1-PS186 | Early Jurassic granodiorite | | | | | | extremely altered andesitic dike | | |
| 18-1-PS204 | Early Jurassic granodiorite | | | | | | west-side granodiorite biotite is partially altered to chlorite | | |
| 18-1-PS207 | Early Jurassic granodiorite | | | | | | mafic dike with plagioclase and olivine phenocrysts (altered to serpentinite), and pyroxene, matrix is made up of plagioclase laths and fine-grained groundmass | | |
| 18-1-PS240 | Early Cretaceous tonalite | | | | | | cataclastically deformed sample of the Early cretaceous tonalite | | |
| | | | | Quartz | 15% | | | | |
| | | | | Plagioclase | 50% | slightly altered | | | |
| | | | | K-spar | 3% | slightly altered | | | |
| | | | | Amphibole | 19% | commonly twinned | | | |

| | | | | | | | | |
|---|---|---|---|---|---|---|---|---|
| | | | | Chlorite | 8% | late veinlets | | |
| | | | | Oxides | 5% | both primary and secondary (as veins) | | |
| 18-1-PS246 | <50% mylonite within the Late Jurassic-Early Cretaceous granodiorite | | | | | a lot of myrmekite, euhedral epidote replacing possibly plagioclase feldspar, sample of the Late Jurassic granodiorite | | |

A

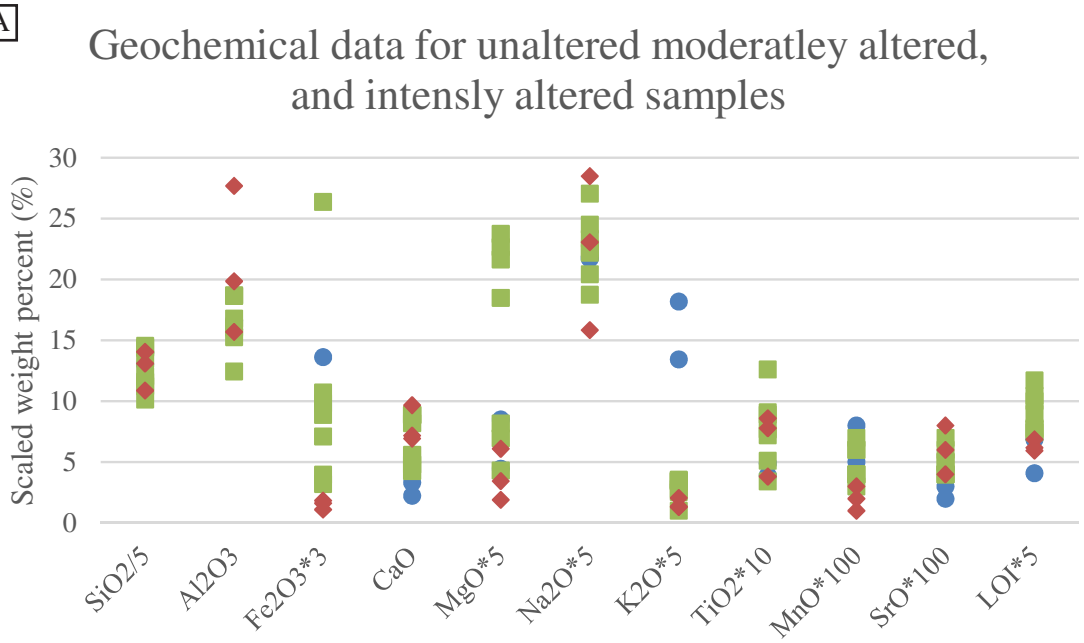


B

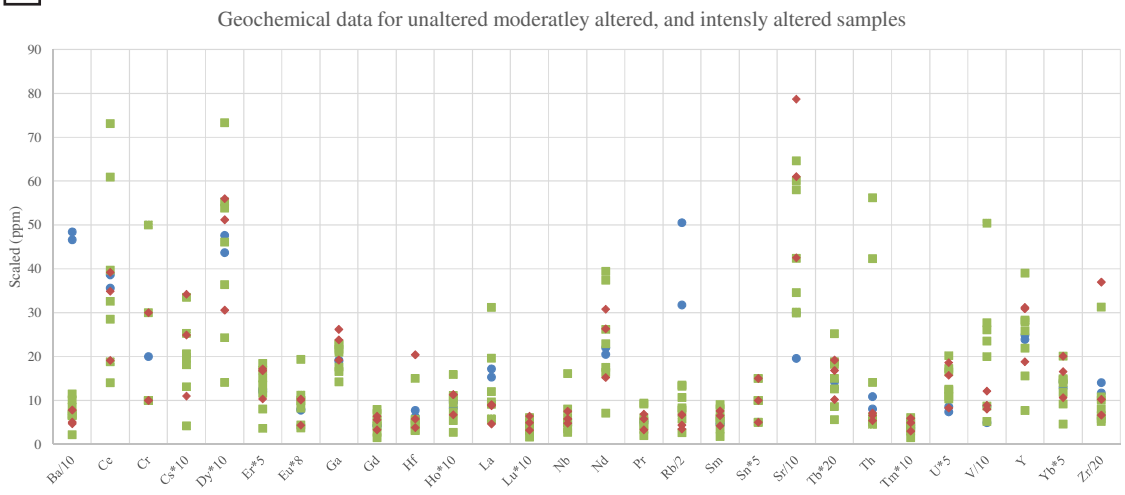


**Appendix 4: A)** Plot of the scaled weight percents for major elements and **B)** plot of the scaled ppm of trace elements separated into unaltered (blue dots), moderately altered (green squares), and intensely altered (red diamonds). Alteration amount was qualitatively assigned using field and microstructural observations. There is no noticeable pattern in the trace elements, but in the major elements we see an increase in CaO with alteration and a decrease in $K_2O$ with an increase in alteration.

**Appendix 5:** Table of root mean square grain size, arithmetic mean grain size, and standard deviation for 5 samples from the hydrothermally-altered zone and 5 samples from the Early Cretaceous tonalite.

| Sample name | Unit | Root mean square grain size (µm) | Arithmetic mean grain size (µm) | Standard deviation (µm) | Number of grains measured |
|---|---|---|---|---|---|
| 16-1-P23a | Hydrothermally altered zone | 20.4 | 19.8 | 4.9 | 204 |
| 16-1-P24 | Tonalite | 10.6 | 10.3 | 2.5 | 203 |
| 17-1-P6 | Tonalite | 7.6 | 7.5 | 1.2 | 202 |
| 17-1-P6c | Tonalite | 6.0 | 5.9 | 1.2 | 205 |
| 17-1-P9 | Hydrothermally altered zone | 33.3 | 32.2 | 8.5 | 207 |
| 17-1-P43c | Hydrothermally altered zone | 23.8 | 22.7 | 7.1 | 202 |
| 17-1-P50 | Tonalite | 17.8 | 16.8 | 5.8 | 203 |
| 17-1-P84 | Hydrothermally altered zone | 19.8 | 17.3 | 9.6 | 204 |
| 17-1-P95 | Hydrothermally altered zone | 25.4 | 24.6 | 6.2 | 204 |
| 18-1-P77 | Tonalite | 12.6 | 12.2 | 3.0 | 206 |